COMPUTER SIMULATION STUDIES OF MnO_2 AND $LiMn_2O_4$ NANOTUBES

by

DAVID MAGOLEGO TSHWANE

RESEARCH DISSERTATION

Submitted in fulfilment of the requirements for the degree of

MASTER OF SCIENCE

in

Physics

in the

FACULTY OF SCIENCE AND AGRICULTURE

(School of Physical and Mineral Sciences)

at the

UNIVERSITY OF LIMPOPO

Supervisor: **Prof. R.R. Maphanga**

Co-Supervisor: **Prof. P.E. Ngoepe**

2016

Abstract

Nanostructured materials are attractive candidates for efficient electrochemical energy storage devices because of their unique physicochemical properties. Introducing nanotube systems as electrode materials represents one of the most attractive strategies that could dramatically enhance the battery performance. Nanostructured manganese based oxides are considered as ideal electrode materials for energy storage devices such as high energy and high power lithium-ion batteries. In this study, computer simulation strategies were used to generate various structures of MnO_2 and spinel $LiMn_2O_4$ nanotubes; where Miller index, diameter and symmetry are considered as variables. The effect of these variables on nanotube generation was investigated. MnO_2 and spinel $LiMn_2O_4$ nanotubes were generated using MedeA® software. Lower Miller indices, namely; {001}, {100}, {110} and {111} with diameter ranging from 5Å-30Å were investigated for both systems. There are two ways that a nanotube structures could be wrapped along different directions, i.e., a_around_b or b_around_a. It was observed that wrapping direction has an effect on the geometrical structure of the nanotube. MnO_2 nanotube generated from {110} revealed that nanotube wrapped along b_around_a gave a close-packed structure compared to its counterpart nanotube wrapped a_around_b. Diameter represents an important structural parameter of nanotubes; however, precise control of nanotube diameter over a wide range of materials is yet to be demonstrated. In this study, it was found that as the diameter of the nanotube is changed, parameters such as cross-sectional area and bond length change as well. The average bond distance of the nanotubes is less than that of MnO_2 and $LiMn_2O_4$ bulk structure. Molecular dynamics simulation is further used to investigate the structure of MnO_2 and $LiMn_2O_4$ nanotubes and the effect of temperature on the generated systems. Molecular graphical images used for the atomic positions for the nanotubes were investigated. The nanotube structures are described using radial distribution functions and XRD patterns. The calculated XRD patterns are in good agreement with the experiments, thus validating the generated structural models for the nanotubes. The resulting models conform to pyrolusite polymorph of MnO_2 and $LiMn_2O_4$, featuring octahedrally coordinated manganese atoms. It was established that the variables have a direct control on nanotube morphology and the stability of generated nanotube model depends on surface morphology and termination.

Declaration

I declare that the dissertation hereby submitted to the University of Limpopo for the degree Master of Science has not been submitted as an exercise for any other university, that is entirely my own work both in design and execution and that all material contained herein has been duly acknowledged.

_____ DATE

Tshwane D.M. (Mr.) 08/09/2016

Acknowledgements

I would like to take this appropriate time to thank my supervisor: Professor R.R. Maphanga and co-supervisor: Professor P.E. Ngoepe for the initiation of the project, wonderful support, patience, encouragement and fruitful discussions that led to completion of this project.

The calculations in this dissertation were undertaken at the Materials Modelling Centre (MMC) of the University of Limpopo and the Centre for High Performance Computing (CHPC) of CSIR in Cape Town. I received a substantial support from MMC team, they made the centre a good environment for me to work at. I really cherish the comfortable working environment and the cooperation as well as the productive discussions. I also thank the sponsors for this project: National Research Foundation (NRF) for financial support and Centre for High Performance Computing for computing resources.

Thanks to my family for the patience they have shown me, coupled with encouragement and support. Not forgetting all friends and colleagues for giving me delightful support over the period of my study.

I would like to thank the Almighty God for all the strength and perseverance He has installed in me during all the years of my studies.

Dedication

This work is dedicated to

my late Mother

Magane Julia Tshwane

my wonderful Father

Mamaile Petrus Tshwane

and

Tshwane Family

KE A LEBOGA MADEBELE

Table of Contents

List of Tables

List of Figures

Chapter 1

Introduction

1.1 General Introduction

Energy crisis is indubitably one of the great challenges in the 21st century [1]. The high energy demand is resulting in a rapid consumption of sources, which can lead to major problems in the future. These ever-growing energy needs and depleting fossil-fuel resources demand the pursuit of sustainable energy alternatives, including both renewable energy sources and sustainable storage technologies. To mitigate CO_2 emissions, exploiting renewable energy sources and storage is urgent, which necessitates reliable and environmentally friendly energy storage systems. Hence, there is a need to develop new materials for energy storage devices, with improved properties. Furthermore, it is essential to incorporate material abundance, eco-efficient synthetic process and life-cycle analysis into the design of new electrochemical storage systems. Currently, a few existing technologies address these issues, but in each case, fundamental and technological hurdles remain to be overcome.

Lithium-ion battery system with high energy and power is regarded as one of the near-term solution for energy storage because of its relatively simple reaction mechanism. Current lithium-ion battery technology is well-developed for the portable electronic devices (such as mobile phone, laptops, cameras, etc.) and has been widely used in the past 20 years. However, to implement Li-ion battery technology in large-scale high power systems such as electronic vehicles (EV), hybrid electronic vehicle (HEV) and plug-in hybrid electric vehicles (PHEV) is a challenge. Thus, despite that lithium-ion batteries can provide high energy, their power-density remains too low for high-power application. Furthermore, for high-power applications, performance requirements (energy/power density, cycling life and safety issues) are raised. Therefore, further lithium-ion battery materials and technology developments are essential. These advances and developments depend on exploring new classes of compounds and gaining a better understanding of the fundamental science of functional materials that underpin battery technology research.

Lithium-ion batteries are currently outperforming other battery systems as it is shown in figure 1. Among the various existing technologies, lithium-ion battery technologies are the systems of choice due to their high-energy density, flexible and light-weight design and longer-life span.

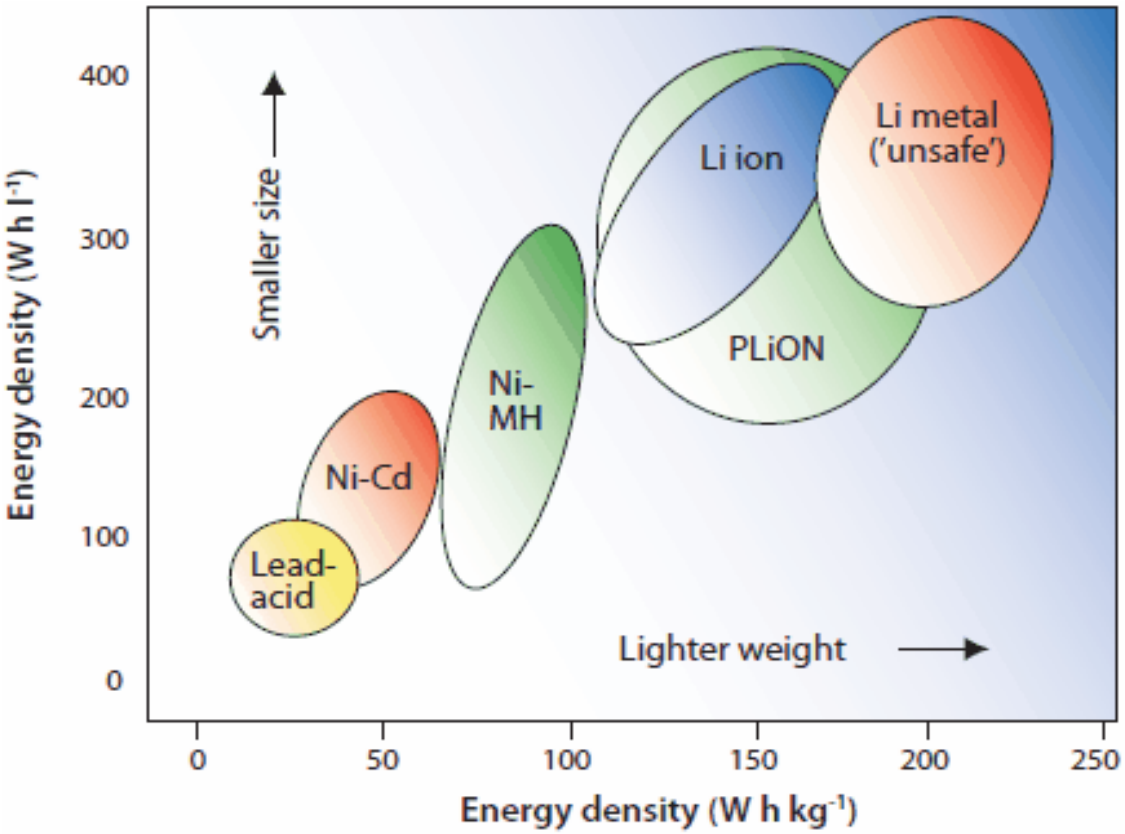

Figure 1: Schematic representation of comparison of different battery technologies in terms of volumetric and gravimetric energy density [2].

Recently, nanostructured materials have become increasingly important in the areas of physical, chemical and electrochemical energy storage, such as hydrogen storage and electrochemical performance for applications in Li-ion batteries [3, 4]. Materials at the nanoscale offer unique properties resulting in high performance electrodes and electrolytes in various energy storage applications. Consequently, considerable efforts have been made recently to fulfil the future requirements of electrochemical energy storage using the nanostructured materials. Various multi-functional hybrid

nanostructured materials are currently being investigated to improve energy and power densities of next generation storage devices, including lithium-ion batteries. The nanostructured electroactive materials provide a large surface area and therefore charge transfer resistances at electrode/electrolyte interface is effectively decreased. Nanostructured active battery materials tend to shorten the diffusion paths for lithium ions through the material, hence enhancing the charge/discharge reactions. Furthermore, nano-sized particles with a narrow size distribution (such as nanotubes, nanorods, nanowires, etc.) improve homogeneous current distribution in the electrode materials for high-power lithium-ion batteries. Amongst narrow size nanostructured materials, nanotubes are the most attractive candidates for the energy storage applications because of their large surface areas and surface-to-weight ratios [5]. Nanotubes do not only increase electron conductivity but also help improve Li^+ diffusion during the electrochemical reaction.

Nanostructured materials with various morphologies have been synthesised by a wide variety of synthetic approaches including hydrothermal solution-phase and templating methods, which greatly improve the electrochemical properties. However, synthesis of transition metal oxide nanostructures with controlled size, uniform morphology, good crystallinity and high dispersion remains a challenge. Therefore, continuous efforts on developing methods of synthesising nanostructured electrode materials are essential to solve these scientific challenges. Also, the fundamental basis for contrasting properties of nanostructures is not fully understood. In this study, computer simulation methods are employed to develop strategies for generating MnO_2 and $LiMn_2O_4$ nanotubes and investigate their physical properties.

1.2 Literature Review

1.2.1. Origin of Nanotubes

Nanotubes are subject of interest owing to their unique atomic structures and great potential in electronic, optical, mechanical and bioscience applications [6]. Tubular-structured materials have more virtues than other structures due to their potentially fast surface adsorption kinetics. Since the discovery of carbon nanotubes (CNTs) in 1991 by Iijima [7], CNTs have attracted much interest and are of great potential for the

next generation of nanoscale electronic devices, owing to their extraordinary electronic properties [8]. It has been confirmed theoretically and experimentally that carbon nanotubes possess remarkably high stiffness and strength [9]. They also have exceptionally high electrical and thermal conductivities [10]. Due to their extraordinary properties, carbon nanotubes hold a substantial promise for future technical applications in different areas such as, field emitters, molecular electronics and absorbent materials.

A carbon nanotube structure can be regarded as one gigantic molecule (fullerene) which is obtained by rolling-up graphite sheet into a cylinder, whose diameter is measured in nanometer and whose length can reach macroscopic dimensions. One unusual feature of nanotube structures is that they simultaneously involve widely varying scale, their length can be macroscopic, up to millimeters, while their width falls in the nanoscale. Nanotube may be visualised by wrapping bulk structure around a cylindrical surface. The direction of wrapping with respect to the crystal structure is known as the chiral vector. They occur in two main types, the single-wall nanotube (SWNT) as shown figure 2a and the multi-wall nanotube (MWNT) shown in figure 2b. A hollow cylinder made up of a single rolled-up sheet is a single walled nanotube (SWNT) and multi-walled nanotubes (MWNT) is composed of several concentric hollow cylinders. Double-walled nanotubes are the simplest MWNTs and they provide a good platform for studying the inter-tube interactions in MWNTs.

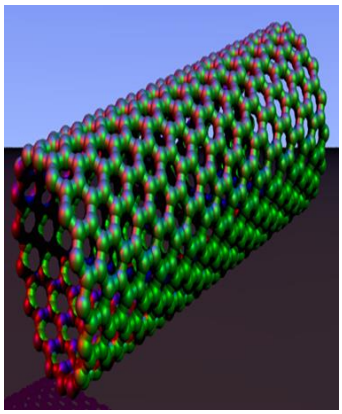

(a)

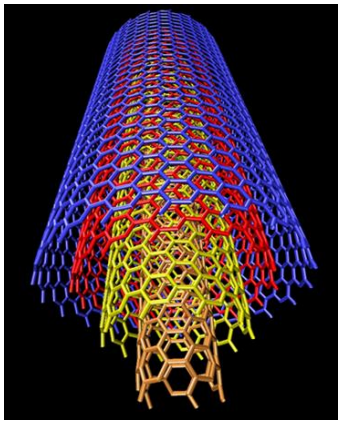

(b)

Figure 2: Schematic diagram of (a) single-walled carbon nanotube (SWCNTs) and (b) multi-walled carbon nanotube (MWCNTs).

In 1992, the first successful growth of inorganic nanotubes was reported by Tenne's group [11]. The report was issued only one year after the discovery of carbon nanotubes. Inorganic nanotubes (NTs) have also played an increasingly important role in NT research, with a variety of physical possibilities and promising chemistry. They represent a fast developing field of nanotube investigations and unique area of nanotechnology [12]. In 1996, inorganic nanotubes were first synthesised by chemical transport reaction, which is a standard method for growth of transition metal dichalcogenides [13].

1.2.2. Metal Oxide Nanotubes

The transition metal oxide electrode materials have drawn a great and extensive research attention due to their large specific capacitance, resulting from fast and reversible redox reactions at the surface of active material [14]. Nano-sized metal oxides are expected to improve the high rate capability of cathode materials for lithium-ion batteries because of the considerably higher effective interfacial area between the nano-sized metal oxide and electrolyte and its shorter lithium diffusion path length during charging/discharging [15]. Nanotubular materials, in particular metal oxide nanotubes, have been synthesised experimentally using the so-called template method [16]. The synthesis of metal oxide nanotubes through the template method involves a two-step process: the templates are first coated with the metal oxide and are then removed to yield metal oxides with nanotubular hollow interiors. The metal oxides should form on the templates during coating. The selective coating is needed because if metal oxides were to form in the absence of templates, the nanotube yield would drop. Thus, the template method for synthesising nanostructured transition metal oxide materials is restricted and complicated.

Gong *et al.* [17] synthesised titanium oxide nanotubes using fabricated anodic oxidation of a pure titanium sheet in an aqueous solution containing 0.5 to 3.5wt% hydrofluoric acid. The synthesised nanotubes were found to be well aligned and organised into high-density uniform arrays. While the tops of the synthesised nanotubes were open, the bottoms of the nanotubes were closed, forming a barrier

layer structure similar to that of porous alumina. The sizes of the diameter of the nanotubes were ranging from 25 to 65nm. The diameter was found to increase with an increasing anodising voltage, while the length of the tube was found to be independent of anodisation time.

Unique TiO_2 nanotube arrays (TNAs) grafted with MnO_2 nanosheets were previously synthesised as an anode material for lithium-ion battery. The character of this special structure is that MnO_2 nanosheets were grown on the outer surface, inner surface and tip of the TNAs. The composite combines various advantages from MnO_2 with high capacity (1230mAhg^{-}1) and TNAs with excellent cycle stability and superior electrical conductivity. The MnO_2 nanosheet layer with different thickness on the surface of TNAs was fabricated through controlling hydrothermal reaction time and it was found that the thickness has a significant impact on capacity, cycle performance and conductivity [18].

The structural, electronic and optical properties of anatase TiO_2 nanotubes were investigated using pseudo-potential density-function theory (DFT) calculations [19]. Electronic structure calculations predict a possible band gap modification of TiO_2 nanotube structure as compared to the bulk counterpart. Also, the effect of change in radius dimension on electronic structure was investigated. Yu *et al.* [20] designed TiO_2 nanostructures i.e., nanoparticle, nanotube and nano-sheet and their photocatalytic activity was investigated using first principle simulation methods. The band structure and corresponding density of states for devised nanostructures were calculated. The study predicted the order of photocatalytic activity of TiO_2 nanostructures, with the rank nanosheet > nanotube > nanoparticle which is consistent with theoretical prediction. No work have been reported on simulation of MnO_2 nanotubes.

1.2.3 Nanostrutured Electrode Materials

Nanostructuring battery electrode materials have been shown to enhance performance, due to the large surface-to-volume ratio that allows for a large electrode/electrolyte contact area [21]. Nanostructures with hollow interior channels, have potentially large storage capacity, safety, fast adsorption and fast desorption times compared to their bulk counterparts [22]. Furthermore, generation of nano-

crystallisation has been considered as a useful way to improve the performance of electrode materials. The high performance is achieved by the formation of large surface area, which provides more reaction sites for Li^+ and shorten Li^+ diffusion path length [23]. Ion diffusion path length govern Li-ion transport within cathode materials. Li-ion path length is of considerable interest, considering rates at which a battery can charge and discharge. Presently, the soft chemistry and template methods for synthesising nanostructured electrode materials are complicated and restricted. Hence, it is vital to explore alternative methods of preparing nanostructured electrode materials.

Recent studies have been focused on synthesising 1-dimensional nanostructures and constructing hierarchical structures or networks, which are expected to play an important role in fabricating the next generation of microelectronics and optoelectronics devices since they can function as both building units and interconnectors [24]. Moreover, nanostructured lithium intercalated compounds with various morphologies have been extensively prepared to improve rate capability of lithium-ion batteries due to the present favourable plane of Li^+ ions diffusion for instance, nanoparticle, nanotubes, nanorods and nanowire [25]. Indeed such an improvement is often considered to be achieved at expense of high volumetric energy density, but high volumetric energy-density and high-power are often incompatible requirements.

Nanostructured electrode materials including nanocrystal, nanoporous and nanotubes have been widely investigated to improve the performance of rechargeable lithium-ion batteries [26, 27]. Most of the nanostructured electrode materials are synthesised by a low-temperature treatment process such as soft-chemistry [28], sol-gel [29] and hydrothermal methods [30]. However, the high-temperature sintering process, which is necessary for high-performance cathode materials based on high-quality crystallinity, such as $LiCoO_2$ [31], $LiMn_2O_4$ [32] and $LiFePO_4$ [33]; leads to large-grain size and aggregation which gives poor battery performance. The poor performance results from increasing lithium-ion diffusion length and decreasing effective surface area contact with electrolyte [34]. Hence, experimentally it is still a challenge to

synthesise a high quality single crystal nanostructured electrode materials for high rate lithium-ion batteries.

1.2.3.1 MnO_2 Nanostructures

Nanostructured manganese dioxides have attracted much attention due to their distinctive properties and wide applications as catalysts, sieves, chemical sensors, electrode materials for batteries and electrochemical supercapacitors [35]. MnO_2 is a promising candidate for lithium-ion batteries due to its advantages of low cost, environmental friendliness and superior performance in energy capacity. Developing a simple route to synthesise various phases and shape for MnO_2 nanostructure is of fundamental importance. So far numerous efforts have been devoted to synthesise of MnO_2 nanostructures. However, the phase and morphology of the MnO_2 nanostructures are still not well controlled.

Qiu *et al.* [36] synthesised MnO_2 nanostructures by hydrothermal treatment and investigated their catalytical and electrochemical properties. Cheng *et al.* [37] synthesised MnO_2 nanostructures of different crystallographic types and crystal morphology via a facile hydrothermal route and investigated their electrochemical properties as active cathode materials in primary and secondary batteries. Furthermore, various MnO_2 nanostructures with controlled phase and morphologies, such as α-MnO_2 nanorods, nanocubes and nanowires have been successfully prepared using hydrothermal method, which is simply tuned by changing the ratio of Mn precursor solution to HCl [38]. Wu *et al* established that temperature is a crucial key to get uniform and surface-smooth nanorods. Since, battery performance properties firmly rely on the structure of the materials used, synthesised MnO_2 products proved to have a potential use in energy storage application. Kalubarme *et al.* [39] synthesised MnO_2 nanorods by hydrothermal method, where different morphologies were obtained. Effects of the crystal structure, size and the shape of MnO_2 on their catalytic activity for O_2 reduction were investigated.

Highly ordered MnO_2 nanotube and nanowire arrays were successfully synthesised via an electrochemical deposition techniques using porous alumina templates [40]. The morphologies and microstructures of the MnO_2 nanotube and nanowire arrays were investigated by field emission scanning electron microscopy and transmission electron microscopy. Electrochemical characterisation demonstrated that MnO_2 nanotube array electrode has superior capacitive behavior and high specific capacitance to that of the MnO_2 nanowire array electrode. Luo *at el.* [41] synthesised single-crystal tetragonal α-MnO_2 nanotubes. The samples were characterised by X-ray diffraction and field emission scanning electron microscopy, which showed that the nanotubes have high-quality crystalline and shape dependent optical properties. Wu *et al*. [42] also used electrochemical deposition method to fabricate MnO_2 nanotubes, but the electron diffraction patterns showed that the nanotube has polycrystalline structures. β-MnO_2 nanotubes with diameter ranging 200-500nm and lengths of several micrometer were successfully synthesised using hydrothermal method. This advanced method for synthesising β-MnO_2 nanotube play an important role in controlling the growth of β-MnO_2 nanotubes [43]. Major synthetic difficulties encountered in experimental synthesis of MnO_2 nanostructures in general are poor crystallinity, low yield and process complexity. However, computer simulation methods have proved to be useful in developing strategies for generating MnO_2 nanostructures and investigating their electrochemical properties [44, 45].

MnO_2 nanostructures with morphology and crystal phase were successfully prepared using chemical synthesis and characterised by three-dimensional electron tomography. The growth process of the various MnO_2 nanostructures are correlated to their electrochemical performance. The specific capacitance of MnO_2 electrodes was found to be strongly correlated with the inner morphology and crystal phase of the MnO_2 nanostructures. It was also demonstrated that the increased capacity with electrochemical cycling of the materials is due to the formation of defective regions embedded in the MnO_2 nanostructures; these regions form during electrochemical cycling of the electrodes, resulting in increased porosity, surface area, and consequently, increased electrochemical capacity [46]. Subramanian *et al.* [47] investigated MnO_2 nanostructures with their influence on structural, morphological, compositional and electrochemical properties in electrode materials.

There is growing interest in simulation study of MnO_2 as a promising candidate for Lithium ion battery materials. Sayle *et al*. [45] generated MnO_2 nanoparticle using simulated amorphisation and recrystallisation technique. MnO_2 nanoparticle were amorphised using molecular dynamic simulation method. Among various MnO_2 nanostructures, mesoporous MnO_2 can be used as a reversible positive electrode in rechargeable Li-ion batteries. Atomistic models are valuable since one can explore the models at the atomistic level to observe the openings of the tunnels, deep inside the nanopore system, into which Li inserts. Sayle *et al*. [44] used atomistic simulation method to predict the electrochemical properties of MnO_2 nanomaterial.

1.2.3.2 Spinel $LiMn_2O_4$ Nanostructures

The spinel $LiMn_2O_4$ has been investigated as a promising cathode material for lithium batteries due to its excellent safety, low-cost, non-toxicity, environmental friendliness, easy preparation and excellent voltage profile characteristics [48]. The discharge capacities, rate performance and cycling life are dramatically affected by particle size, surface morphology and synthesis method. It has been widely acknowledged that the high crystallinity of spinel $LiMn_2O_4$ would improve the stability of the crystallographic structure and charge/discharge cycling ability by hindering manganese dissolution from the system into the electrolyte [49, 50]. Thus, it is of great importance to develop facile and systematic methods for synthesising nanostructured $LiMn_2O_4$ with high crystallinity.

Luo *et al.* [51] developed a topochemical method for synthesising $LiMn_2O_4$ nanostructures, including nanorods, nanothorn, microspheres and hollow nanospheres. The method was capable of producing high quality crystalline materials for $LiMn_2O_4$ nanostructures. Sun *et al.* [52] synthesised the powders of single-crystalline $LIMn_2O_4$ with different dimensional nanostructures. XRD and SEM image confirmed that $LiMn_2O_4$ nanostructures were well formed. The effect of nanostructures on the electrochemical properties of $LiMn_2O_4$ cathode was also investigated by controlling the nanostructures of $LiMn_2O_4$, consisting (i) one-dimensional (1-D) nanorods with diameter of 100nm and the length of 1.6 micrometer, (ii) two-dimesional

(2-D) nanoplates with the diameter ranging from 300 to 400nm and the thickness of 20nm and (ii) three dimensional (3-D) octahedral single-crystals with edge length of 1 micrometer. It was observed that 1-D $LiMn_2O_4$ gave best electrochemical properties [52].

Furthermore, single crystalline $LiMn_2O_4$ nanorods have been successfully prepared by solid state reaction. The results of the electrochemical performance showed a good discharge capacity, stability and the good rate capability [53]. Kim *et al.* [54] synthesised single crystalline $LiMn_2O_4$ nanorods using a simple solid-state reaction. The $LiMn_2O_4$ nanorods had an average diameter of 130nm and length of 1.2μm. Galvanostatic battery testing showed that $LiMn_2O_4$ nanorods have a high charge storage capacity at high power rates compared with commercially available powders. More than 85% of the initial charge storage capacity was maintained for over 100 cycles. The structural transformation studies showed that the Li-ions intercalated into the cubic phase of the $LiMn_2O_4$ with a small change of lattice parameter, followed by the coexistence of two nearly identical cubic phases in the potential range of 3.5 to 4.3V. In addition, the developed $LiMn_2O_4$ nanorods showed a higher Coulombic efficiency and also good rate capability attributed to the formation of the single-crystalline spinel $LiMn_2O_4$ with nanorod morphology. The nanorod morphology with high single crystallinity appeared to improve the kinetic properties of the electrode material through a large surface area to volume ratio.

Hosono *et al.* [55] synthesised a single crystalline spinel $LiMn_2O_4$ nanowire for lithium-ion batteries with high power density. This single crystalline spinel $LiMn_2O_4$ nanowire showed high thermal stability and excellent performance at high rate during charging and discharging. Lee *et al.* [56] developed single $LiMn_2O_4$ nanowire using operando electron microscopy. It was observed that $LiMn_2O_4$ has the advantage of preventing capacity fading at high charge rates. $LiMn_2O_4$ nanowires were synthesised using two-steps approach. The prepared $LiMn_2O_4$ nanowires display excellent cyclability. The $LiMn_2O_4$ nanowires with good cycle stability may be beneficial from the structural stability of $LiMn_2O_4$ crystal cell and one-dimensional nanostructure [57]. Nanowire electrodes have some unique advantages for electrochemical energy storage.

However, they are still facing some challenges which significantly affect the performance of electrochemical energy storage device.

The best electrochemical performance of nanoparticles was reported by Shaju and Bruce [58]. They synthesised stoichiometric $LiMn_2O_4$ by one-pot resorcinol-formaldehyde route. The interconnected $LiMn_2O_4$ nanoparticle with diameter of 50nm to 100nm formed a porous structure. This nanocrystalline $LiMn_2O_4$ demonstrated a high initial capacity. The cyclic stability of this material was greatly improved as compared to the conventionally synthesised bulk $LiMn_2O_4$. Also, spinel $LiMn_2O_4$ nanoparticles were synthesised experimentally using hydrothermal reaction method. The electrochemical performance of $LiMn_2O_4$ nanoparticles towards Li insertion/extraction was examined. It was observed that $LiMn_2O_4$ nanoparticle synthesised has good capacity, cycle performance and excellent high rate capability [59].

Single-crystalline nanotubes of spinel $LiMn_2O_4$ with a diameter of about 600nm, a wall thickness of about 200nm and a length of 1-4μm have been synthesised via a template-engaged reaction using β-MnO_2 nanotubes as a self-sacrifice template. In this fabrication, a minimal structural reorganisation can be responsible for the chemical transformation from [001]-oriented β-MnO_2 template to [110]-oriented $LiMn_2O_4$ [60], Results reveal that single-crystalline nanotubes of $LiMn_2O_4$ will be one of the most promising cathode materials for high-power lithium-ion batteries. Lastly, spinel $LiMn_2O_4$ nanotube with {400} plane was synthesised using multiwall carbon nanotubes as a sacrificial template. Because of nanostructure and preferred orientation, the nanotube showed superfast second-level charge capability as a cathode material for rechargeable lithium-ion battery [61]. From the literature it is established that various experimental methods have been used to synthesise spinel $LiMn_2O_4$ nanostructures. However, there is no computer simulation work reported on generating spinel $LiMn_2O_4$ nanostructures, in particular, nanotubes.

1.3 Structural Aspects

1.3.1 MnO_2 Structure

Manganese dioxide is a non-stoichiometric compound which has many crystalline polymorphs such as hollandite, pyrolusite, ramsdellite, etc. Pyrolusite (β-MnO_2) is the most stable polymorph of manganese dioxide and it has a rutile structure, isostructural to TiO_2. The most commercially important form, γ-MnO_2, is used as a cathode material of choice for aqueous zinc batteries, alkaline batteries and lithium-ion batteries. Pyrolusite is described as an infinite single chains of edge sharing octahedral, which are connected to other single chains as shown in figure 3. The β-MnO_2 is known to be the least reactive and the most highly crystalline form of manganese dioxide.

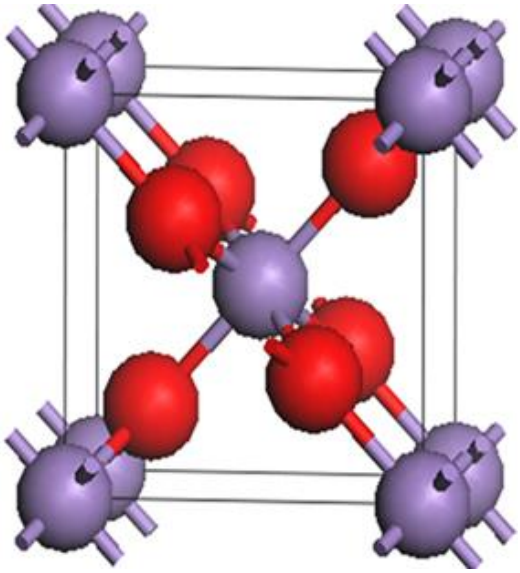

Figure 3: Schematic representation of MnO_2 pyrolusite structure. Different atoms are represented by balls and sticks for bonds, where red balls are oxygen atoms and purple are manganese atoms.

The oxygen atoms form a slightly distorted hexagonal closed packed (hcp) array; half the closed-packed rows of octahedral interstices are occupied by Mn^{4+}. The average bond distance between Mn and O atoms is 1.88Å and pyrolusite has space group $P4_2/mnm$. Manganese dioxide is the inorganic compound with the formula MnO_2. This blackish or brown solid occurs naturally as the mineral pyrolusite. MnO_2 has a tetragonal shape with lattice constant a = b = 4.398Å, c = 2.873Å and volume V = 55.581$Å^3$ with molar mass of 86.9368g/mol. MnO_2 crystal structure is insoluble in water with melting-point of approximately 535^oC. At a higher temperature close to

1000^{o}C the mixed-valence compound Mn_3O_4 forms. The atomic position of Wyckoff position for Mn is 2a and O is 4f.

1.3.2 Spinel $LiMn_2O_4$ Structure

The crystal structure of spinel was firstly discovered by Bragg [62] and Nishikawa [63] independently in 1915. The normal spinel structure of the general chemical formula $(A)_{tet}[B_2]_{oct}O_4$ belong to the group Fd-3m, which has A cations on the tetrahedral sites and B cations on the octahedral sites. The spinel structure consists of cubic closed-packed oxide ions, with Mn^{3+}/ Mn^{4+} ions in one-half of the octahedral site and Li^{+} in one-eighth of the tetrahedral sites. In the spinel $LiMn_2O_4$, Li-ions occupy tetrahedral (8a) sites, Mn ions ($Mn^{3+/}Mn^{4+)}$ octahedral (16d) sites and O^{2-} ions octahedral sites as shown in figure 4.

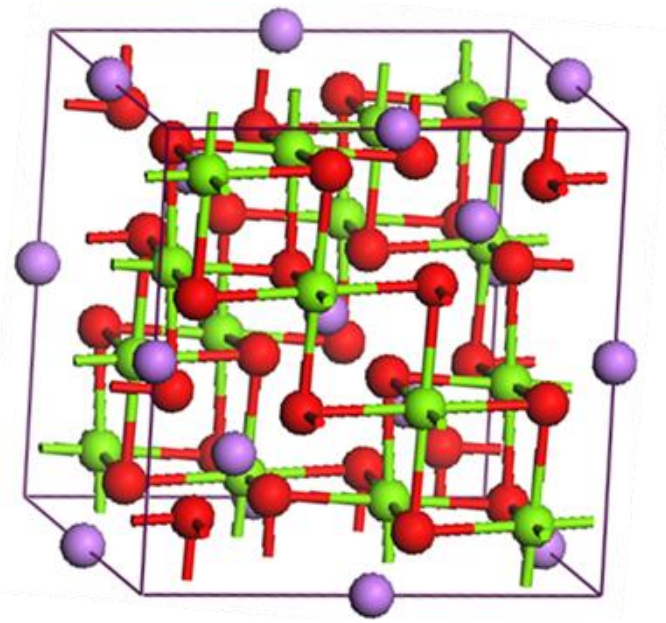

Figure 4: Schematic representation of spinel $LiMn_2O_4$ structure. Different atoms are represented by balls and sticks for bonds, where red balls are oxygen atoms, purple balls are manganese atoms and green are lithium atoms.

The edge-share octahedral Mn_2O_4 host structure is highly stable and possesses a series of intersecting tunnels formed by the face-sharing of tetrahedral lithium (8a) site and empty octahedral (16c) sites. Such tunnels allow the three–dimensional diffusion of lithium ions. The lithium intercalation/deintercalation into/from the 8a tetrahedral

sites occurs at about 4V. Spinel $LiMn_2O_4$ is a brown-black solid with submicron, narrow-size-distribution. Pure-phase particles of $LiMn_2O_4$ can be synthesised by ultrasonic spray pyrolysis method from an aqueous lithium nitrate and manganese acetate solution. $LiMn_2O_4$ with a three-dimensional crystal structure is at present a very prospective candidate for cathode materials for lithium-ion batteries. However, the electrochemical performance of $LiMn_2O_4$ is intimately related to its phase purity, crystallinity, particle size and morphology.

1.4 Motivation

Due to the rapid industrial development and growing population, along with the increase in energy demand, the global energy consumption has been accelerating at an alarming rate. At current consumption rate, global energy exhaustion will become inevitable. To prevent disaster caused by energy exhaustion, the need for renewable energy sources has attracted tremendous attention globally. In order to make the effective use of renewable energy, it is important to develop high-performance, low-cost and environmental friendly energy storage and conversion systems. Adopting renewable energy on a grand scale is a monumental task that requires next generation technologies born out of breakthrough discoveries that push the boundaries in materials science, physics, chemistry and engineering.

Rechargeable lithium batteries are already a major worldwide success and are used in portable electronic devices. Despite intensive effort, it has proved impossible to scale-up such first generation batteries for renewable energy storage or transport applications. The major problem lies with the $LiCoO_2$ positive electrode, which is too expensive, toxic and unsafe when used in larger batteries. To address the energy storage challenge, we investigate MnO_2 and $LiMn_2O_4$ nanotubes as electrode materials for application in lithium-ion batteries. Such electrode materials would be attractive for smart grids and renewable energy storage and their high-power would be particularly attractive for hybrid electric vehicles. Development of nanotubes is growing rapidly; yielding new forms, new applications and new materials based on these unique structures. Furthermore, manganese based oxide cathode materials emerged as most reliable in terms of optimum voltage, tolerance to abuse and low cost.

1.5 Objectives

The objectives of this study are to:

i. generate MnO_2 and spinel $LiMn_2O_4$ nanotubes with different Miller index, symmetry, size and diameter
ii. investigate the effect of diameter and Miller index on generated nanotube structures
iii. determine the stability of nanotubes
iv. calculate XRD patterns for MnO_2 and spinel $LiMn_2O_4$ nanotubes
v. use molecular dynamics simulation to investigate the structural properties
vi. investigate the effect of temperature on structural properties of the nanotubes using molecular dynamics.

1.6 Outline of the Dissertation

Chapter 1: Gives background information on Li-ion batteries, origin of nanotubes structure, metal oxide nanostructures, application of nanostructures as electrode materials, structural properties of MnO_2 and $LiMn_2O_4$. Also gives a brief motivation for the study and objectives of the study.

Chapter 2: Describes the methods that have been employed in this study. Firstly, Ab initio method employed is introduced, particularly, Density Functional Theory. Followed by the discussion on approximations applicable to this study, i.e. the Generalized Gradient Approximation and the Local Density Approximation. In addition, Molecular Dynamics method is discussed. Computer codes used are described briefly. Most importantly, the description on how the nanotubes are created is presented.

Chapter 3: Gives detailed results and discussions on generated MnO_2 nanotubes with various Miller indices and diameters of different sizes. Physical properties such as structural properties, radial distribution functions, XRD patterns and temperature dependences are discussed.

Chapter 4: As in the previous chapter, this chapter presents results based on spinel $LiMn_2O_4$ nanotubes. Similar properties are presented.

Chapter 5: Summarises key findings, make a conclusion and recommendations for future work.

Chapter 2

Methodology

2.1 Theoretical Methodologies

The developments of theoretical concepts and computational approaches for atomistic simulations have been a major part of solid-state physics, chemistry and materials science. There are two ways to study the ground-state properties and excitation spectrum of a many-body electron system.

(i) Empirical potential or force field approach, which describe the interactions between the atoms in a quasi-classical from avoiding any details of the electronic structure.

(ii) Non-empirical quantum mechanical methods that take into account the motion and interactions of the electrons in the system.

The first-principle approach includes the ab initio methods which are computationally intensive and cannot be readily applied to large molecules of interest.

2.2 *Ab initio* Method

Ab initio is the first principle method that requires only a specification of the ion present. The techniques use no experimental parameters in their computation. *Ab initio* computations provide high quality quantitative predictions for a broad range of systems. They can handle any type of atom, including metals. The starting point for the *ab initio* simulations is the optimised nuclear configuration, which can be obtained by using molecular mechanics method. The advantage of this method is that potential parameters can be calculated for systems where there is insufficient or unavailable experimental data.

2.2.1 Density Functional Theory

For inorganic solids, the most widely used theoretical framework for accurate calculations of a system's electronic ground state is density functional theory (DFT). Density functional theory, develop by Hohenberg and Kohn in 1964 [64] and Kohn and Shan in 1965 [65], is a quantum mechanical theory used in physics and chemistry to

investigate the electronic structure of many-body systems, in particular atoms, molecules and condensed phases.

DFT is among the most popular and versatile methods available in condensed-matter physics, computational physics and computational chemistry. At the minimum; the Kohn-Sham energy functional is equal to the ground-state energy of the system of electrons with the ions in positions {R_I}. It is necessary to determine the set of wave functions φ_I that minimises the Kohn-Sham energy functional. These are given by the self-consistent solutions to the Kohn-Sham equation

$$[\frac{-\hbar^2}{2\mathrm{m}}\nabla^2 + \mathrm{V_{ion}(r)} + \mathrm{V_H(r)} + \mathrm{V_{XC}(r)}]\varphi_\mathrm{i}(\mathrm{r}) = \varepsilon_\mathrm{i}\varphi_\mathrm{i}(\mathrm{r}) \quad (1)$$

where φ_I is the wave-function of electronic state I, ε_i is the Kohn-Sham eigenvalue, and V_H is the Hartree potential of the electrons [66]. The Kohn-Sham total energy functional for a set of doubly occupied electronic states φ can be written as:

$$E = \{\varphi_i\} = 2\sum\left(-\frac{\hbar^2}{2m}\right)\nabla^2\varphi_i d^3r + \int V_{ion}n(r)d^3r + \frac{e^2}{2}\int\frac{n(r)n(r)}{|r-r'|}d^3rd^3r + E_{xc}[n(r)] + E_{ion}(\{R_I\}) \quad (2)$$

where E_{ion} is the Coulomb energy associated with interactions among the nuclei (or ions) at positions {R_I}, V_{ion} is the static total electron-ion potential, and $n(r)$ is the electronic density given by:

$$n(r) = 2\sum_i|\varphi_i(r)|^2 \quad (3)$$

where $E_{xc}[n(r)]$ is the exchange-correlation functional. Hence the name Density functional theory comes from the use of functional of the electron density. Although DFT has its conceptual roots in the Thomas-Fermi model, it was put on affirm theoretical footing by the two Hohenberg-Kohn theorems [65]. The theorems proven in their report represent the major theoretical pillars on which all modern day density functional theories are erected. The Hohenberg-Kohn theorems relate to any system

consisting of electrons moving under the influence of an external potential$V_{ext}(r)$. The first Hohenberg-Kohn theorem states as follows: The external potential $V_{ext}(r)$ is a unique functional of the $\rho(\overrightarrow{r})$ since in turn $V_{ext}(\vec{r})$ fixes **H** such that the full many particle ground state is a unique of $\rho(\overrightarrow{r})$. In other words, there is unique relation of the external potential $V_{ext}(\vec{r})$ within N electron system and its (ground state) electron density $\rho(\overrightarrow{r})$.

$$V_{ext}(\vec{r}) \Rightarrow \rho(\vec{r}\,) \tag{4}$$

and this inverse mapping exists

$$\rho(\vec{r}\,) \Rightarrow V_{ext}(\vec{r}) \tag{5}$$

The density $\rho(\vec{r}\,)$ contains all the information of the system, meaning every property, even the ones of electronically excited states, could be calculated with the help of $\rho(\vec{r}\,)$.

Suppose there are two different external potentials $V_{ext}(\vec{r})$ and $V_{ext}(\vec{r})'$ which differ by more than a constant and give rise to the same density $\rho(\vec{r}\,)$ associated with the (non-degenerated) ground state φ_0, then

$$V_{ext}(\vec{r}\,) \neq V_{ext}(\vec{r})' \tag{6}$$

and

$$\delta[V_{ext}(\vec{r}\,)] = \rho(\vec{r}\,) = \delta[V_{ext}(\vec{r})'] \tag{7}$$

since both external potentials differ, they lead to two different Hamiltonians $\hat{\mathbf{H}}$, with two different ground state wavefunctions φ

$$H = H_0 + V_{ext};\ H\varphi = E\varphi \tag{8}$$

$$H' = H_0 + V'_{ext};\ H'\varphi' = E'\varphi' \tag{9}$$

Therefore φ and φ' are different N particle wavefunctions and using the variational principle one can write the inequality

$$E = \left(\varphi \left|\tilde{\mathbf{H}}\right| \varphi\right) < \left(\varphi' \left|\tilde{\mathbf{H}}\right| \varphi'\right) = \left(\varphi' \left|\tilde{\mathbf{H}}'\right| \varphi'\right) < \left(\varphi' \left|\tilde{\mathbf{H}} - \tilde{\mathbf{H}}'\right| \varphi'\right). \quad (10)$$

Because the two Hamiltonians differ only by the external potential

$$E < E' + (\varphi'|V_{ext} - V'_{ext}|\varphi') \quad (11)$$

which yields

$$E < E' + \int \rho(\vec{r}\,)\{V_{ext} - V'_{ext}\}d\vec{r} \quad (12)$$

The last transformation is based on the fact that the external field interacts only via a classical electrostatic interaction between the negatively charged and the positive charges of the nuclei. Interchanging the primed and the primed quantities; and repeating the steps above leads two the corresponding equation:

$$E < E' + \int \rho(\vec{r}\,)\{V'_{ext} - V_{ext}\}d\vec{r} \quad (13)$$

Adding the two equations leaves the clear contradiction

$$E' + E < E + E' \quad (14)$$

from which it can be concluded that there cannot be two different external potentials V_{ext} and V'_{ext} that yield the same density $\rho(\vec{r}\,)$. Since the complete ground state energy E_0 is a unique functional of the density ρ, so must be its individual parts. One can write

$$E_o[\rho] = T[\rho] + V_{int}[\rho] + V_{ext}[\rho] \quad (15)$$

This expression can be classified by parts depended on the actual system (determined by the external potential) and parts which are universal in the sense that the form of the functional is independent of N, R_A and Z_A.

$$E_o[\rho] = V_{ext}[\rho] + T[\rho] + V_{int}[\rho] \quad (16)$$

where the system independent part defines the Hohenberg-Kohn functional

$$F_{HK}[\rho] = T[\rho] + V_{int}[\rho] \quad (17)$$

The second Hohenberg-Kohn theorem is nothing else than the variational principle formulated for densities. Given any density $\breve{\rho}$ associated to an N electron system with external potential V_{ext}, one can state that;

$$E_o \leq E[\breve{\rho}] = T[\breve{\rho}] + V_{int}[\breve{\rho}] + V_{ext}[\breve{\rho}] \quad (18)$$

with the equal sign only valid if $\breve{\rho} = \rho$

2.2.2 Local Density Approximation

The Hohenberg-Kohn theorem provides some motivation for using approximate methods to describe the exchange-correlation energy as a function of the electron density. The simplest method of describing the exchange-correlation energy of an electronic system is to use the local density approximation (LDA). In local density approximation the exchange-correlation energy of an electronic system is constructed by assuming the exchange-correlation energy per electron at a point *r* in the electron gas. Within the LDA one assumes the density functional of an N particle system can be expressed in the following form:

$$\mathrm{E}_{\mathrm{XC}}^{\mathrm{LDA}}[\rho] = \int \rho(\overrightarrow{\mathrm{r}})\mathcal{E}_{\mathrm{XC}}\ (\rho(\overrightarrow{\mathrm{r}}))(\vec{\mathrm{d}}(\overrightarrow{\mathrm{r}})), \quad (19)$$

where ρ is the electronic density and $\mathcal{E}_{XC}(\rho(\vec{r}))$ is the exchange-correlation energy per particle of a uniform electron gas. The local density approximation assumes that the exchange-correlation energy functional is purely local. In principle, LDA ignores correction to the exchange-correlation energy at a point *r* due to nearby inhomogeneities in the electron density. The LDA is a first-principle approach in the

sense that the quantum mechanical problem solved without any adjustable, arbitrary or system dependent parameters [67].

2.2.3 Generalized Gradient Approximation

Generalized Gradient Approximation (GGA) is the functional of the form,

$$\mathrm{E}_{\mathrm{xc}}^{\mathrm{GGA}}[\mathrm{n}_{\uparrow}, \mathrm{n}_{\downarrow}] = \int \mathrm{f}\big(\mathrm{n}_{\uparrow}(\mathrm{r}), \mathrm{n}_{\downarrow}(\mathrm{r}), \nabla \mathrm{n}_{\uparrow}(\mathrm{r}), \nabla \mathrm{n}_{\downarrow}(\mathrm{r})\big), \tag{20}$$

that depends not only on the density at a particular coordinate r but also take into account the gradient of density at the same co-ordinate [68], there exist an explicit dependence of the integral f on the densities and their gradients [69]. The generalized gradient approximation [70] adds the gradient of the density, as an independent variable. The gradient introduces non-locality into the description of exchange and correlation. The GGA still entails some locality however it also takes into account the gradient of the density, the density at the same coordinates as given by:

$$\mathrm{E}_{\mathrm{xc}}[\mathrm{n}_{\uparrow}, \mathrm{n}_{\downarrow}] = \int \varepsilon_{\mathrm{xc}}(\mathrm{n}_{\uparrow}, \mathrm{n}_{\downarrow}, \nabla \mathrm{n}_{\uparrow}, \nabla \mathrm{n}_{\downarrow}) \rho(\mathrm{r}) \mathrm{d}^3\mathrm{r}, \tag{21}$$

where $\varepsilon_{\mathrm{xc}}$ is the exchange correlation energy, ∇n is the gradient term and $n_{\uparrow}$ and $n_{\downarrow}$ are spin up and spin down densities respectively. GGA functional have evolved in two main orientations, which one sometimes referred to as the ‘parameter free’, where the new parameters are determined from known expansion coefficients and other exact theoretical conditions, and the second is empirical, with parameters determined from fits to experimental data or accurately calculated atomic and molecular properties. The GGA functional most commonly used in physics, Perdew, Burke and Ernzerhof (PBE) and Perdew – Wang from 1991 (PW91), are parameter free [71]. Most GGAs used in chemistry applications, such as Becke, Lee, Parr and Yang (BLYP), are empirical [72].

2.2.4 Plane-wave Pseudopotential Method

Among a variety of different ways of describing the crystal orbital, one widely used implementation of DFT combines a plane-wave basis set with the pseudopotential method, in which the pseudopotential replace the nuclear potential and the inert core electrons, so that only valence electrons are included explicitly in the calculation. The plane-wave pseudopotential method has become a powerful and reliable tool to study the properties of a broad class of materials. The emphasis on the total energy and the related properties makes plane-wave pseudopotential a technique suited to structural studies based on a quantum-mechanical treatment of the electronic subsystem. The main idea of the method is to simplify the DFT problem by considering only valence electrons.

2.2.4.1 Plane-Wave Basis

An infinite plane-wave basis set is used to expand the electronic wave functions of the system. The method is described well by using Bloch's theorem, which state that the electronic wave function at each k-point can be expanded in terms of a discrete plane-wave basis set

$$\Psi_{ki}(r) = \exp[ik.r]\, f_i(r) \tag{22}$$

This expression has a wavelike and cell-periodic part. The function $f_i(r)$ defines the periodicity of the solid and can be expanded using a basis set with a discrete set of plane waves, written as:

$$f_i(r) = \sum C_i G^{[iG.r]} \tag{23}$$

where the G are the reciprocal lattice vectors of the periodic cell. Thus each electronic wave function can be written as a sum of plane waves:

$$\Psi_{ki}(r) = \sum C_{i,k} + G^{[i(k+G).r]} \tag{24}$$

where $C_{i,k+G}$ are the coefficients for the plane waves that need to be solved and depend entirely on the specific kinetic energy,

$$\frac{\hbar^2}{2m}|K+G|^2 \tag{25}$$

The convergence of this expansion is controlled by the choice of the kinetic energy cut-off. In practice, the plane wave basis set is limited by including all plane waves whose kinetic energies are less than some particular cut-off energy E_{cut}. Introduction of an energy cut-off to the discrete plane wave basis set produces a finite basis set. The truncation of the plane wave basis set at finite cut-off energy will lead to an error in the computed total energy. However, it is possible to reduce the magnitude of the error by increasing the value of the cut-off energy. In principle, the cut-off energy should be increased until the calculated total energy has converged.

2.2.4.2 Pseudopotential Method

The physical properties of solids are dependent on the valence electrons to a much greater extent than on the core electrons. In the pseudopotential method, the core electrons and the strong attractive Coulomb potential inside the ionic core are replaced by a weaker pseudopotential that describes all the salient features of a valence electron moving through a crystal, including relativistic effects. Thus, the original solid is now replaced by pseudovalence electron and pseudoion cores. These pseudoelectrons experience exactly the same potential outside the core region as the original electrons but have a much weaker potential inside the core region. Figure 4 illustrates the ionic potential (Z/r), the valence wave function (v), the corresponding pseudopotential (Vpseudo) and pseudowave function (pseudo).

The valence wave functions oscillate rapidly in the region occupied by the core electrons due to the strong ionic potential in this region. The oscillations maintain the orthogonality between the core and valence wave functions, which is required by the exclusion principle. The pseudopotential is constructed ideally, so that its scattering properties or phase shifts for the pseudo wave functions are identical to the scattering properties of the ion and the core electrons for the valence wave functions, but in such a way that the pseudo wave functions have no radial nodes in the core region. In the core region, the total phase shift produced by the ion and the core electrons will be

greater by π, for each node that the valence functions had in the core region, than the phase shift produced by the ion and the valence electrons. Outside the core region the two potentials are identical, and the scattering from the two potential is indistinguishable.

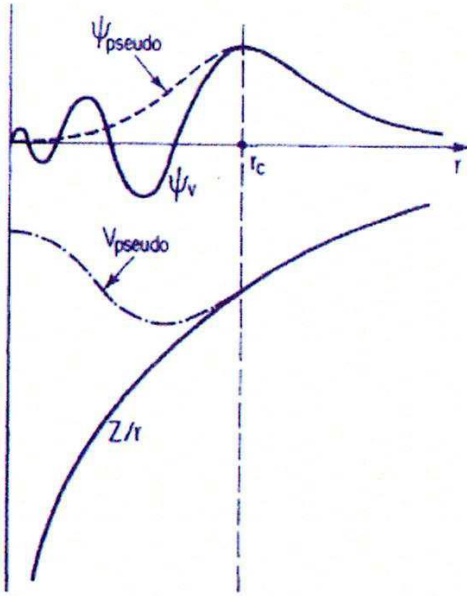

Figure 5: Schematic illustration of all-electron potential (solid line) and pseudoelectron potential (dashed line) with the corresponding valence wave function (v) and pseudowave function (pseudo) [73].

2.2.4.3 Brillouin Zone

Brillouin zone corresponds to primitive cells of a different type that come up in the theory of electronic levels in a periodic potential. Most of all the calculations in crystals involve the averaging over the Brillouin zone of periodic functions of wave vector. Such calculations are often long and complicated and in principle require knowledge of the value of the function at each k-point in the Brillouin zone [74]. Electronic states are allowed only at a set of k-points determined by the boundary conditions that apply to bulk solid. Due to Bloch theorem, the infinite number of electrons in the solid is accounted for by an infinite number of k-points and only a finite number of electronic states are occupied at each k-point. The occupied states at each k-point contribute to the electronic potential in the bulk solid so that, in principle, an infinite number of calculations are needed to compute this potential. All required functions of k, in particular the potential are continuous so the integral over the infinite number of k-points can be replaced by a sum over a finite, often small number. Density functional theory approximates the k-space integrals with a finite sampling of k-points. Special k-

point schemes have been developed to use the fewest possible k-points for a given accuracy, thereby reducing the computational cost.

2.3 Molecular Dynamics

Molecular dynamics (MD) is a computer simulation technique where the time evolution of a set of interacting atoms is followed by integrating their equations of motion. MD is one of the most widely used theoretical tools for studying the molecular behaviour of fluids and solids. The method allows the prediction of the static and dynamic properties of molecules directly from the underling interactions between the molecules.

In molecular dynamics, successive configurations of the system are generated by integrating Newton's laws of motion. The result is a trajectory that specifies how the positions and velocities of the particles in the system vary with time. The trajectory is obtained by solving the differential equations embodied in Newton's second law of motion:

$$\vec{F} = \vec{m}\vec{a} \tag{26}$$

This equation describes the motion of a particle of mass m_i along one coordinate (x_i) with F_{x_i} being the force on the particle in that direction. Starting from the knowledge of molecular interactions, the simulation provides structural information as well as thermodynamics and transport properties of liquid and solid states. MD simulation generates a trajectory that describes how the dynamic variables change with time. They are typically run for tens or hundreds of picoseconds (a 100ps simulation using a 1fs time step requires 100 000 steps).

MD methods are used in solid-state physics, with applications in studies of ionic properties, modelling of phase transition and elucidating the structure and dynamical correlations. The simulations are traditionally performed under conditions of constant number of particles (N), volume (V) and energy (E) (the constant NVE or microcanonical ensemble). But it can also be adapted to simulate from the canonical ensemble, and two other common ensembles, which are isothermal-isobaric (fixed NPT) and grand canonical (fixed μVT). Molecular dynamics simulations generate information at the microscopic level, including atomic positions and velocities. The

forces acting upon the atoms are originated by the interactions and the atoms move under the action of the instantaneous force. The positions and forces change as the atoms move.

The default integrator of the equations of motion is based on the Verlet algorithm (discussed in the next section), which allows for very useful extensions of the MD scheme, as for example introducing constraints or extended Lagrangian formalisms.

2.3.1 Verlet Algorithm

In molecular dynamics, the most commonly used time intergration algorithm is the so called Verlet algorithm. The basic idea is to write two third-order Taylor expansions for the positions $r(t)$, one forward and one backwards in time. Calling v velocities, a the accelerations and b the third derivatives of r with respect to t, one has:

$$r(t+\Delta t) = r(t) + v(t)\Delta t + \frac{1}{2}\boldsymbol{a}(t)\Delta t^2 + \frac{1}{6}b(t)\Delta t^3 + o(\Delta t^4) \quad (27)$$

$$r(t-\Delta t) = r(t) - v(t)\Delta t + \frac{1}{2}\boldsymbol{a}(t)\Delta t^2 - \frac{1}{6}b(t)\Delta t^3 + o(\Delta t^4) \quad (28)$$

Adding the two expressions gives

$$r(t+\Delta t) = 2r(t) - r(t-\Delta t) + \boldsymbol{a}(t)\Delta t^2 + 0(\Delta t^4) \quad (29)$$

This is the basic form of the Verlet algorithm. This is the one of the most important test to verify that a MD simulation is proceeding correctly. The velocities do not explicitly appear in the Verlet algorithm and can be calculated by dividing the difference in positions at times $t + \Delta t$ and $t - \Delta t$ by $2\Delta t$, that is:

$$v(t) = \frac{r(t+\Delta t) - r(t-\Delta t)}{2\Delta t} \quad (30)$$

2.3.2 Velocity Verlet Algorithm

This algorithm yields positions, velocities and accelerations at time t. The advantage of velocity Verlet algorithm is that it provides a more accurate expression for the velocities. At the first stage the velocities are advanced to $t + (1/2)\Delta t$ by integration of the force:

$$\boldsymbol{v}\left(t + \frac{1}{2}\Delta t\right) = \boldsymbol{v}(t) + \frac{1}{2}\Delta t \frac{\boldsymbol{F}(t)}{m} \tag{31}$$

where m is the mass of a site and δt is the timestep. The positions are then advanced to a full step $t + \Delta t$ using the new half-step velocities:

$$r(t + \Delta t) = r(t) + \Delta t \boldsymbol{v}\left(t + \frac{1}{2}\Delta t\right) \tag{32}$$

A recalculation of the force at time $t + \delta t$ is required since the positions have changed

$$\boldsymbol{F}(t + \Delta t) = \boldsymbol{F}(t) \tag{33}$$

In the second stage the half-step velocities are advanced to a full step using the new force

$$\boldsymbol{v}(t + \Delta t) = \mathrm{v}\left(t + \frac{1}{2}\Delta t\right) + \frac{1}{2}\Delta t \frac{\boldsymbol{F}(t+\Delta t)}{m} \tag{34}$$

2.3.3 Leap-frog Algorithm

Leap-frog algorithm uses the following relationships:

$$\mathrm{r}(t + \Delta t) = \mathrm{r}(t) + \Delta t \mathrm{v}\left(t + \frac{1}{2}\Delta t\right) \tag{35}$$

$$\mathrm{v}\left(\mathrm{t} + \frac{1}{2}\Delta \mathrm{t}\right) = \mathrm{v}\left(\mathrm{t} - \frac{1}{2}\Delta \mathrm{t}\right) + \mathrm{a(t)}\Delta \mathrm{t} \tag{36}$$

The velocities are first calculated at time $t + \frac{1}{2}\Delta t$; these are used to calculate the positions, r at time $t + \Delta t$. In these way, the velocities leap over the positions, then positions leap over the velocities. The velocities at time *t* can be calculated from

$$v(t) = \frac{1}{2}\left[v\left(t + \frac{1}{2}\Delta t\right) + v(t - \frac{1}{2}\Delta t)\right] \quad (37)$$

The advantage of this algorithm is that the velocities are explicitly calculated. However, most practical cases occur under conditions wherein the system is exposed to external influences such as a change in temperature and pressure. Because of these influences the total energy of the system under study is no longer conserved, hence extended forms of molecular dynamics are required. Several methods are available for controlling temperature and pressure where specific ensembles are selected in order to calculate structural, energetic and dynamic properties of the system.

There are three ensembles of statistical mechanics, the microcanonical ensemble, the canonical ensemble and the grand canonical ensemble. The microcanonical or constant-NVE ensemble system (a solid, liquid or a gas) which is completely isolated from its surroundings has constant energy E and a constant number of particles N contained at constant volume V. The canonical or constant-NVT ensemble is generally the most useful in practice since we most often deal with systems in thermal equilibrium (constant T) with their surroundings. The energy states fluctuate and there is a probability of observing the system in a given energy state at constant T. The canonical ensemble considers system (a solid, liquid or a gas) in contact with a heat bath at constant temperature. A canonical ensemble is an assembly of mental copies of this system. Since energy can be transferred between the system and the heat bath, the energy of the systems in the assembly differ. Other commonly used ensemble is the grand canonical ensemble, which considers an open system in contact with a heat and particle bath. The system is open meaning that particles as well as heat can be exchanged between the bath and the system.

2.3.4 Energy

MD method is used in the simulation of kinetic and thermodynamic properties of molecular systems using Newton equations of motion, for a specific interatomic potential, with certain initial condition and boundary conditions. The internal energy is given by equation (38) below:

$$\mathrm{E} = \mathrm{K} + \mathrm{U} \quad (38)$$

where K is the kinetic energy and is given by:

$$\mathrm{K} = \sum_{\mathrm{i}=1}^{\mathrm{N}} \frac{1}{2} \mathrm{M_i} |\dot{\mathrm{x}}_\mathrm{i}(\mathrm{t})|^2 \quad (39)$$

and U is the potential energy given by the expression:

$$\mathrm{U} = \mathrm{U}(\mathrm{x}^{3\mathrm{N}}(\mathrm{t})) \quad (40)$$

where $x^{3N}(t)$, denotes the collective of 3D co-ordinates.

The Helmholtz (canonical ensemble) free energy is defined as:

$$\mathrm{F} = \mathrm{E} - \mathrm{TS} \quad (41)$$

where E and S are the energy and entropy of a system respectively. Relative free energies determine the relative stability of different states of a system whereas the free energy barriers determine the rates of transitions between different states. Therefore, atomic simulations allowing estimation of the relative free energies are of great importance. The standard techniques for calculating free energy differences include the so-called thermodynamic integration and thermodynamic perturbation methods. Both approaches usually imply a series of MD or Monte Carlo (MC) simulations (for intermediate states) with extensive sampling and they are computationally very intensive.

2.3.5 Temperature

In molecular dynamics there is no simple way of assigning a temperature to the system in advance. Instead, the temperature is calculated from the kinetic energy of the particles. For each translational degree of freedom (not including molecular rotation),

the average kinetic energy is $\frac{\mathrm{KT}}{2}$. Assuming that any bulk flow (translational and rotational) has been removed, for a 2-D simulation,

$$KT = \frac{1}{2} < V^2 > \tag{42}$$

which in other units is,

$$T = \frac{1}{2} < V^2 > \tag{43}$$

In the microcanonical ensemble, however, the temperature will fluctuate. The temperature is directly related to kinetic energy of the system as follows:

$$\chi = \sum_{\mathrm{i}=0}^{\mathrm{N}} \frac{|\mathrm{p_i}|^2}{2\mathrm{m_i}} = \frac{\mathrm{k_B T}}{2}(3\mathrm{N} - \mathrm{N_c}) \tag{44}$$

In equation (44), p_i is the total momentum of the particle i and m_i is its mass. According to the theorem of the equipartition of energy, each degree of freedom contributes $\frac{k_B T}{2}$. If there are N particles, each with degree of freedom, the kinetic energy should equal $\frac{3Nk_BT}{2}$.

In MD simulations the total linear momentum of the system is often constrained to a value of zero, which has the effect of removing three degrees of freedom from the system and so N_c would be equal to 3. In thermal equilibrium, there is a Maxwellian distribution of particle velocities. This can be described by random selection of a Maxwell-Boltzmann distribution at the temperature of interest, such that:

$$P(v)\partial(v) = \left(\frac{2}{2\pi KT}\right)^{\frac{3}{2}} e^{\left(\frac{-2mv^2}{2KT}\right)} 4\pi v^2 \partial v \tag{45}$$

$P(v)$ is the probability of velocity *v*, *m* is the mass of particle, *v* is the velocity of the particle, T is the temperature and k is Boltzmann constant. However, due to fluctuations, the temperature determined from summing over the particle energies will also fluctuate. Therefore, after equilibrium is established, a time-averaged temperature is calculated.

2.3.6 Radial Distribution Functions

The radial distribution function (RDF) is an example of a pair correlation function, which describes how, on average, the atoms in a system are radially packed around each other and is given by:

$$g_{ij}(r) = \left[\frac{<n_{ij}(r)>}{(\rho 4\pi r^2 \Delta r)}\right] \quad (46)$$

Where *g(r)* is the RDF, *n(r)* is the mean number of atoms in a shell of width *Δr* at distance r and *ρ* is the mean atom density. The method needs not be restricted to one atom. All the atoms in the system can be treated in this way, leading to an improved determination of the RDF as an average over many atoms. This proves to be a particularly effective way of describing the average structure of disordered molecular systems such as liquids. Also in liquid systems, where there is continual movement of the atoms and a single snapshot of the system shows only the instantaneous disorder, it is extremely useful to be able to deal with the average structure.

The pair distribution function g(r), gives the probability of finding an atom (molecule, if simulating a molecular fluid) a distance r from another atom (molecule). Compared to the ideal gas distribution, g(r) is thus dimensionless. Higher radial distribution functions (e.g. the triplet radial distribution function) can also be defined but are rarely calculated and so references to the radial distribution function are usually taken to mean the pairwise version. In a crystal, the radial distribution function has an infinite number of sharp peaks whose separations and heights are characteristics of the lattice structure. The radial distribution function of a liquid is intermediate between the solid and the gas, with a small number of peaks as short distances.

2.4 Potential Model

The potential includes two-body, three-body and four-body interaction energies and each one consisting of exponential exchange and dispersion terms taken from perturbation theory up to the fourth order. The proposed potential and its first derivatives are incorporated in the molecular dynamics simulation code. The simulations contained in this work make use of a pair-wise description for atom interactions. The basis of this method is to calculate the total interaction energy, often called the lattice energy of the system under study. It uses parameterised analytical functions to describe the interactions between all species in the system. When simulating ionic lattices both long range and short range interactions are accounted. The potential model has the long-range electrostatic interaction $(\mathrm{U_{LR}})$ and the short-range interaction that acts mainly as a repulsive force that prevents two oppositely charged ions from colliding to form a singularity. This short-range interaction may also contain an attractive component. Then, total interaction energy is the combination of the short-range and long-range interactions:

$$U = U_{SR} + U_{LR} \tag{47}$$

The general interaction between all the ions in a solid can be very complex and can be written as a series of summations involving increasing numbers of ions, i.e. two-body, three-body and *n*-body terms:

$$U = U_0 + \sum_{ij} U_{ij} + \sum_{ijk} U_{ijk} + \sum_{ijkl} U_{ijkl} + \cdots \tag{48}$$

where *ij* represents interactions between pairs of ions, *ijk* triplets, and higher order terms. U_0 is the function of the local environment and defines the zero energy. It should be stressed, as argued previously, that employing such a potential model does not necessarily mean that the electron distribution corresponds to a fully ionic system, and that the general validity of the model is assessed primarily by its ability to reproduce observed properties of the crystal lattice. Indeed, good quality interatomic potentials are available for a wide range of oxides materials.

2.4.1 Long-Range Interaction

In this study, the interaction pair is simplified to a set of pair-wise interactions, from which the long range and short range interactions can be defined. In an ionic system if a pair of ions i and j are separated by a distance r_{ij}, there is a Coulomb interaction energy found by solving equation (49):

$$\Phi_{ij} r_{ij} = \frac{q_i q_j}{4\pi\epsilon_0 \mathrm{r_{ij}}} \tag{49}$$

where q is the charge on the ion and ϵ_0 is the permittivity of free space. In non-ionic systems this interaction will not be present and only short range interactions need to be considered.

2.4.2 Short-Range Interaction

Short-range interactions involve the attractions and repulsions of the ions. Electron cloud overlap leads to strong short-range repulsive forces since electron density and therefore nuclear shielding, is reduced. This in turn increases the Columbic repulsion between the positively charged nuclei. The charge distributions of two adjacent atoms are able to overlap if they are brought near enough to one another. This causes two repulsive interactions, which if the distance between these atoms become sufficiently small causes the overall force between them to become repulsive, even if the ions are oppositely charged. Formal charges are assumed for lattice simulations and gas surface interactions are non-ionic, thus; the short-range potential is the only simulation variable throughout. As such, great care over the form and parameters of the short-range interactions must be exercised. Despite this, by only adjusting the much smaller short-range, contribution the whole spectrum of crystal structures can be reproduced. In the next subsections, selected possible descriptions for the short-range interaction are discussed.

2.4.2.1 Simple Harmonic Interaction

The most basic form would be a simple harmonic interaction given by equation (50) below:

$$\Phi_{sr}(r_{ij}) = \frac{1}{2}k(r_{ij} - r_0)^2 \quad (50)$$

where r_{ij} is the distance between two atoms i and j, r_0 is the equilibrium bond distance and k is the harmonic force constant. This model is quite sufficient for systems that only deviate slightly from r_0 and for which interactions can realistically be confined to adjacent pairs of ions.

2.4.2.2 Buckingham Potential

The Buckinghum potential rests upon the specification of an effective potential model, which expresses the total energy of the system as a function of the nuclear coordinates. For polar solids, a good basis is the Born model framework, which partitions the total energy into long-range Coulombic interactions, and a short-range term to model the repulsions and van der Waals forces between electron charge clouds. The Buckingham potential is often used for the short-range term to describe wider ranges of separations. The analytical expression of Buckingham potentials is given by equation (51) as follows;

$$\Phi_{ij}(r_{ij}) = A_{ij}e^{\left(\frac{-r_{ij}}{\rho_{ij}}\right)} - \frac{C_{ij}}{r_{ij}^6} \quad (51)$$

where A_{ij} and r_{ij} describe components of the repulsive interaction and C_{ij} describes the attractive interaction. A_{ij} and r_{ij} are thought to relate to the number of electrons and the electron density, respectively, while C_{ij} is meant to represent the van der Waals interactions. The classification of the short-range interaction used here is somewhat generalised since the van der Waals interaction will operate over several atomic distances, A and ρ are related to the size and the hardness of the ion, respectively.

2.4.3 Periodic Boundary Conditions

Because of the small number of particles used in simulations, it is important that particles do not evaporate i.e., get so far away from the centre of mass of the system such that they no longer interact with the other particles. Evaporation removes energy from the system. To prevent evaporation, the particles are confined to a box. When a

particle crosses a side of the box, it is teleported to the opposite side of the box, with its velocity unchanged. This is a form of periodic boundary conditions. The basic box is considered to be replicated throughout the space. Each particle has an image in each replicated box. For short-range forces, like the Buckingham force, we only need to consider interactions with particles that are near.

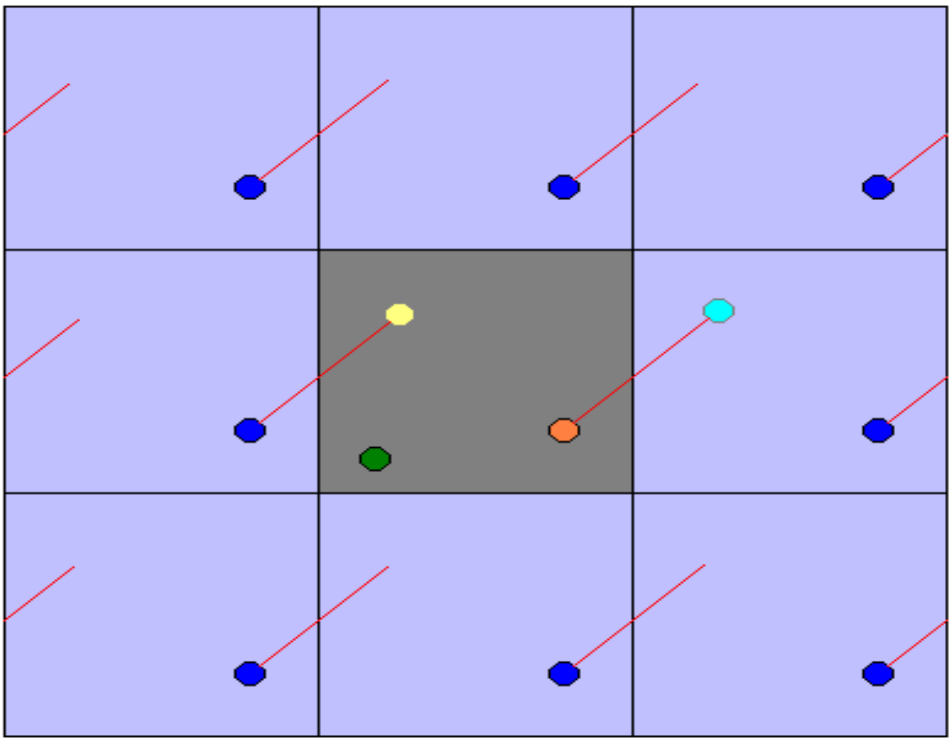

Figure 6: The illustration of periodic boundary conditions. The blue particles are all images of the orange particle in the basic box. The dashed lines show the motion of the particle and its images over a time step. The light blue and yellow filled circles show where the orange particle and one of its images are at the end of the time step.

2.5 Energy Minimisation

Energy minimisation generates individual minimum energy configurations of the system. Thus, energy minimisation is a numerical procedure for finding a minimum on the potential energy surface starting from a higher energy initial structure. In some cases the information provided by energy minimisation can be sufficient to predict accurately the properties of the system. If all minimum configurations on the energy surface can be identified then statistical mechanical formulae can be used to derive a partition function from which thermodynamic properties can be calculated. However,

this is possible only for relatively small molecules or small molecular assemblies in the gas phase. When the structures are built in a computational chemistry software package Media, the initial geometry does not necessarily correspond to one of the stable conformers. Therefore, energy minimisation is usually carried out to determine a stable conformer. This process is also called geometry optimisation. In this study, energy minimisation was performed with the static energy minimisation technique using CASTEP [75] and METADISE [76] codes.

2.6 Computer Codes

Computer simulation of matter with atomistic detail has become a very prominent tool in chemistry, physics, life sciences and materials sciences. In these fields, simulation results can yield the insights needed to interpret experimental measurements, can be used to predict material properties and design new materials.

2.6.1 GULP

The General Utility Lattice Program (GULP), is a classical simulations code for performing a wide range of calculations on 3D periodic solids, 2D surfaces, gas phase clusters and isolated defects in bulk materials [77] . In particular, GULP has a large number of materials-specific force fields, such as the shell model for simulating ionic materials. Recently, GULP has been implemented in such a way that it is operated from within the Materials Studio® environment.

2.6.2 METADISE

METADISE is a computer code that is designed to model surfaces and interfaces as well as dislocations in a system. The crystal is considered to consist of a series of (charged) planes parallel to the surface and periodic in two dimensions. METADISE uses a two-region approach, considering the crystal as being comprised of two blocks, each consisting of two regions, I and II, which are periodic in two dimensions. Those atoms near the interface are incorporated into region I while region II represents the rest of the crystal. The inclusion of region II ensures that all the ions in region I experience the forces associated with the rest of the crystal and that the energies are fully converged. Region I ions are allowed to relax to their mechanical equilibrium, whereas region II ions are kept fixed. To achieve energy convergence, the number of ions in region I and II have to be sufficiently large. In this work, METADISE code was

used to optimise starting models for MnO_2 and $LiMn_2O_4$ systems and generate DL_POLY input files.

2.6.3 DL_POLY

DL_POLY [78] is a package of subroutines, programs and data files, designed to facilitate molecular dynamics simulations of macromolecules, polymers, ionic systems, solutions and other molecular systems on a distributed memory parallel computer**.** The code imposes 3D periodic boundary conditions. DL_POLY is a general-purpose parallel molecular dynamics simulation package developed at Daresbury Laboratory under the auspices of the Council for the Central Laboratory of the Research Councils. Written to support academic research, it has a wide range of applications and is designed to run on a wide range of computers: from single processor workstations to parallel supercomputers. Its structure, functionality, performance, and availability can be found elsewhere. In this study, all molecular dynamic simulation results were performed using DL_POLY code.

2.6.4 MedeA

The MedeA® software package predicts materials properties using simulations based on quantum mechanics, statistical thermodynamics, classical mechanics and electrodynamics as well as correlation methods involving empirical data. MedeA® is designed for materials engineers and scientists who want rapid and reliable answers for a range of materials issues related to application areas such as electrical power generation, automotive applications, energy storage, alloy design, microelectronics, the chemical industry and petrochemicals. MedeA® environment was used to create various MnO_2 and spinel $LiMn_2O_4$ nanotubes.

2.6.5 Materials Studio

Accelrys Materials Studio is a software package that is designed for structural and computational researchers in physics, chemistry and materials science research and development and it covers the following areas of application:

Materials Studio's analytical and crystallisation software helps investigate, predict and modify crystal structure and crystal growth. It can be used to simulate particle

morphology, predict crystal structure and understand polymorphism, study surface interactions and design growth mediating additives. Also it can be used to calculate various properties such as, electronic, structural, thermodynamics and mechanical properties.

2.7 Generation of Nanotubes

Generation of nanotube is way of arranging the atomic structure of a substance so that it can be made thousands of times stronger than in its native state. The ability to build nanostructures of defined shapes, physical, chemical and mechanical properties has always been a prerequisite for the development of nanotechnology. The main challenge in this area is how to precisely control the sizes, dimensionalities, compositions and crystal structures at the nanoscale level, which may serve as a powerful tool for the tailoring of physical/chemical properties of materials in a controllable way. Synthesis of nanostructures with a single-size and morphology is one of the most significant challenges in nanotechnology [79]. The difficulty arises because nanostructures are normally metastable relative to the equivalent bulk material [80]. However, the growth of nanostructure is driving the development of new electroactive materials for batteries and other applications. Figure 7, shows how experimentally carbon nanotubes (and other materials) are constructed. In simple form, carbon nanotubes are formed by rolling-up an infinite strip of graphite sheet, called graphene layer as illustrated in figure 7.

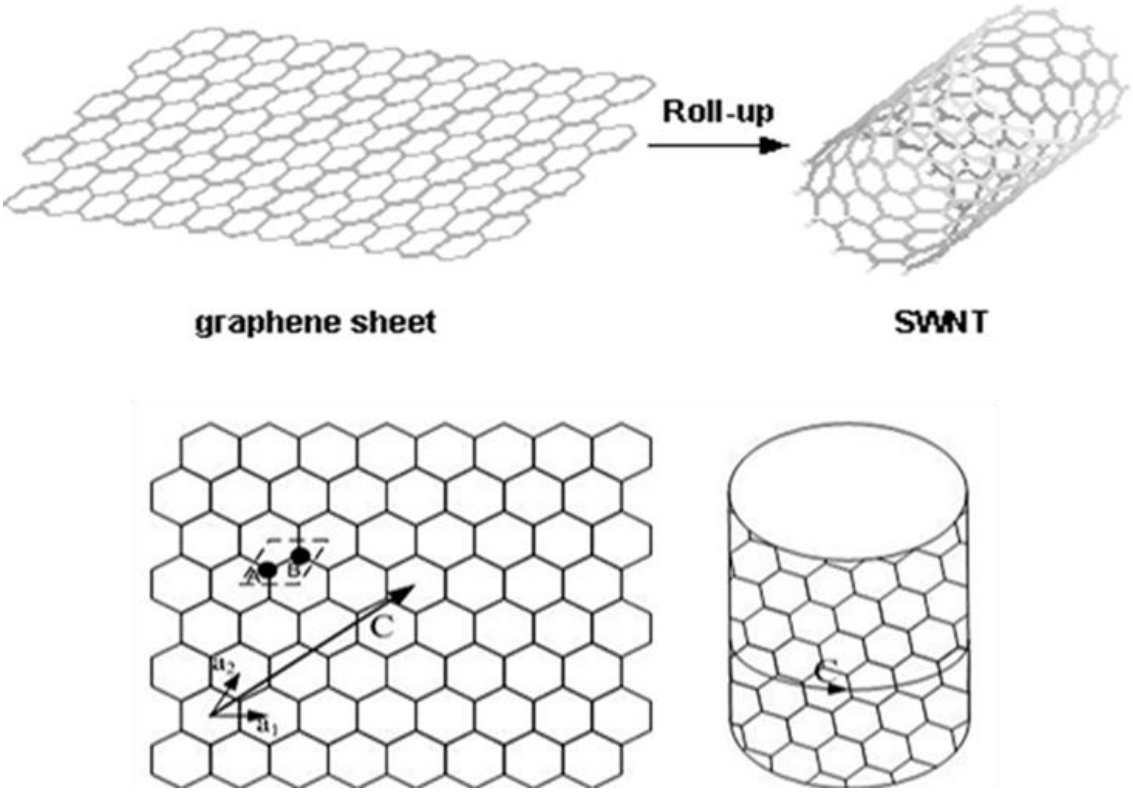

Figure 7: Illustration of generating single wall carbon nanotubes experimentally [81].

Nanotubes structures are usually synthesised by a hydrothermal reactions [82]. They typically have diameter of approximately 5-10nm [83], a length of between ~100nm and ~10μm and consist of between approximately 3-5 layers [84]. On the nanometer scale, self-assembly has proven to be a viable method for building structures with reliability and precision. The structure of the nanotubes is difficult to clearly understand from the experimental studies. Currently, the crystal structure of nanotubes remains unclear and this is hampering efforts to explain the formation mechanism of the nanotubes [85]. Various methods have been demonstrated to process a broad range of materials into nanotubes. However, the methods are complicated, time-consuming and hard to control. Thus, the shape control and size tenability of these tubular nanostructures remain difficult. The surface of the structure and morphologies of nanostructure are difficult to extract by experiment. With the right arrangement of atoms therefore computer simulations, on the other hand, offer a valuable means of exploring such structures. Computer simulation strategies have attracted more attention because they can simply be developed to control the shapes of various materials. Furthermore, the nanotube materials can be processed and simulated at a larger scale. In this study, MnO_2 and $LiMn_2O_4$ cathode materials are developed using computer simulation strategies. Variables such as diameter, Miller

index, symmetry and size are varied to construct various nanotube structural models. Details of the techniques followed in the study are presented below.

Materials design software (Medea®) was used to generate MnO_2 and $LiMn_2O_4$ nanotube structures. From the bulk structure, low Miller index surfaces ({001}, {100} {110} and {111}) with various orientations were created. In figure 8, surfaces cut from {100} and {110} Miller indices are shown as examples. From the cleaved surfaces, next step is to select and freeze atoms which will not form part of the slab for building a nanotube. Thus, freezing these atoms (thin balls and sticks in the diagram) simply contribute in controlling which atoms will be used to generate the nanotube. All the frozen atoms will not be part of the slab which will be wrapped to form a nanotube. Atoms placed at any position in the surface can be used to construct the slab as long as they make the right stoichiometry of the system under investigation. Also any number of layers can be used as long as they form the correct stoichiometry of the system. The number of layers used determines and contributes to the number of walls that the nanotube will be made up of. When creating the slab, the frozen atoms are eliminated from forming part of the slab as shown in figure 8. Then the selected atoms which form the slab are wrapped around to form a nanotube. Figure 8 depicts how a nanotube with a 15Å diameter was created from the slab. From the same slab nanotubes with different diameter and different wrapping directions can be generated.

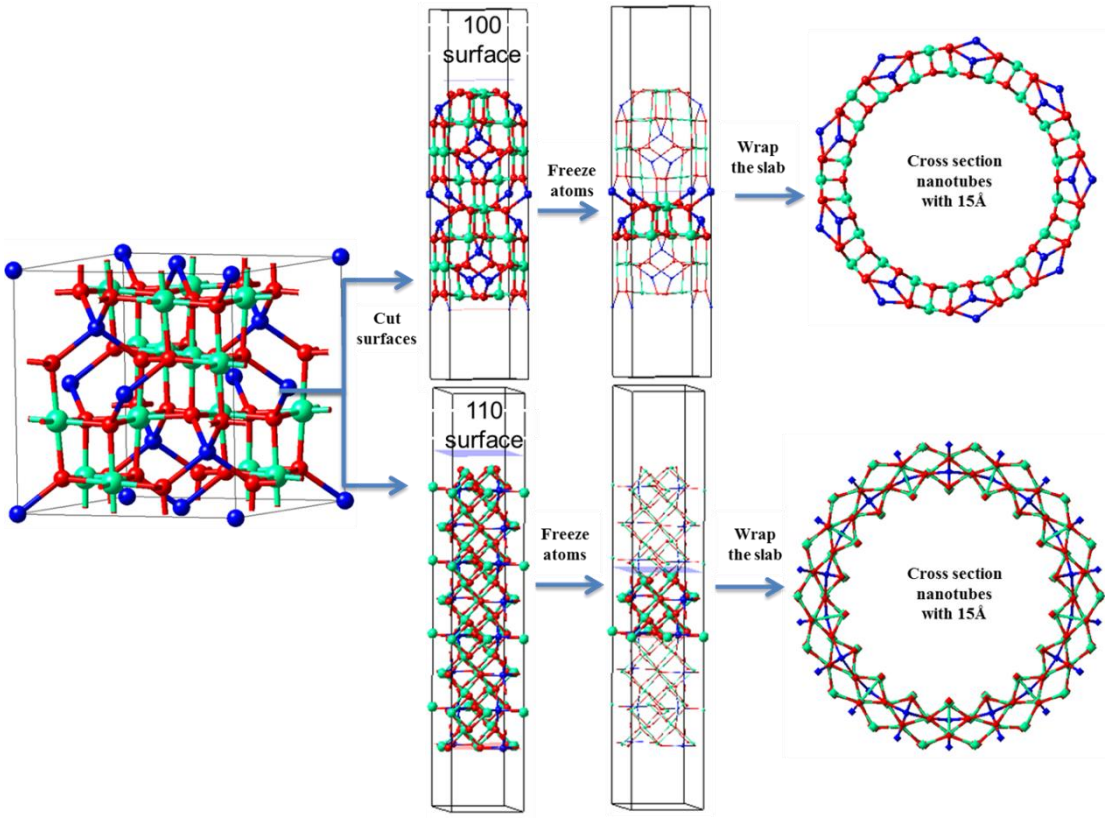

Figure 8: Step-by-step procedure for constructing $LiMn_2O_4$ nanotubes from different surfaces.

Figures 9 and 10, illustrate how nanotubes can be wrapped in two different directions, which produce nanotubes with different atomic geometrical arrangement. Thus, when a slab cut from the same position on a surface is wrapped along two different directions, different nanotubes structures are generated. Figure 9 shows the resulting MnO_2 nanotube when the slab is wrapped along a_around_b direction. The top layer of the slab resides on the inner surface of the nanotube while the bottom layer of the slab forms the outer part of the nanotube. Figure 10 depicts MnO_2 nanotube structure formed when the slab is wrapped along b_around_a direction. In this case, the bottom layer is on the inner side of the nanotube while the top layer is on the outer side of the nanotube. The resulting nanotube structures indicate that the atomic geometric arrangements of the nanotubes depend on the direction of rolling-up the surface and this can be controlled using computer simulations techniques.

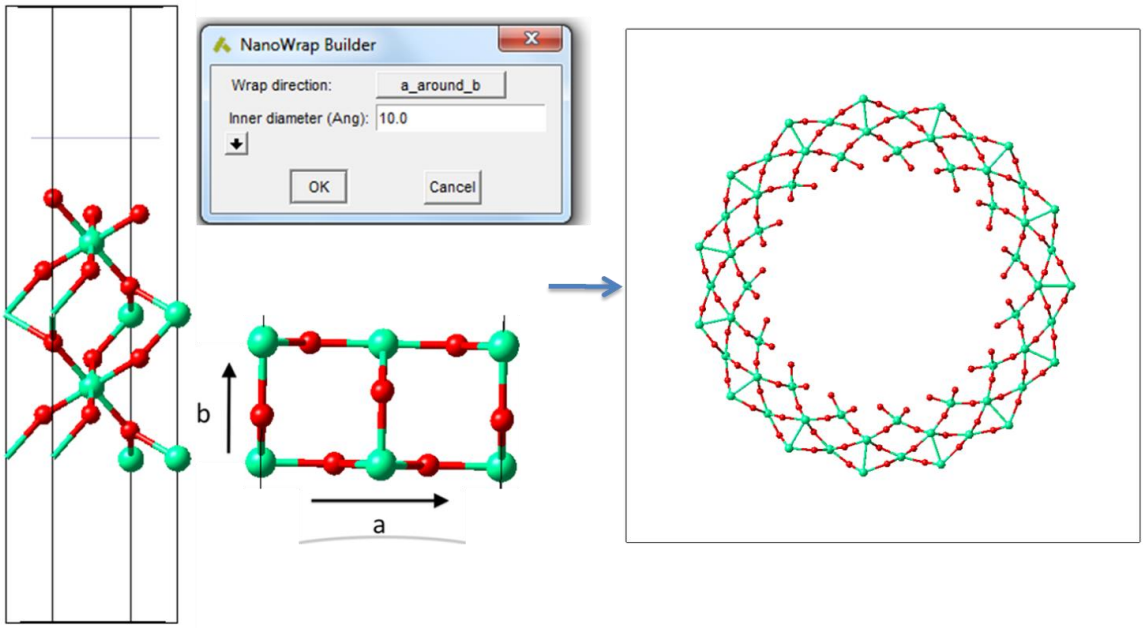

Figure 9: MnO_2 10Å nanotube depicting the structure resulted from wrapping along a_around_b direction.

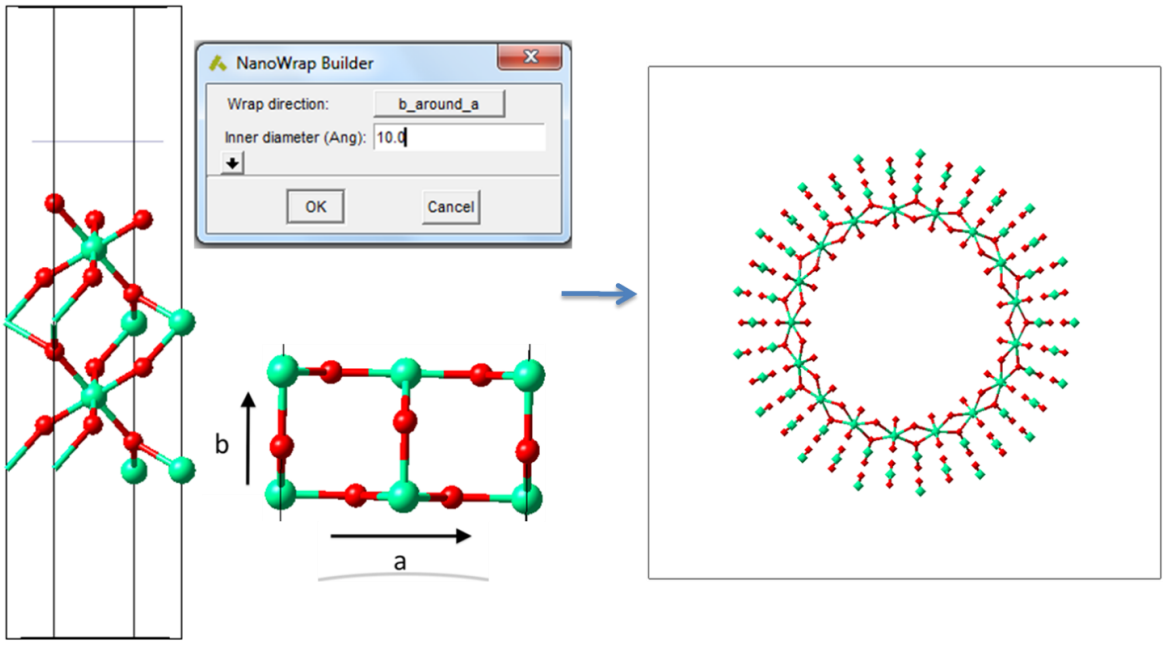

Figure 10: MnO_2 10Å nanotube depicting the structure resulted from wrapping along b_around_a direction.

Chapter 3

MnO_2 Nanotubes Results and Discussion

3.1 Atomistic Simulations of MnO_2 Nanotubes

Atomistic simulation of materials with atomistic details has become a very prominent tool in chemistry, physics and materials science. In these fields, a simulation uses the various potential models and can yield the insights needed to interpret experimental measurements. Also, it can be used to predict material properties or design new materials for various applications. In classical atomistic simulations, the energy of the crystal is described via interatomic potentials. The potential is comprised of parameterised analytical expressions describing the interaction between atoms. In this study potential models based on Born model of ionic solids was considered. A partially charged model, where the rigid ion potentials were obtained by modifying the parameters for model developed by Matsui [86] for isostructural TiO_2 was used. The potential parameter reproduced structural parameters for MnO_2 well and the parameters have been published elsewhere [87] proved to be reliable for simulating MnO_2 nanostructures. Matsui has successfully applied this potential to study the stability of TiO_2 polymorphs as the function of temperature and pressure.

Table 1: Interatomic potentials for pyrolusite MnO_2 rigid ion model. The potential parameters describe the short-range potential term between the compound ions species. The cut-off of 10.0Å was used.

Interaction	A(eV)	P(Å)	C(eVÅ^6)	species	q(e)
$Mn^{2.2+}$-$O^{1.1-}$	15538.20	0.195	22.00	$Mn^{2.2+}$	2.20
$Mn^{2.2+}$-$Mn^{2.2+}$	23530.50	0.156	16.00		
$O^{1.1-}$-$O^{1.1-}$	11782.76	0.234	30.22	$O^{1.1-}$	-1.10

3.2 Geometry Optimisation of MnO_2 Nanotubes

Geometry optimisation is a procedure that attempts to find the configuration of minimum energy of the system. It is the geometry that minimises the strain on a given

system. Any perturbation from this geometry will induce the system to change so as to reduce this perturbation.

MnO_2 nanotubes were generated from low Miller indices i.e. {001}, {010}, {100} and as {110} shown in table 2, starting with the diameter of 5Å. Previous studies demonstrated that nanotubes with smaller diameter are stable. The structures were fully optimised using energy minimisation technique embedded within CASTEP code, with a cut-off of 600 eV and k-point set 2x1x1. Therefore it was possible to calculate the total energy of the nanotubes. Nanotube made with {100} surface was found to have the lowest energy as shown in table 2 and this surface was also found to be the most stable surface in TiO_2 nanotube [88]. The nanotubes contracts after geometry optimisation.

Table 2: Total energy for MnO_2 nanotubes with 5Å diameter.

Miller Index	Energy (eV)	Cell Volume (A^3)	
		Before Optimisation	After Optimisation
{001}	-12201.62	2381.45	1223.80
{010}	-18302.69	2794.73	1760.51
{100}	-24386.19	3938.80	1772.84
{110}	-18289.63	3724.66	2164.59

3.3 MnO_2 nanotubes with Diameter Ranging from 5Å-11Å

3.3.1 MnO_2 {100} Nanotube

Diameter represents an important structural parameter of nanotubes. However, precise control of nanotube diameter over a wide range of materials is yet to be demonstrated. In this section different MnO_2 nanotubes with smaller diameter 5Å-11Å are generated and discussed. Figure 11 shows MnO_2 nanotube generated from {100} surface with diameter ranging from 5Å-11Å. As discussed in chapter 2, nanotubes can be wrapped in two different ways. In this case, the presented nanotubes are wrapped along b_around_a direction. Nanotubes generated from {100} surface is composed of a varying number of atoms relative to the size of the diameter. Thus, nanotubes with diameter 5Å has 72 atoms while 7Å, 9Å and 11Å are composed of 96, 120 and 156 atoms, respectively. For all the nanotubes, the inner layer is composed of interstitial O

atoms, while the outer layer is composed of Mn and O atoms. All the nanotubes reveals that Mn atoms are octahedrally coordinated.

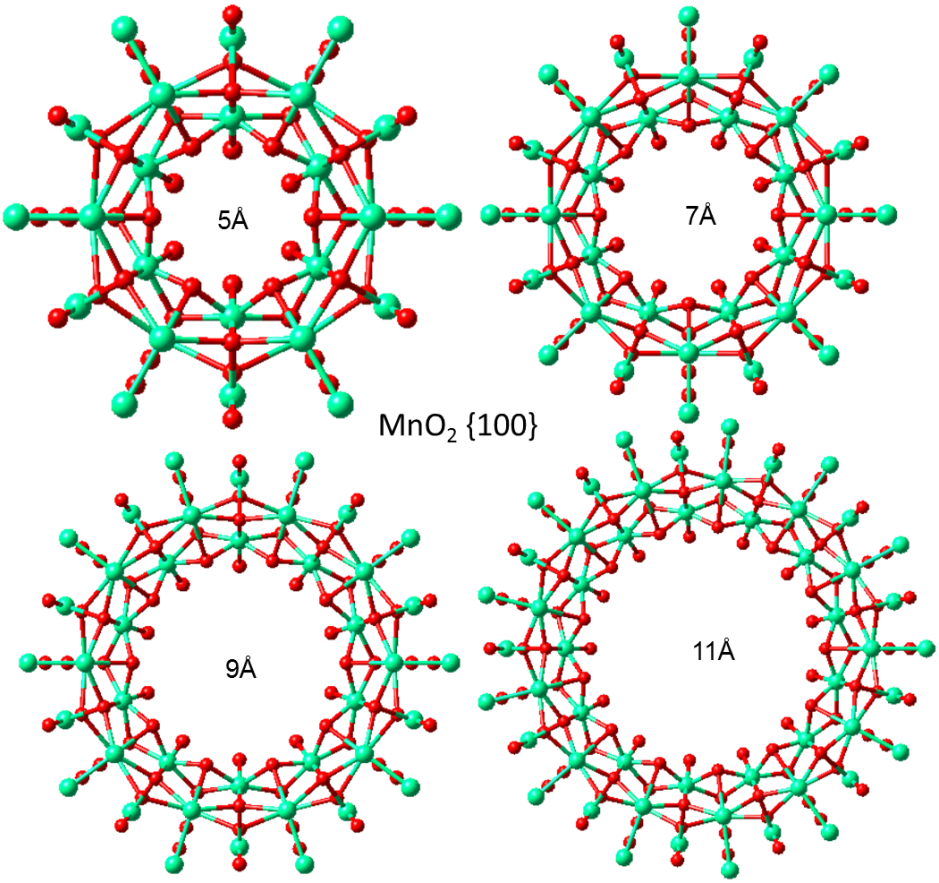

Figure 11: MnO_2 nanotube obtained by rolling up {100} surface with diameter from 5Å-11Å.

3.3.2 MnO_2 {110} Nanotube

In this section, we demonstrate that different nanotube structures can be generated from same surface when the slab is cut at different positions from the surface. Figure 12 shows MnO_2 {110} surface cut from the bulk system, together with the slab and the nanotube structure. In this case, the slab was cut at the middle of the surface and wrapped along a_around_b direction to generate nanotube shown in figure 13. From the slab it is evident that the system has a stoichiometry of 1Mn:2O and also observed octahedral coordination on Mn atoms. Similarly to {100} nanotube discussed in section 3.3.1, the nanotube are composed of 72, 96, 120 and 156 atoms for 5Å, 7Å and 9Å and 11Å respectively. As the diameter is increased the shape of the nanotube becomes more circular. For all the nanotubes, the inner layer is composed of Mn atoms while the outer layer is composed of Mn and O atoms.

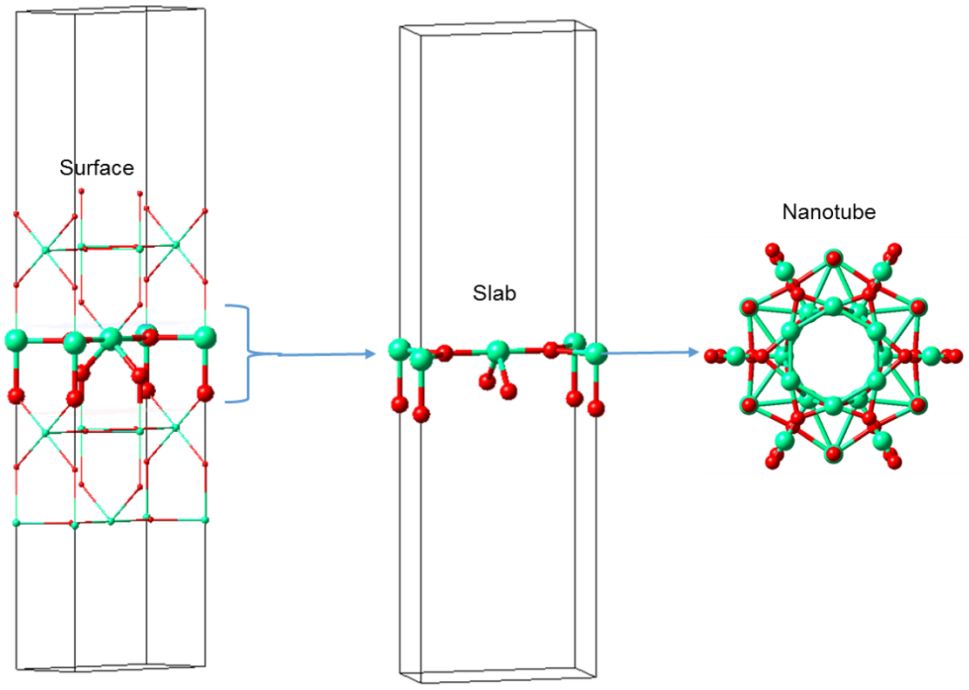

Figure 12: MnO_2 slab of {110} surface.

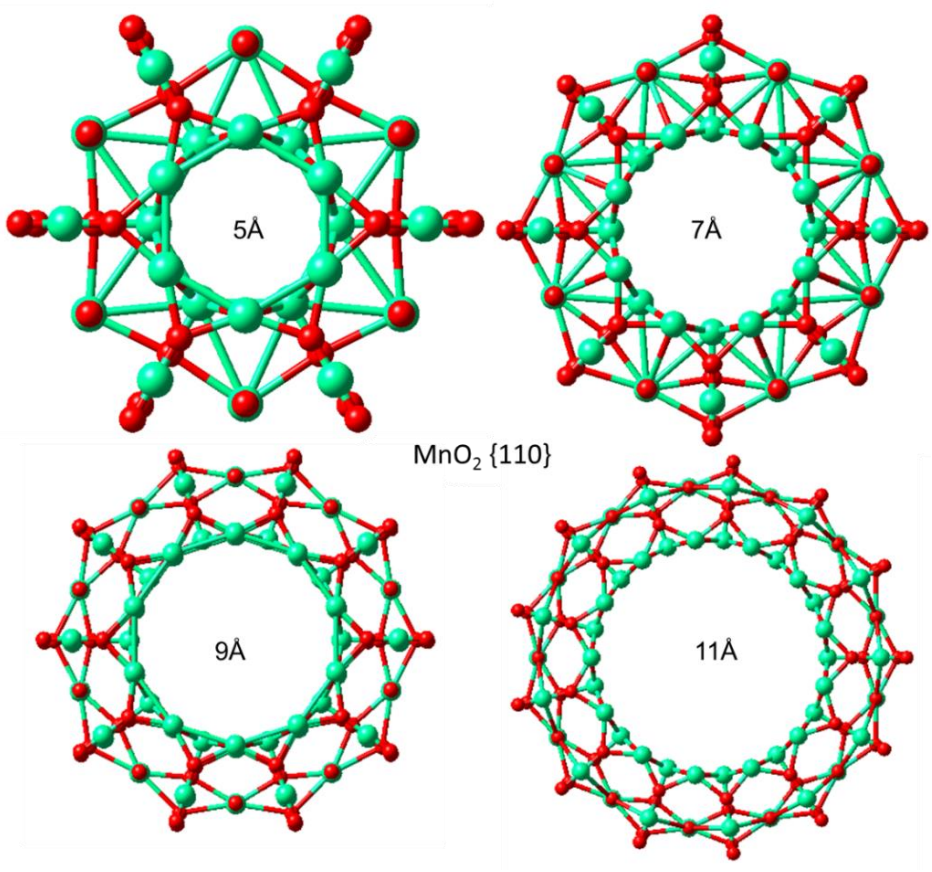

Figure 13: MnO_2 nanotubes generated from {110} surface.

Figure 14 shows MnO_2 {110} surface cut from the bulk system, together with the slab and the nanotube structure, whereby nanotubes in figure 15 are generated and were wrapped along a_around_b direction. Nanotube generated from {110} surface is composed of a varying number of atoms relative to the size of the diameter. Thus, nanotubes with diameter 5Å has 72 atoms while 7Å, 9Å and 11Å are composed of 96, 120 and 156 atoms respectively. For all the nanotube structures, the inner and outer layers are composed of alternating Mn and O atoms.

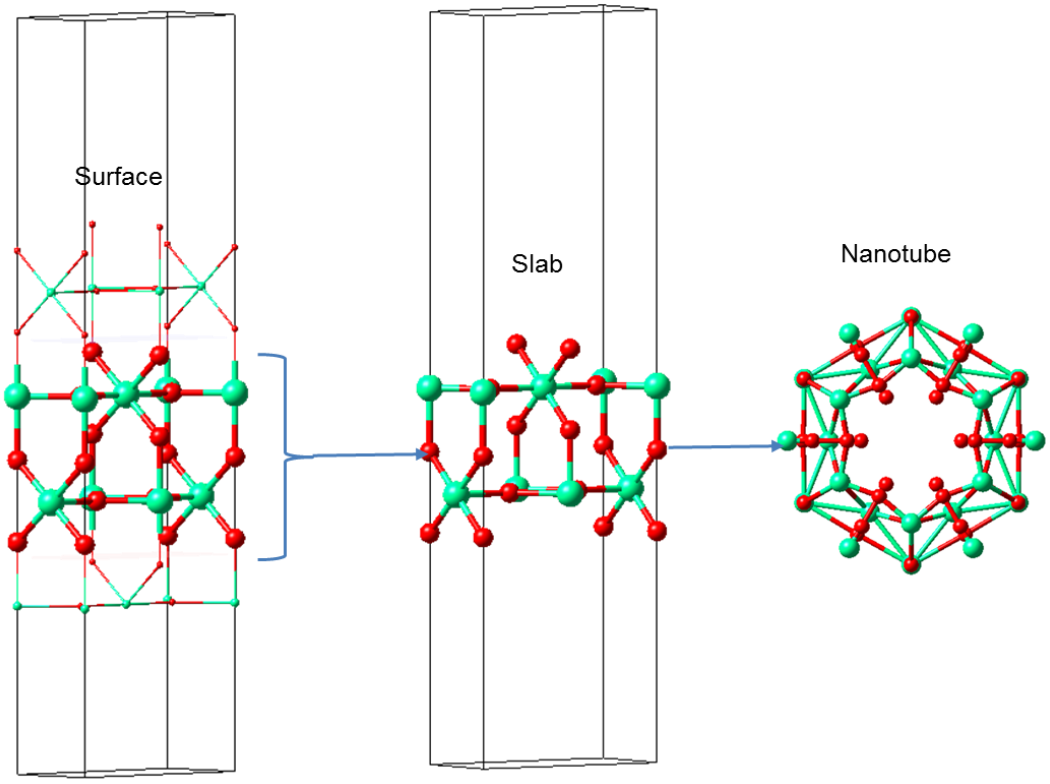

Figure 14: MnO_2 slab of {110} surface.

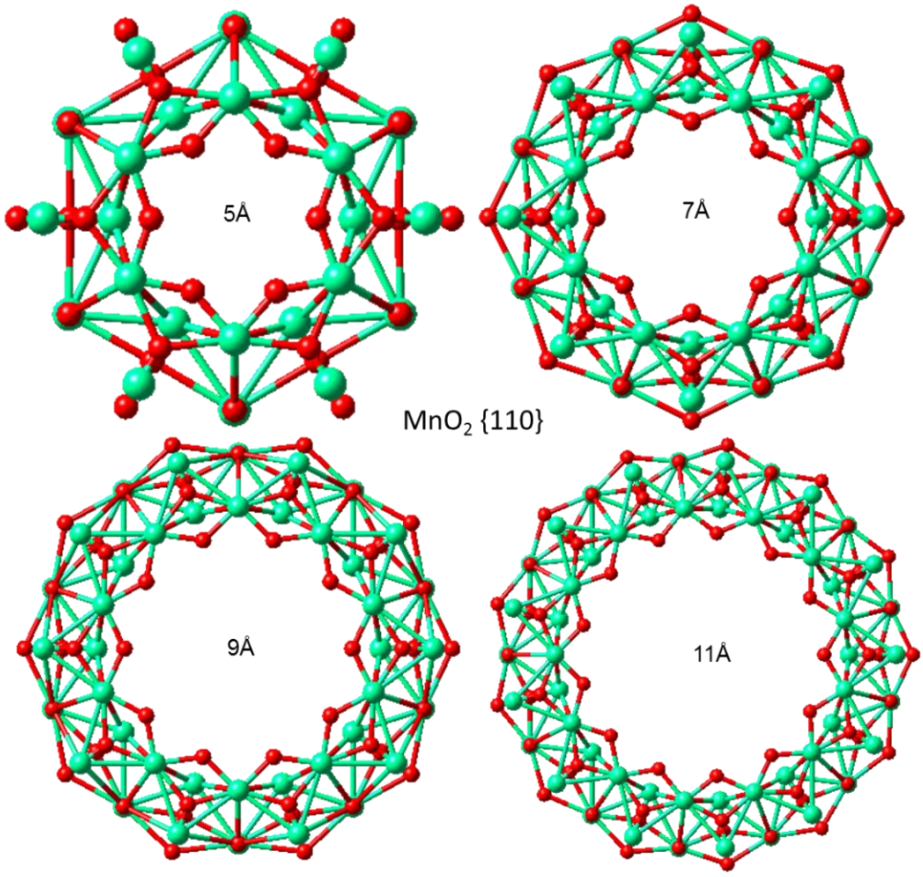

Figure 15: MnO_2 nanotubes generated from {110} surface wrapped along a_around_b.

Figure 16 shows {110} nanotubes wrapped b_around_a direction as discussed in section 2.7. As compared to the nanotubes wrapped a_around_b in figure 16, b_around_a is not closely-packed. This may suggest that for {110} nanotubes wrapping along a_around_b is more favourable than along b_around_a direction. For all the nanotubes the inner and the outer layer composed Mn and O atoms. There is no clearly defined coordination for all the nanotubes. Nanotube generated from {110} surface is composed of a varying number of atoms relative to the size of the diameter. Thus, nanotubes with diameter 5Å has 72 atoms while 7Å, 9Å and 11Å are composed of 96, 120 and 156 atoms, respectively. Using the standard vector notation (n,m) used for this nanotubes, these denote (3,3), (4,4), (5,5) and (6,6) for 5Å, 7Å, 9Å and 11Å nanotubes, respectively.

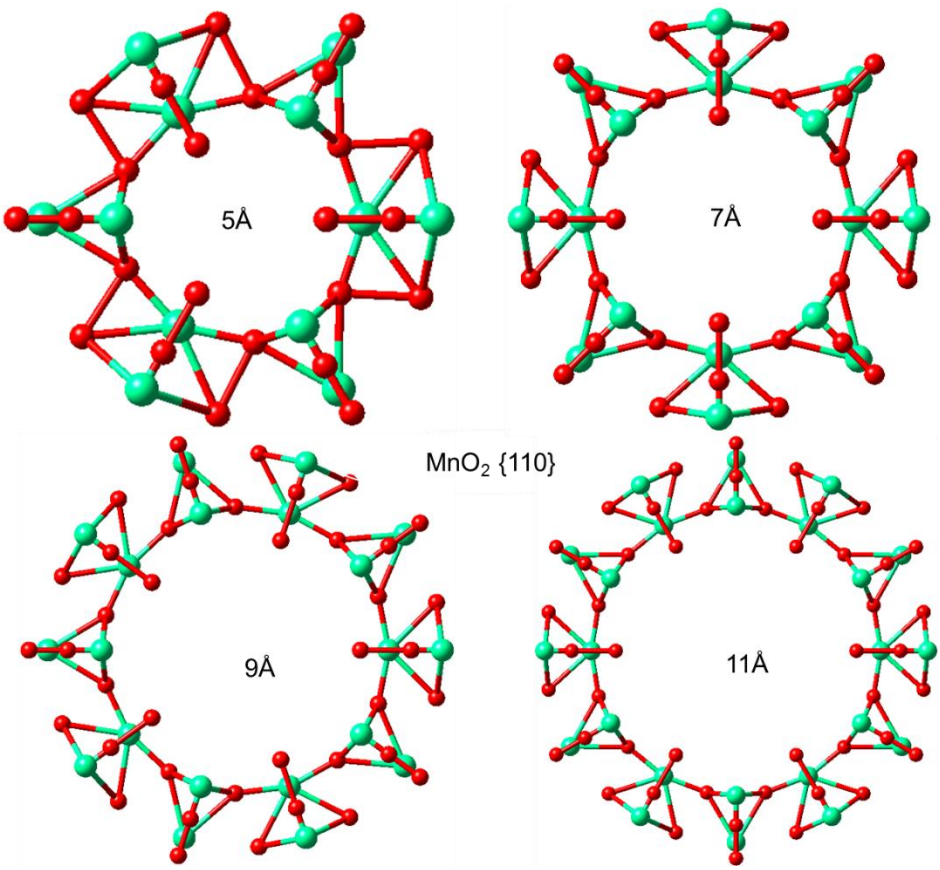

Figure 16: MnO_2 nanotube generated from {110} surface wrapped along b_around_a.

3.3.3 MnO_2 {001} Nanotube

Figure 17 shows MnO_2 nanotube generated from {001} surface with diameter ranging from 5Å-11Å. The nanotubes are wrapped along a_around_b direction. The shape of the tube changes as the diameter is increased. Similarly, nanotubes generated from {001} surface are composed of a varying number of atoms relative to the size of the diameter. Thus, nanotubes with diameter 5Å has 72 atoms while 7Å, 9Å and 11Å are composed of 96, 120 and 156 atoms, respectively. As the diameter is increased, the more the circular nanotubes becomes. For all the nanotubes, the inner and the outer layers are composed of Mn and O atoms. Compared to {100} and {110} nanotubes discussed in the previous sections, this nanotube is not closely-packed. It is known generally that for bulk systems, the more closely-packed is the system, the more stable it is. Similar observation is noted from the generated nanotube structures, the less closely-packed is the system and the less stable it is. This is confirmed by geometry optimisation results, where {001} nanotube is the least stable.

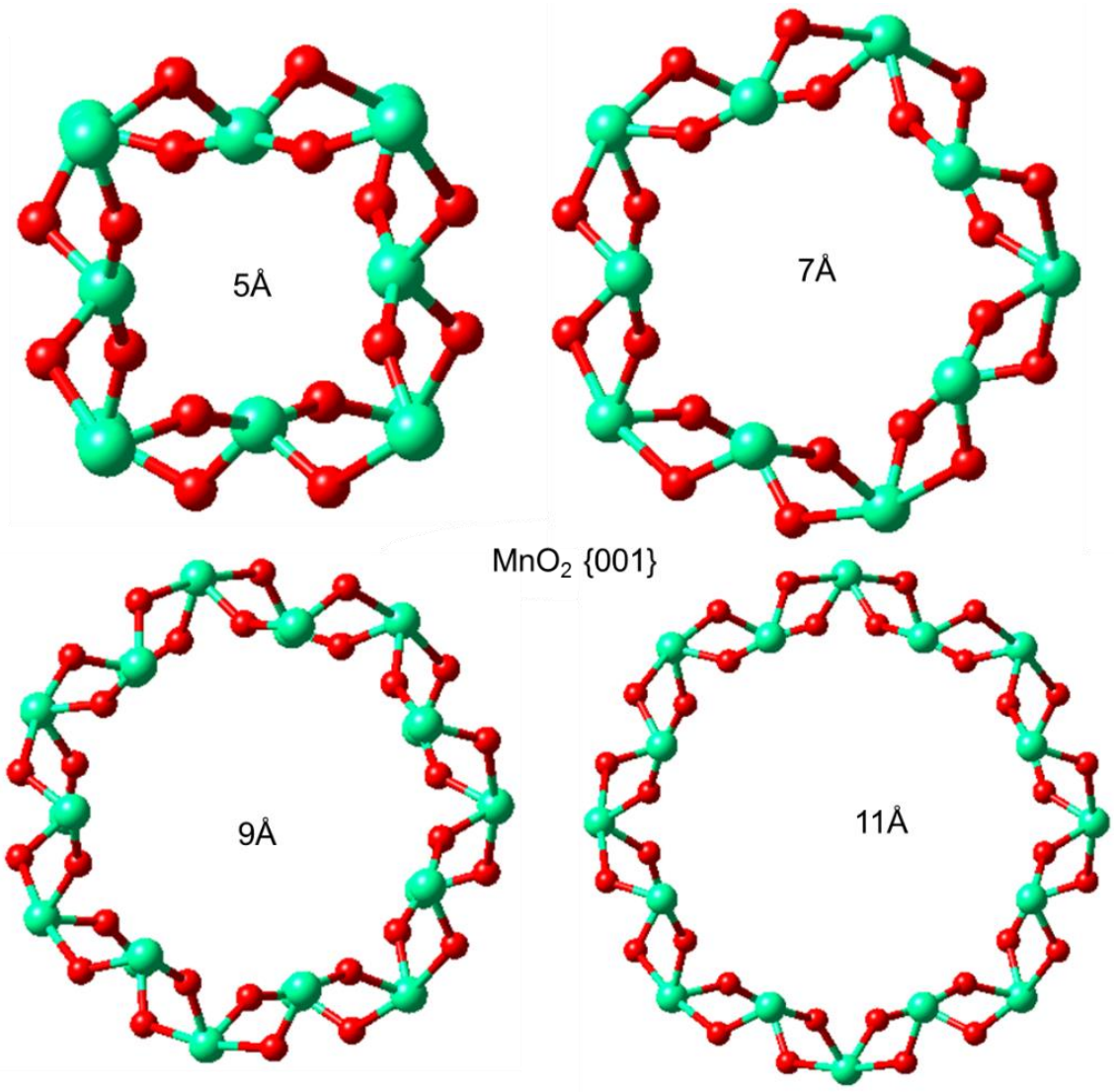

Figure 17: MnO_2 nanotubes created from {001} surface.

3.3.4 MnO_2 {111} Nanotube

Figure 18 shows a MnO_2 nanotube generated from {111} surface with diameter ranging from 5Å-11Å. The nanotubes are wrapped along a_around_b direction. Nanotube generated from {111} surface is composed of a varying number of atoms relative to the size of the diameter. Thus, nanotubes with diameter 5Å has 72 atoms while 7Å, 9Å and 11Å are composed of 96, 120 and 156 atoms, respectively. As the diameter of the nanotube is increased, the nanotube becomes more circular. For all the nanotubes, the inner and the outer layers are composed of Mn and O atoms (MnO_2).

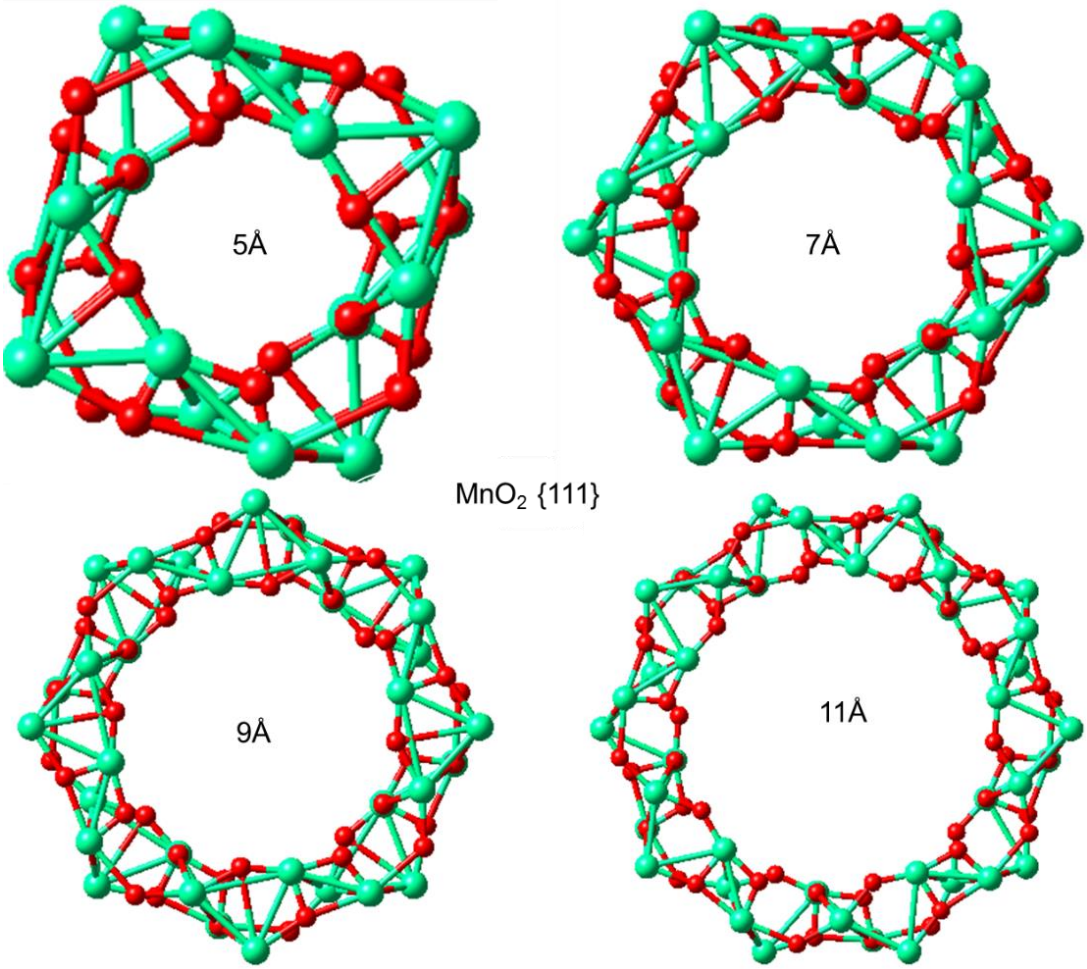

Figure 18: Multi-wall MnO_2 nanotube obtained by rolling up {111} surface with diameter from 5Å-11Å.

3.4 MnO_2 Nanotube with Diameter Ranging From 10Å-30Å

3.4.1 MnO_2 {100} Nanotube

In this section different MnO_2 nanotubes with larger diameter (15Å-30Å) are generated and discussed. Figure 19, shows MnO_2 nanotube generated from {100} surface with diameter ranging from 15Å-30Å. Nanotube generated from {100} surface is composed of a varying number of atoms corresponding to the size of the diameter. Thus, nanotubes with diameter 15Å has 204 atoms while 20Å, 25Å and 30Å are composed of 264, 336 and 396 atoms, respectively. The nanotubes are wrapped along b_around_a. For all the nanotubes, the inner layer is composed of interstitial O atoms, while the outer layer is composed of Mn and O atoms. All the nanotubes reveals that Mn atoms are octahedrally coordinated.

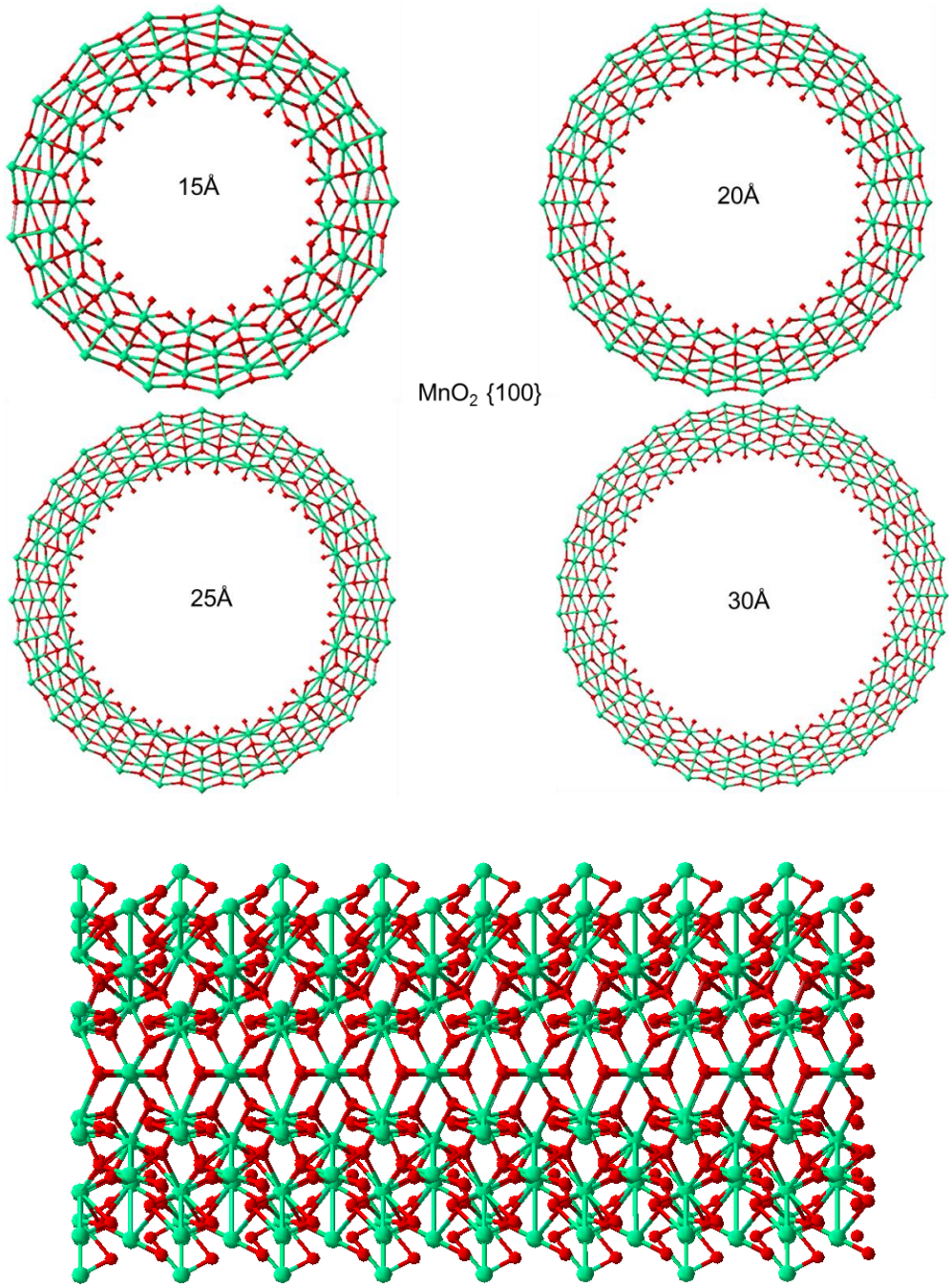

Figure 19: Cross-sectional view and long view of MnO_2 nanotube along {100} surface with diameter ranging from 15Å-30Å.

3.4.2 MnO_2 {110} Nanotube

The results presented herein, represent the widest range of average diameter control with the highest precision for MnO_2 nanotubes. This level of diameter control in terms of range and precision rivals the highest report levels and highlights simulations ability to control the structures of the nanotubes. Figure 20 shows a MnO_2 nanotube

generated from {110} surface with diameter ranging from 15Å-30Å. Nanotube generated from {110} surface is composed of a different number of atoms relative to the size of the diameter. Thus, nanotubes with diameter 15Å has 204 atoms while 20Å, 25Å and 30Å are composed of 264, 336 and 396 atoms, respectively. The nanotubes are wrapped along a_around_b. For all the nanotubes, the inner layer is composed mostly of Mn atoms, while the outer layer is composed of Mn and O atoms. The cross-section area of nanotube decrease as the diameter is increased.

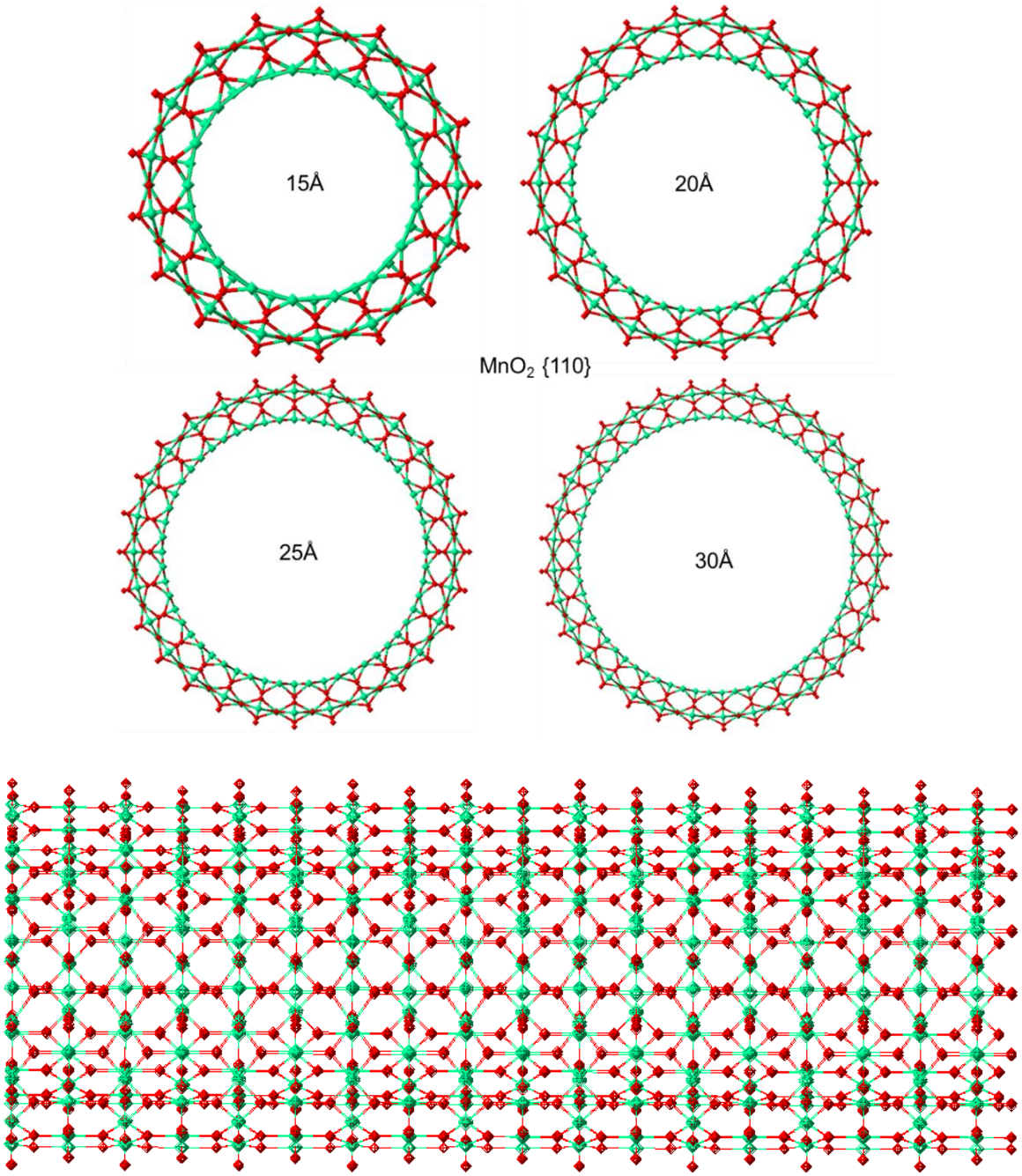

Figure 20: Cross-sectional view and long view of MnO_2 nanotube along {110} surface ranging from 15Å-30Å.

3.4.3 MnO_2 {001} Nanotube

Figure 21 shows a MnO_2 nanotube generated from {001} surface with diameter ranging from 15Å-30Å. The nanotube structures are wrapped along a_around_b direction. Nanotube generated from {100} surface is composed of different number of atoms corresponding to the size of the diameter. Therefore, nanotubes with diameter 15Å has 204 atoms while 20Å, 25Å and 30Å are composed of 264, 336 and 396 atoms, respectively. For all the nanotubes, the inner layer is composed mostly of Mn and O atoms, while the outer layer is composed of Mn and O atoms.

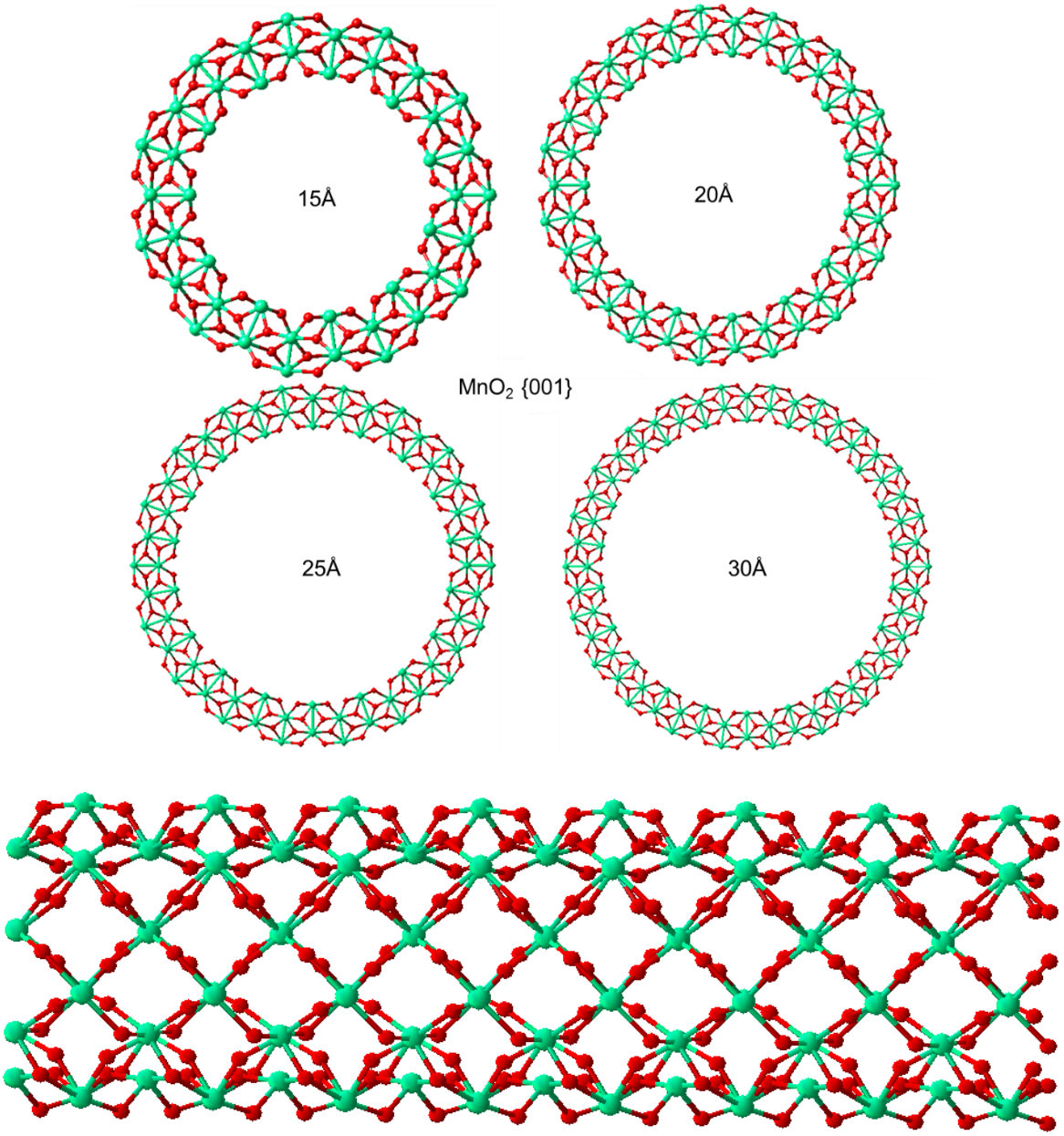

Figure 21: Cross-sectional view and long view of MnO_2 nanotube along {001} surface ranging from 15Å-30Å.

3.4.4 MnO_2 {111} Nanotube

Figure 22 below shows a MnO_2 nanotube generated from {111} surface with diameter ranging from 15Å-30Å. The nanotubes are wrapped a_around_b. Nanotube generated from {100} surface is composed of varying number of atoms relative to the size of the diameter. Thus, nanotubes with diameter 15Å has 204 atoms while 20Å, 25Å and 30Å are composed of 264, 336 and 396 atoms, respectively. For all the nanotubes, the inner layer is composed mostly of Mn and O atoms, while the outer layer is composed of Mn and O atoms. The cross-section area of tube decrease as the diameter is increased.

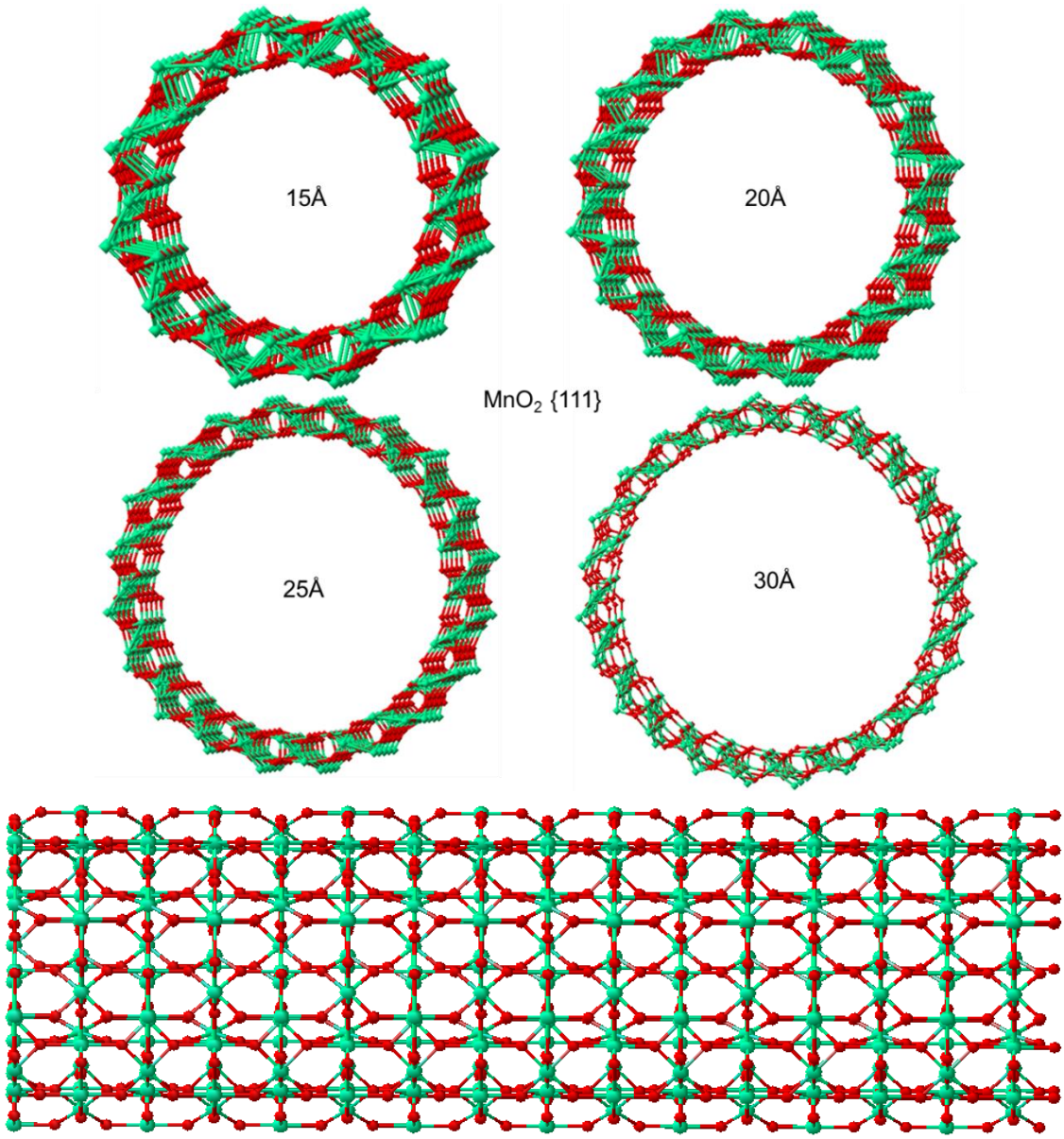

Figure 22: Cross-sectional view and long view of MnO_2 nanotube along {111} surface diameter ranging from 15Å-30Å.

3.5 MnO_2 Nanotube Length

The availability of nanotube sample with uniform length is essential to many specialised applications, such applications include biological imaging and sensing applications where shorter nanotube length may be required to penetrate cells and to serve as biological markers. The ability to control the length of the nanotube will allow control over their solubility, which will aid in the development of many applications as the dispersion of nanotubes into composites. The generation of long nanotubes with uniform length using experimental methods is difficult and challenging.

MnO_2 nanotubes are shown in figures 23 and 24. The figure reveal that nanotubes cut from same surface can produce nanotubes of different lengths depending on the size of the diameter. Figure 23 describes the cross-section and nanotube wall of MnO_2 nanotubes made from {110} surface with diameter of 11Å. This resemblance of the nanotubes is collectively known as a multi-walled nanotube (MWNT) as shown in figure 23(b). MWNTs that are composed of only two layers are known as double-walled nanotubes (DWNTs). Due to complexity and density of MnO_2 system, the generated nanotubes are found to be multi-walled nanotubes.

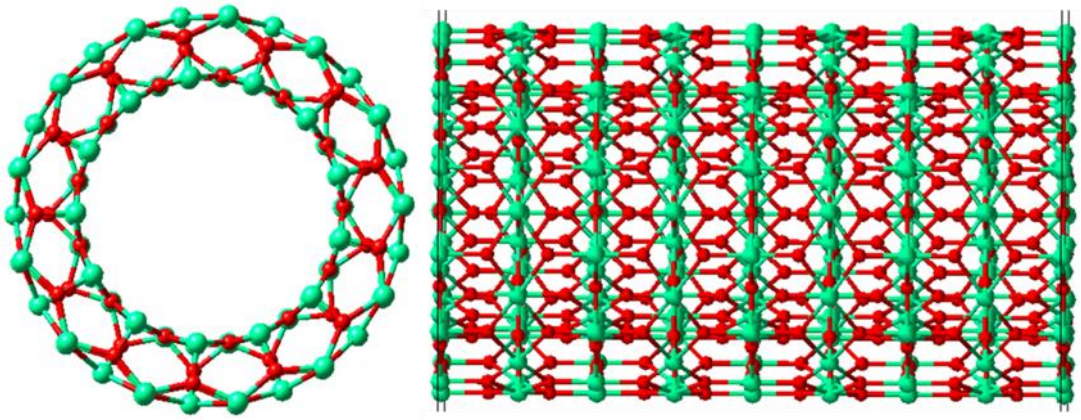

Figure 23: MnO_2 nanotubes made from {111} surface with diameter of 11Å, (a) shows the cross section of the nanotube and (b) shows the nanotube wall.

An isolated tube of only one layer is known as a single-walled nanotube (SWNT) shown in figure 24(b). Figure 24 show the cross-section and nanotube wall of MnO_2 nanotube generated from {111} surface with diameter of 9Å. Depending on how tightly the sheet has been rolled, one can easily envision tubes of different length. The long

nanotube with length exceeding the millimetre order greatly improves the electrical conductivity and mechanical strength. From computer simulations, this can be achieved by controlling the strain applied when rolling the nanotube.

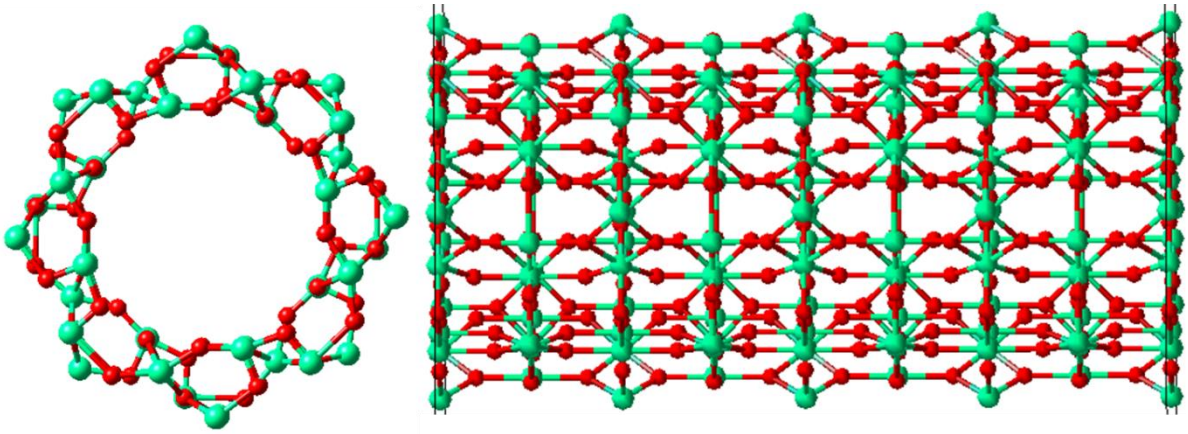

(a) (b)

Figure 24: MnO_2 nanotubes generated from {111} surface with diameter of 9Å, shows the cross section of the nanotube and (b) shows the nanotube wall.

3.6 Bond Length of MnO_2 Nanotubes

3.6.1 MnO_2 {100} Nanotube Bond Length

Another important aspect in nanotube structures is that the average bond lengths in the nanotubes are different from the counterpart bulk system. The bond length changes as the diameter of the nanotubes changes, due to the curvature of the nanotube side wall. The curvature bonding provides the nanotube structures with their unique strength. Figure 25 shows average bond length of MnO_2 {100} nanotube with diameter of 5Å and 7Å. The average bond length of nanotube changes as the diameter is changing. For 5Å nanotube the inner Mn atoms are octahedrally coordinated and the average bond length between Mn-O is equal to 1.74Å, while for 7Å nanotube the average bond length between Mn-O is equal to 1.79Å. As the diameter increases the average bond length increases. The average bond length is lower than the average bond length for bulk system which is reported 1.91Å [45]. The outer average bond distance for 5Å nanotube equal to 3.34Å while for 7Å nanotube the outer average bond distance equal to 3.03Å.

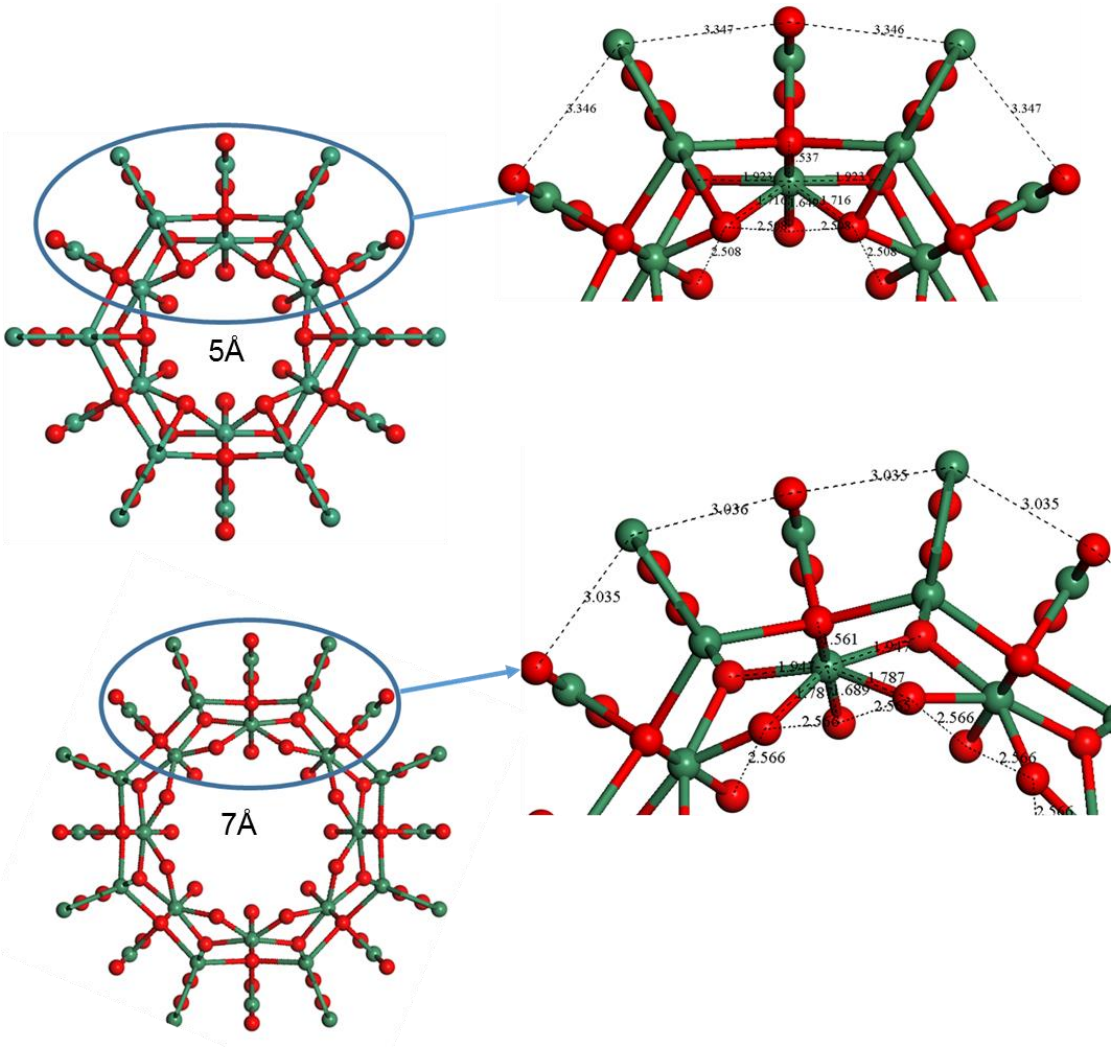

Figure 25: Bond length of {100} MnO_2 nanotube with diameter of 5Å and 7Å.

Figure 26 shows the bond length of MnO_2 nanotube with diameter of 9Å and 11Å. Manganese atoms in both nanotubes are octahedrally coordinated. The average bond length between Mn-O for 9Å nanotube equals to 1.81Å while for 11Å nanotube the average bond length between Mn-O equals to 1.74Å. Different size of nanotube diameters result in systems with different average bond lengths. Both 9Å and 11Å nanotubes, the inner layers consist of O atoms and the average bond length equal to 2.60Å and 2.57Å, respectively. The outer average bond length for 9Å nanotube is 2.84Å while for 11Å nanotube the outer average bond length equal to 2.53Å.

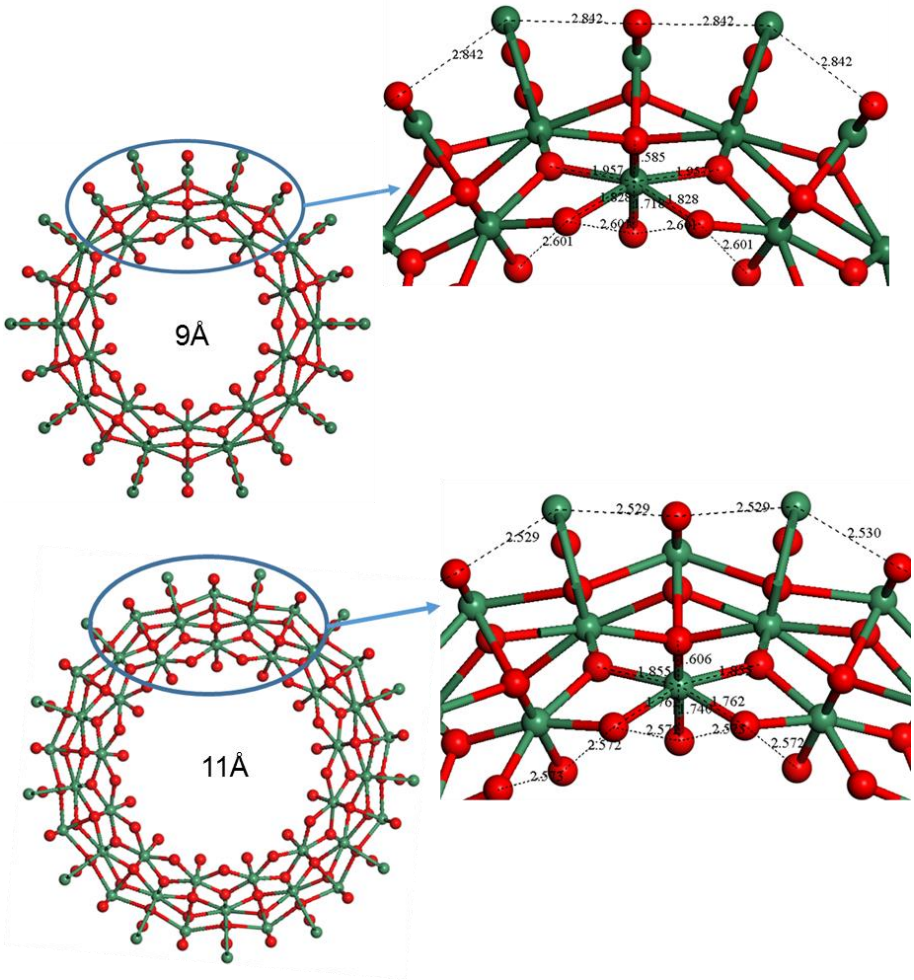

Figure 26: Bond length of {100} MnO_2 nanotube with diameter of 9Å and 11Å.

3.6.2 MnO_2 {110} Nanotube Bond Length

In this section two different nanotube structures were cut from different position on {110} surface. Figure 27 shows bond length of MnO_2 nanotubes rolled from {110} surfaces with diameter of 5Å and 7Å. The Mn-O average bond lengths for 5Å and 7Å nanotubes are 1.52Å and 1.64Å, respectively, which are less than the bond length of MnO_2 bulk structure. For 5Å nanotube the average bond length of the nearest two atom equal to 2.96Å for an outer layer and for inner layer is equal to 2.00Å while for 7Å the average bond length for the nearest atom equals to 2.91Å for outer layer and for inner layer the average bond length equals to 2.29Å. It is observed that as the diameter of nanotube is changed the bond length between atoms could be stretched or compressed. This is due to strain applied to the system from different orientations. Other atoms move far from each other while some other atoms come closer to each other.

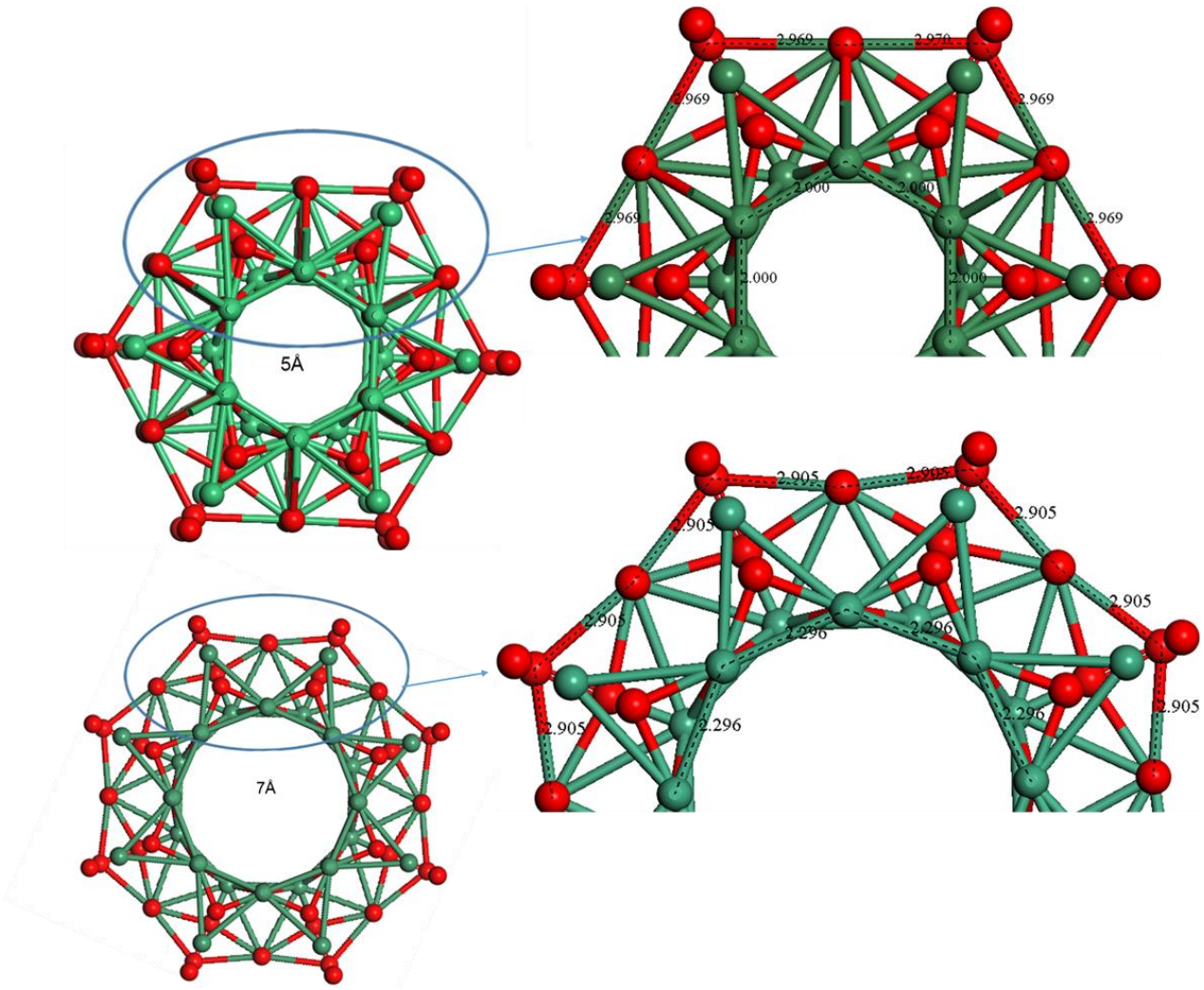

Figure 27: Bond length of {110} MnO_2 nanotube with diameter of 5Å and 7Å.

The average bond lengths of nanotube behave differently depending on the diameter of the nanotube. Figure 28 shows bond length of MnO_2 nanotubes rolled from {110} surfaces with diameter of 9Å and 11Å. The Mn-O average bond lengths for 9Å and 11Å nanotubes are 1.71Å and 1.67Å, respectively, and less than the bond length of MnO_2 bulk structure. For 9Å nanotube the average bond length of the nearest atoms on the outer layer is equal to 2.86Å and the inner layer equals to 2.47Å. As the diameter is increased to 11Å the outer layer compresses and equals to 2.72Å while the inner layer compresses to 2.39Å.

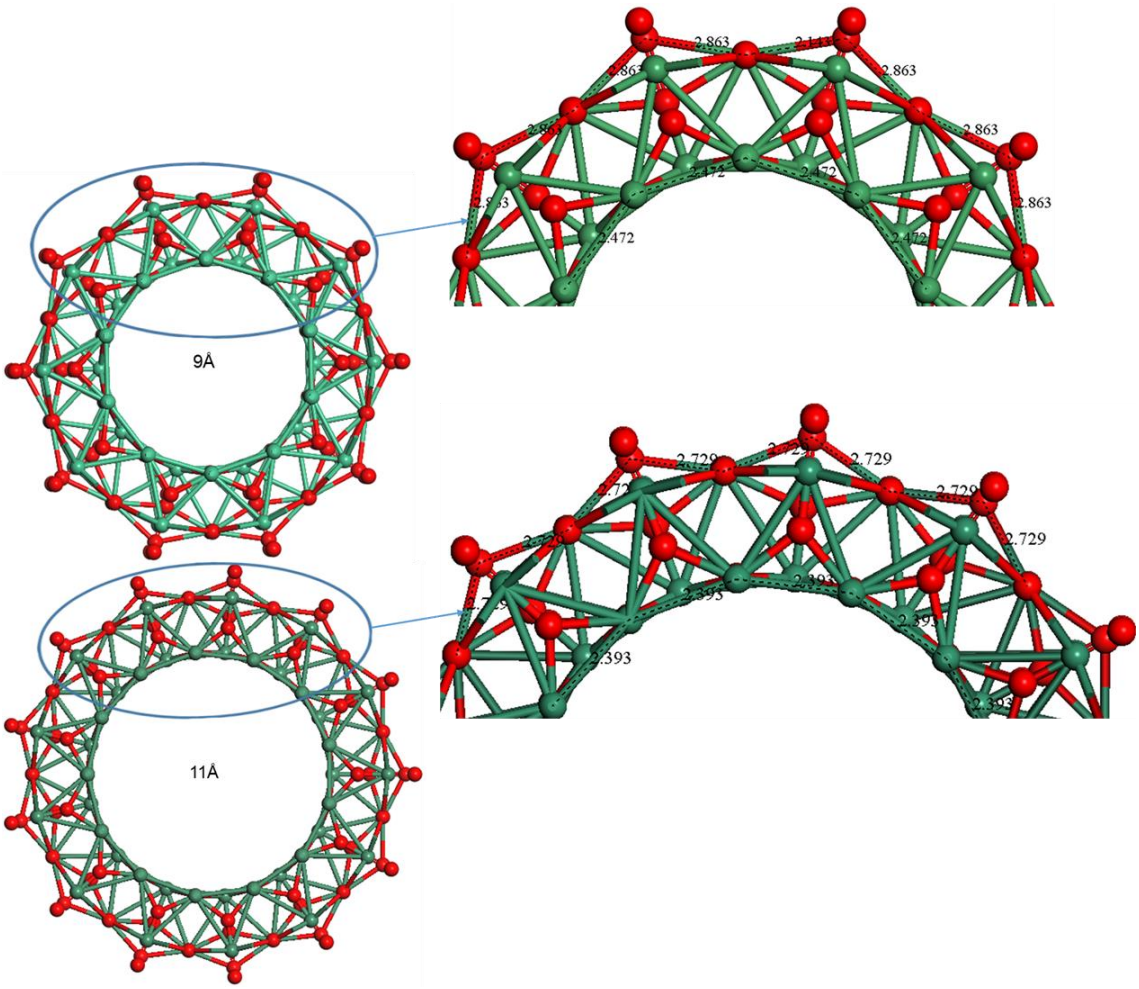

Figure 28: Bond length of {110} MnO_2 nanotube with diameter of 9Å and 11Å.

Figure 29 shows the bond length of MnO_2 {110} nanotubes with diameter of 5Å and 7Å. For 5Å nanotube inner layer consist of Mn-O atoms. The Mn-O average bond lengths equal to 1.52Å, while outer layer consist of O-O and the average bond length between the nearest O-O atoms equals to 3.22Å. For 7Å nanotube the Mn-O average bond length equals to 1.64Å and the outer layer consists of O-O, with an average bond length of 3.08Å.

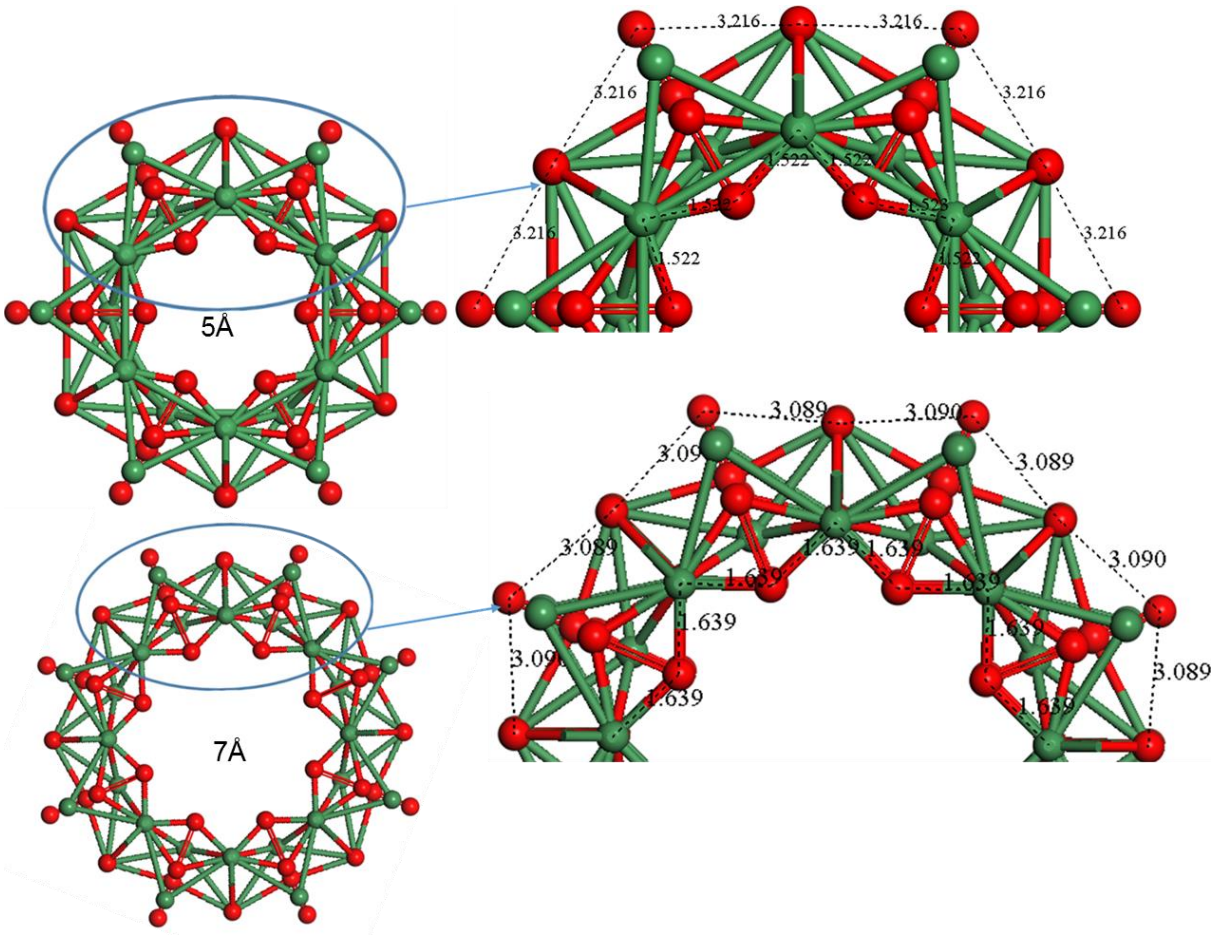

Figure 29: Bond length of {110} MnO_2 nanotube with diameter of 5Å and 7Å.

Figure 30 shows the average bond length of MnO_2 {110} nanotube with diameter of 9Å and 11Å. The calculated average bond lengths of 9Å and 11Å nanotubes are less than the average bond length of the bulk as observed with other nanotubes from different surfaces. For 9Å nanotube inner layer consists of Mn-O atoms. The Mn-O average bond lengths equal to 1.71Å, while outer layer consisting of oxygen atoms with an average bond length of 3.01Å. The 11Å nanotube also consists of Mn-O atoms on the inner surface, with Mn-O an average bond length of 1.67Å while the outer layer consists of O-O atoms with an average bond length of 2.84Å.

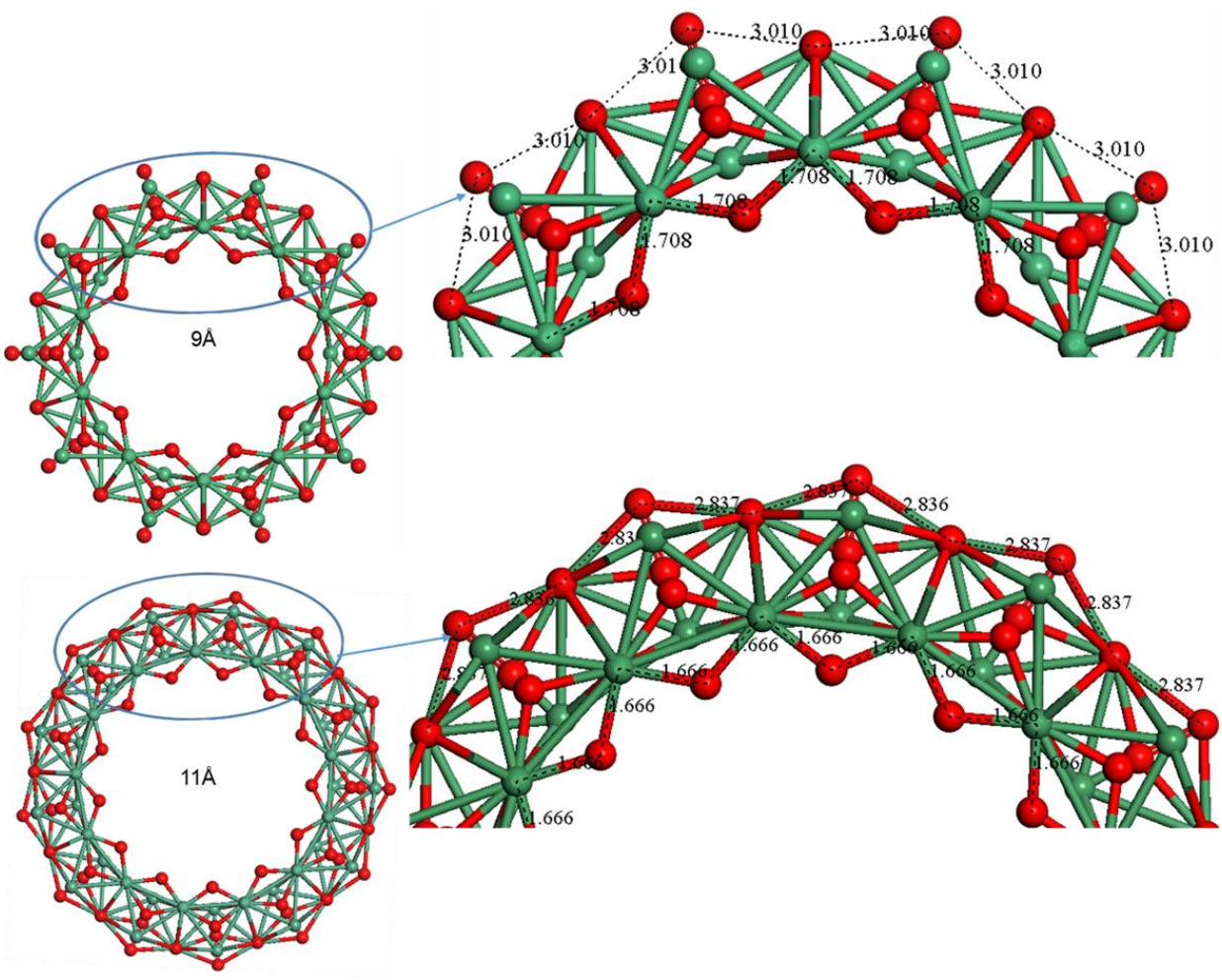

Figure 30: Bond length of {110} MnO_2 nanotube with diameter of 9Å and 11Å.

3.6.3 MnO_2 {111} Nanotube Bond Length

Figure 31 and figure 32 shows the average bond length of MnO_2 {111} nanotube with diameter ranging from 5Å-11Å. As it has been discussed previously that the size of the diameter has an effect on morphology of the nanotubes, increasing the diameter tends to shape the nanotubes into more spherical shape. Both nanotubes (5Å and 7Å) have the inner and outer layer consisting of Mn and O atoms. The Mn-O average bond length for 5Å and 7Å nanotubes equal to 2.02Å and 1.84Å, respectively, which are relatively closer to the measured bond length for the bulk system. Compared to other nanotubes from different surfaces, this surface gives the results that are closer to measured value for the system.

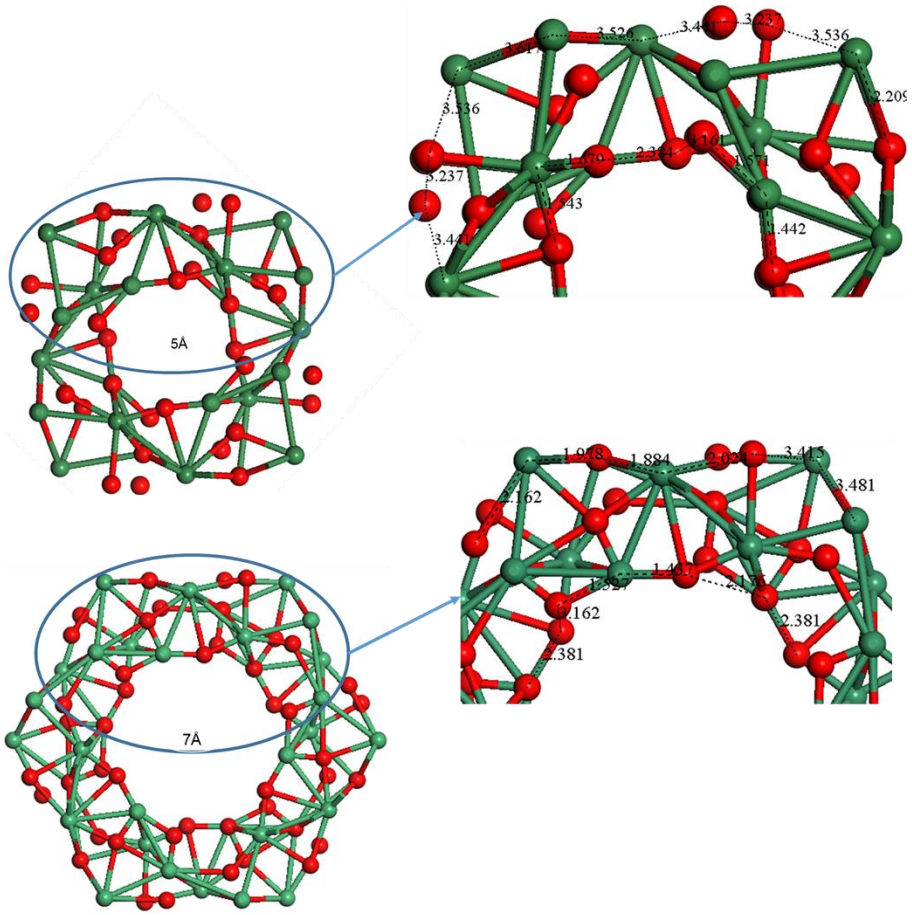

Figure 31: Bond length of {111} MnO_2 nanotube with diameter of 5Å and 7Å.

Figure 32 shows the average bond length of MnO_2 nanotube with diameter of 9Å and 11Å. All the nanotubes give different average bond length. Both 9Å and 11Å nanotubes have their inner and outer layers consisting of Mn and O atoms. The Mn-O average bond lengths for 9Å and 11Å nanotubes equal to 1.77Å and 1.76Å respectively. A summary of bond length results is presented in table 3. The Mn-O, O-O and Mn-Mn average bond lengths for various nanotubes discussed are presented. As the diameter increases average bond length Mn-O and Mn-Mn decreases while there is no trend on average bond length O-O. This could be attributed to the fact that, at times nanotube contract/expand on the inner/outer layer and vice versa. However, all the calculated bond distances are below the value for the counterpart bulk system, with an exception of {111} 5Å nanotube.

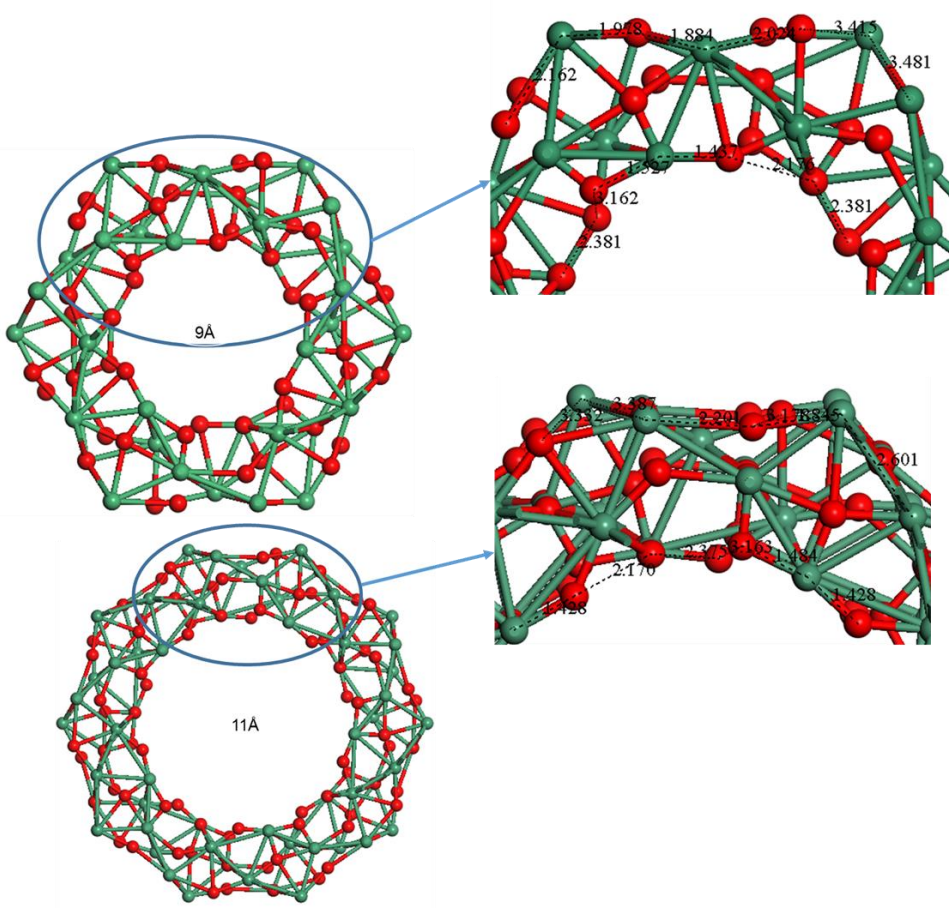

Figure 32: Bond length of {111} MnO_2 nanotube with diameter of 9Å and 11Å.

Table 3: Average bond lengths for various MnO_2 nanotubes

		Mn-O(Å)	O-O(Å)	Mn-Mn(Å)
Bulk MnO_2		1.57	2.87	2.76
Miller index	Diameter (Å)	Mn-O(Å)	O-O(Å)	Mn-Mn(Å)
{100}	5	1.74	2.51	2.25
	7	1.79	2.56	2.30
	9	1.81	2.60	2.36
	11	1.74	2.57	2.42
{110}	5	1.52	2.00	2.53
	7	1.64	2.29	2.57
	9	1.71	2.47	2.61
	11	1.67	2.39	2.56

{111}	5	2.02	2.31	2.63
	7	1.84	2.27	2.39
	9	1.77	2.38	2.37
	11	1.67	2.37	2.36

3.7 Lattice Parameters for MnO_2 Nanotubes

Tables 3-6 show the lattice parameter for MnO_2 nanotube structures, with different Miller indices and diameter ranging from 5Å-30Å. The tables depict that the diameter has an effect on the cell parameters of the generated nanotube. It is observed that as the diameter is increased, the cell parameter a increases while cell parameter c remains constant. Similar trend is observed for all nanotubes with different Miller indices as shown in table 4-7. For {100} surface the lattice parameter a for small diameter (5Å) nanotube is 24.842Å while for 30Å the lattice parameter a equal to 53.131Å. {001} surface gave 5Å nanotube with the least lattice parameter of 17.35Å.

Table 4: Lattice parameters for MnO_2 nanotube along {100} surface

Index	Diameter (Å)	Cell Parameters (Å)
{100}	5	a=24.842, c=4.398
{100}	7	a=27.368, c=4.398
{100}	9	a=29.811, c=4.398
{100}	11	a=32.188, c=4.398
{100}	15	a=36.796, c=4.398
{100}	20	a=42.365, c=4.398
{100}	25	a=47.795, c=4.398
{100}	30	a=53.131, c=4.398

Table 5: Lattice parameters for MnO_2 nanotube along {110} surface

Index	Diameter (Å)	Cell Parameters (Å)
{110}	5	a=21.675, c=6.220
{110}	7	a=24.068, c=6.220
{110}	9	a=26.378, c=6.220
{110}	11	a=28.011, c=6.220

{110}	15	a=33.011, c=2.873
{110}	20	a=38.345, c=2.873
{110}	25	a=43.383, c=2.873
{110}	30	a=48.762, c=2.873

Table 6: Lattice parameters for MnO_2 nanotube along {001} surface

Index	Diameter (Å)	Cell Parameters (Å)
{001}	5	a=17.358, c=4.398
{001}	7	a=19.454, c=4.398
{001}	9	a=21.525, c=4.398
{001}	11	a=23.573, c=4.398
{001}	15	a=27.642, c=4.398
{001}	20	a=32.692, c=4.398
{001}	25	a=37.724, c=4.398
{001}	30	a=42.747, c=4.398

Table 7: Lattice parameters for MnO_2 nanotube along {111} surface

Index	Diameter (Å)	Cell Parameters (Å)
{111}	5	a=19.838, c=6,220
{111}	7	a=22.122, c=6.220
{111}	9	a=24.334, c=6.220
{111}	11	a=26.498, c=6.220
{111}	15	a=30.736, c=6.220
{111}	20	a=35.934, c=6.220
{111}	25	a=41.880, c=6.220
{111}	30	a=46.168, c=6.220

3.8 Radial Distribution Functions for MnO_2 Nanotube

In this section radial distribution functions (RDFs) for {110} nanotube with diameter of 25Å are discussed. Molecular dynamics simulations were carried out to study the configuration energy and radial distribution functions of MnO_2 {110} nanotube at different temperatures. Radial distribution function is a pair of correlation function, which is used to describe the structure of various systems. It describes how the atoms in a particular system are radially packed around each other. The radial distribution functions at different temperatures for MnO_2 nanotube structure are presented, wherein the radial distribution functions for Mn-Mn, Mn-O and O-O pairs at various temperatures are shown. Figure 33 shows the calculated RDFs for the nanotube model obtained by molecular dynamics simulations. At temperature 300K, the peak occurs at approximately r= 3.4Å for O-O pair and pair distribution function g(r) = 4.5, for Mn-O pair the peak occurs at r=2.1Å with g(r) = 34.5 and for Mn-Mn pair the first peak occurs at r= 3.7Å with g(r) = 8.53.

Figure 34 shows the calculated RDFs for the nanotube at the temperature of 1500K. The RDFs for all these three pairs has an effect on the peak broadening. As the temperature is increased the peaks become broader, this depicts that the nanotubes becomes disordered. There is a decrease in peak height as the temperature is increased. This can be easily seen at temperature 3300K shown in figure 35. The first peak occurs approximately at r= 3.5Å for O-O pair and g(r) =2.0. Mn-O pair, the peak occurs at r= 2.1Å and g(r) =9.2 at temperature 3300K. The same behaviour of g(r) decreases with increase in temperature is observed with Mn- Mn pair with g(r) = 2.4.

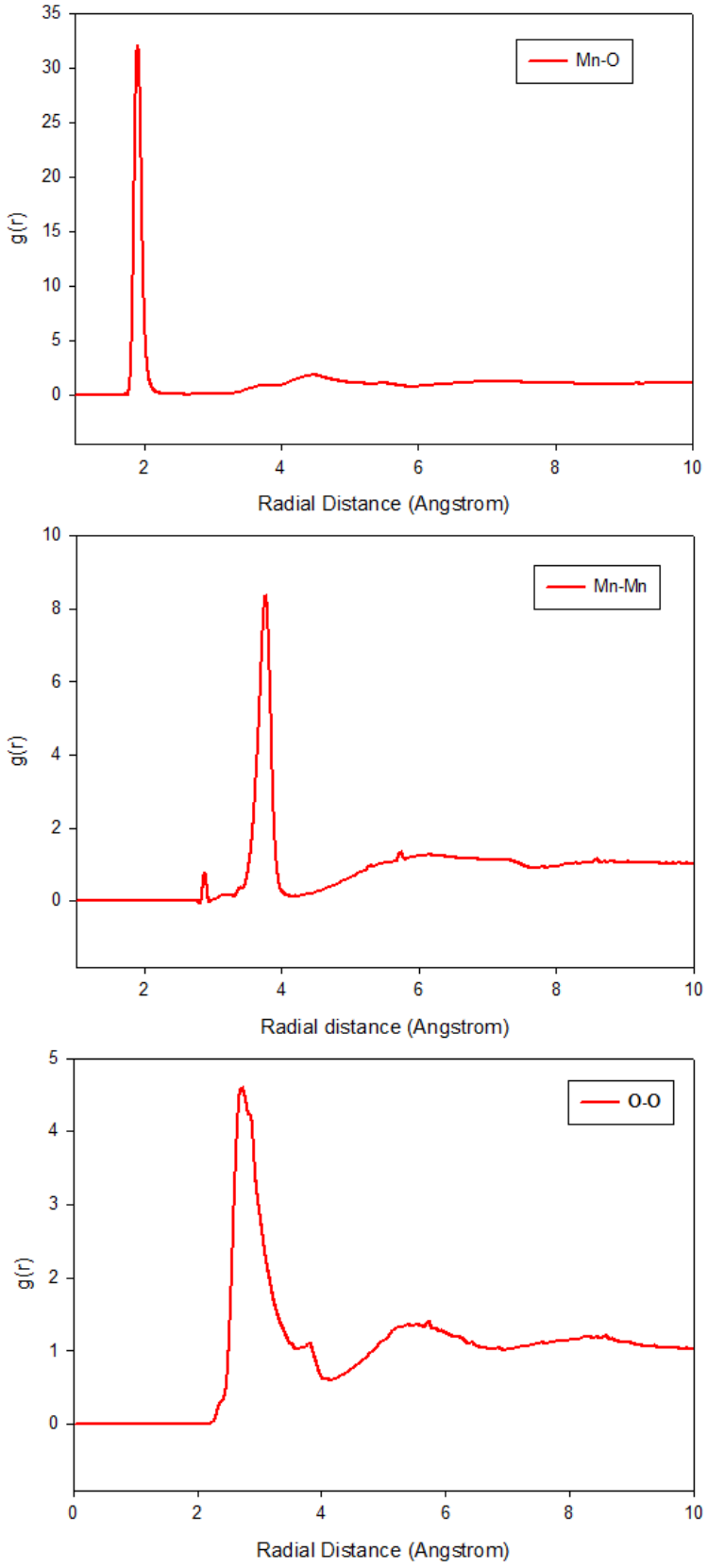

Figure 33: Graphs of g(r) and radial distance showing the partial radial distribution function of Mn-O, Mn-Mn and O-O at 300K.

Figure 34 shows partial radial distribution function for Mn-O, Mn-Mn and O-O at 1500K. The graphs show that all the peaks appear at the same position irrespective of the temperature, while the the value of g(r) is decreasing.

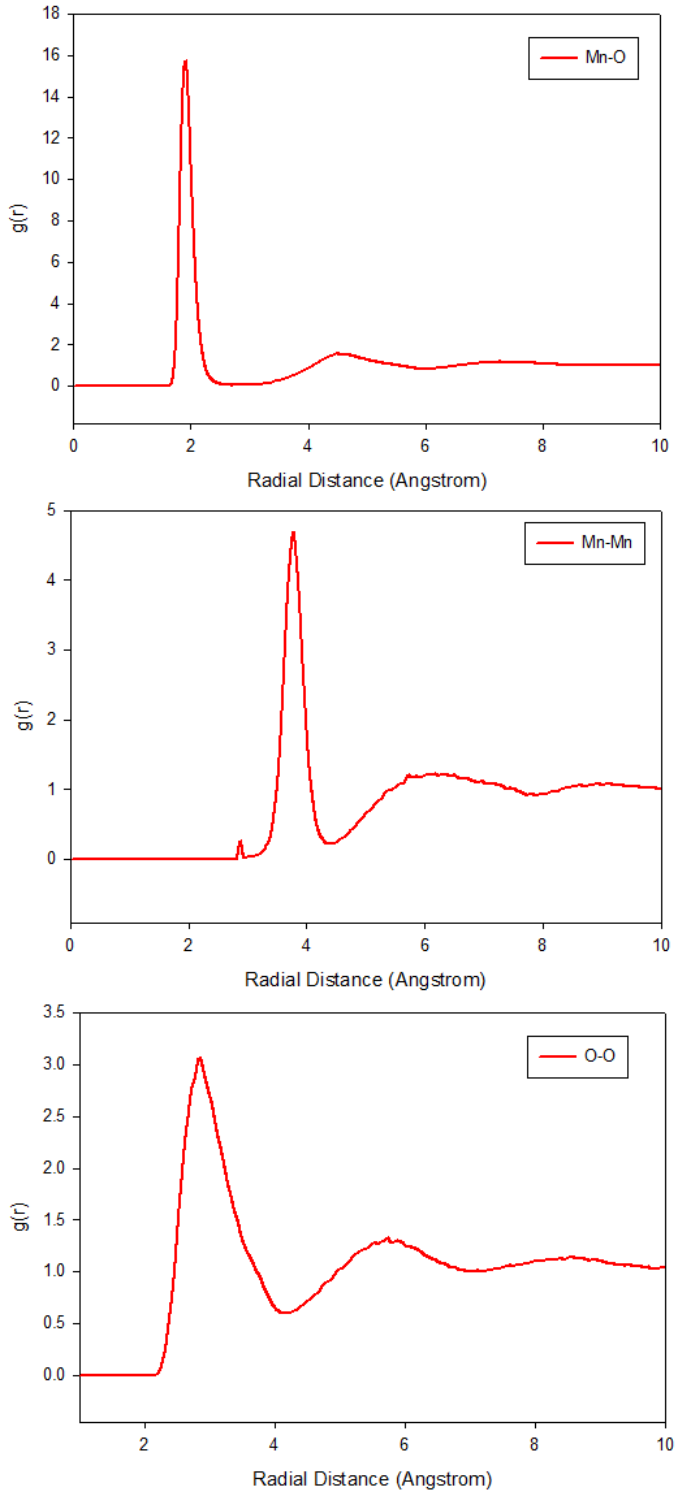

Figure 34: Graphs of g(r) and radial distance showing the partial radial distribution function of Mn-O, Mn-Mn and O-O at 1500K.

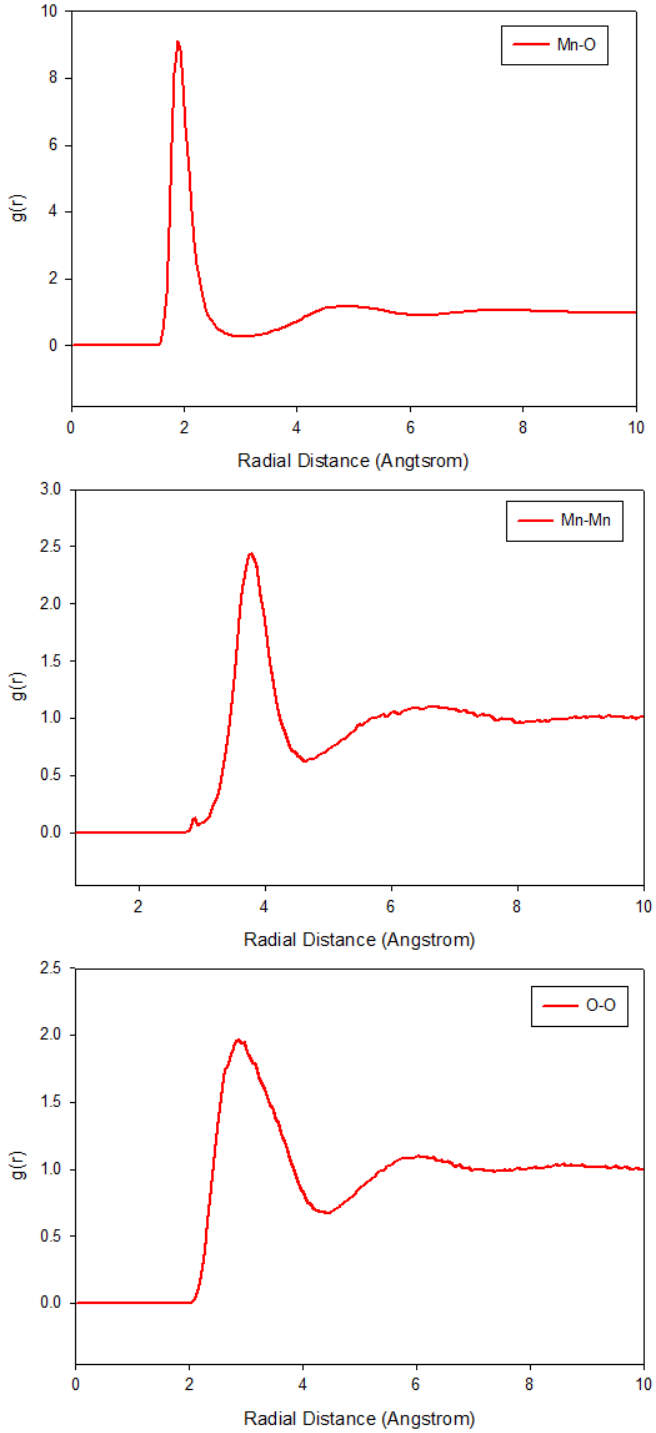

Figure 35: Graphs of g(r) and radial distance showing the partial radial distribution function of Mn-O, Mn-Mn and O-O at 3300K.

Figure 36 shows graphs of g(r) and radial distance showing the partial radial distribution function of Mn-O, Mn- Mn and O-O pairs at various temperatures. The peaks occur almost at the same distances irrespective of the temperature. Temperature has no effect on peak position, however it is noted that the higher the

temperature the higher the disorder in the system and the lower the value of g(r). Furthermore, the effect of temperature on the peaks is noted, as the temperature is increased the peaks become broad. This implies that the disorder within system is increased as the temperature increases while the value of g(r) decreases.

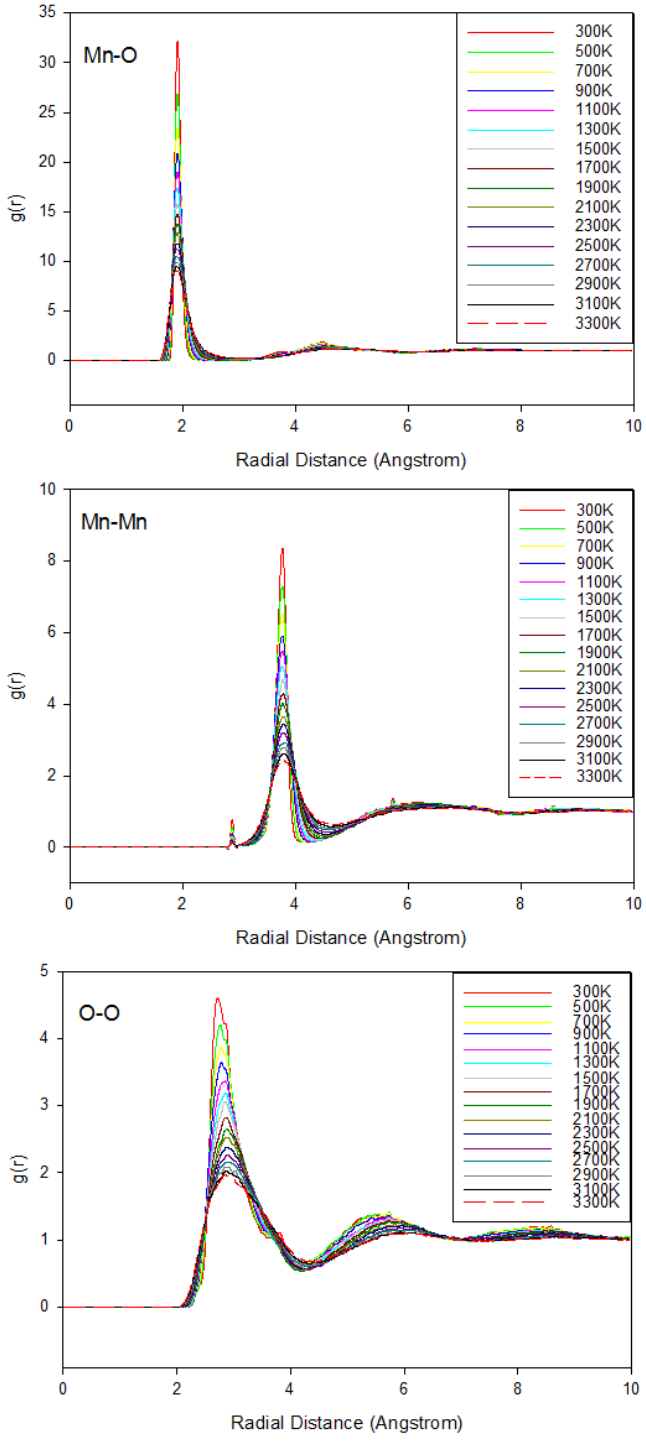

Figure 36: Graphs of g(r) and radial distance showing the partial radial distribution function of Mn-O, Mn-Mn and O-O at various temperatures.

Figure 37 shows the total energy versus temperature graph, wherein the phase changed properties are discussed. It is observed that the total energy of the system is directly proportional to the temperature, thus as the temperature increases the total energy of the system increases as well. The graph shows three regions, where (i) from 300K to ~2500K the total energy is increasing linearly with temperature, (ii) total energy jumps between 2500K and 3000K (iii) another linear increase from 3000K. The phase transition is noted at approximately ~2500K. With the increase of temperature the energy of MnO_2 nanotube increases and the discontinuity appear on the energy-temperature curve at 2700K. Before and after the discontinuity the curve is approximately linear.

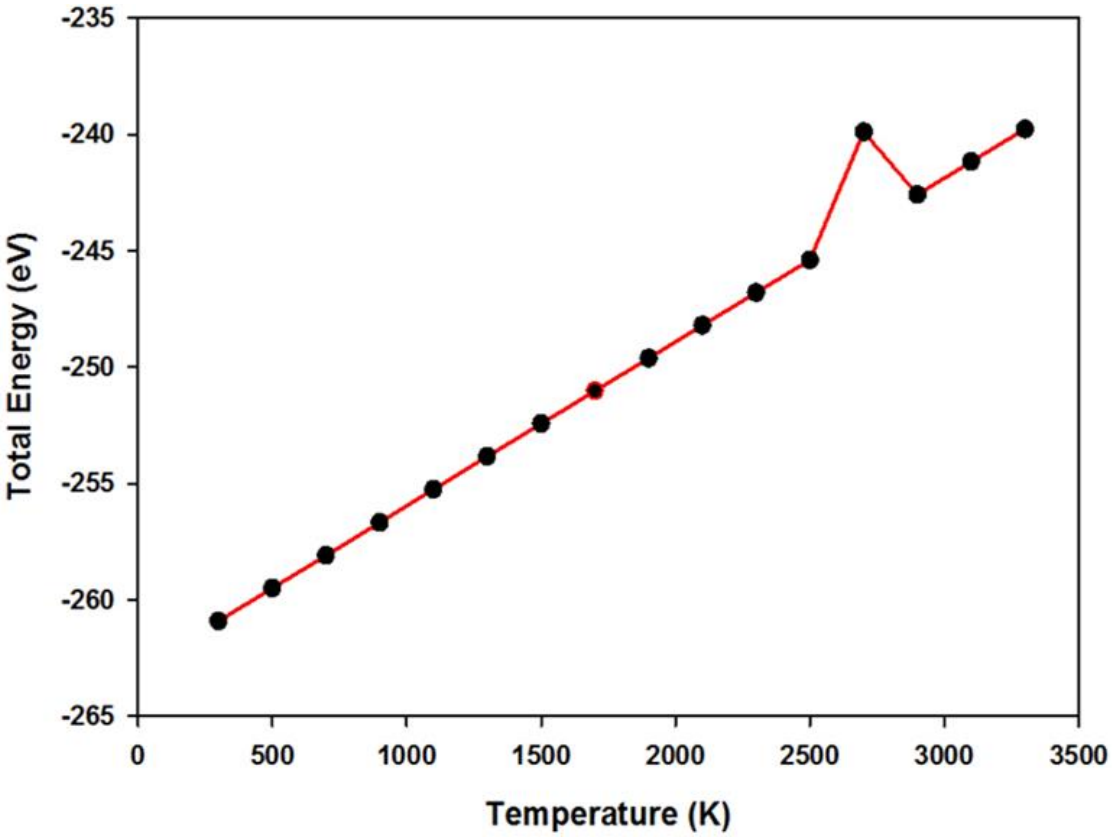

Figure 37: Total energy as a function of temperature graph for MnO_2 nanotube.

3.9 XRD Patterns for MnO_2 Nanotubes

X-ray powder diffraction (XRD) is a rapid analytical technique primarily used for phase identification of a crystalline material and can provide information on unit cell dimensions. Powder diffraction techniques have a wide variety of applications in compositional, structural, microstructural and many other areas. The XRD has become a cornerstone technique for deriving crystallite size in nano-science due to speed and accuracy. The intensity of the peaks is determined by the arrangement of the atoms within the crystal. The position of the peaks in the powder pattern determines the size, shape and symmetry of the unit cell and also position of the peak corresponds to the average spacing between the atoms.

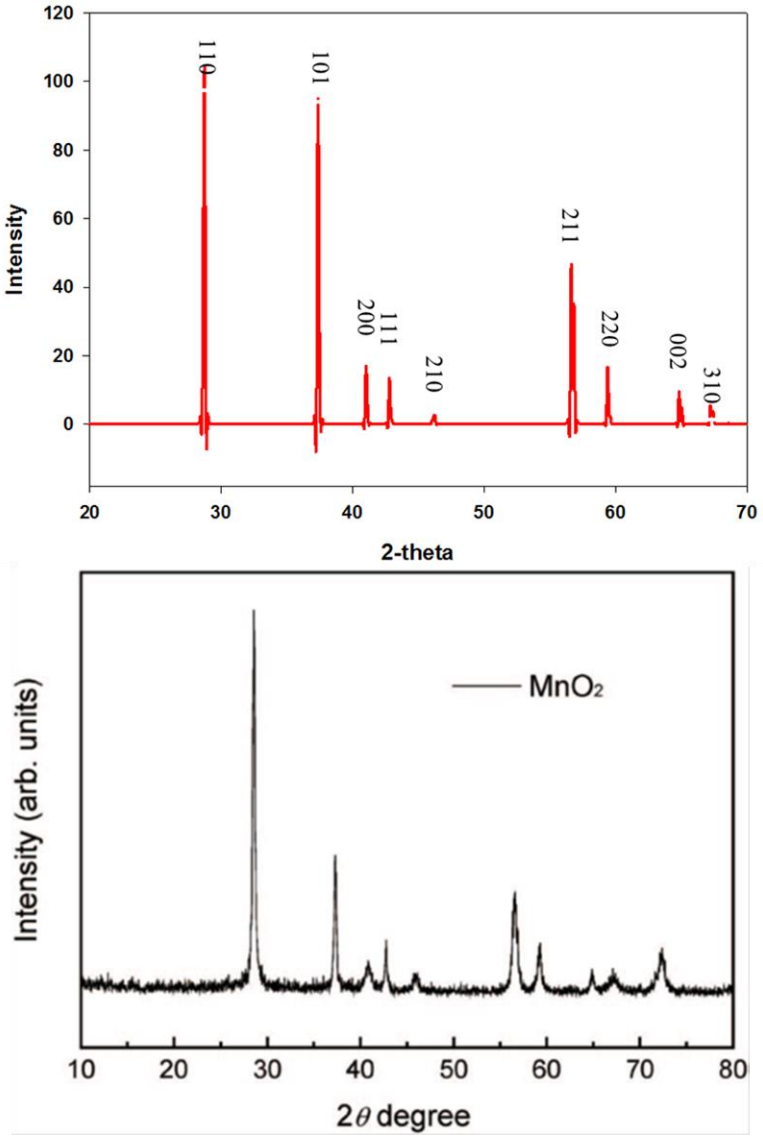

Figure 38: Calculated and experimental XRD [43] patterns for MnO_2.

In the study of nanostructures, the crystallite size is usually the sole factor of interest. The peak broadening of reflections in a power diffraction pattern contains much information, such as crystallite strain, shape and stacking faults, which are often not considered. For samples that are too small to be studied by X-ray diffraction, electron crystallography provides the best tool for structure determination. Figure 38 shows the calculated and experimental X-ray patterns for spinel MnO_2 bulk structure. Calculated and experimental [43] X-ray patterns are in good agreement, all the peaks appears at the same position of 2θ. This validates the bulk model that was used as the parent material, from which the surfaces were cut.

3.9.1 MnO_2 {100} Nanotube

XRD patterns are a non-destructive technique used to identify crystalline phases, arrangement of atoms and orientation. Also, they are used to determine structural properties, such as lattice parameters, phase compositions, preferred orientation and thermal expansion. In this subsection, different XRD patterns for MnO_2 nanotubes with smaller diameter 5Å-11Å are calculated and discussed. Figure 39 shows typical XRD patterns for MnO_2 nanotube generated from {100} surface with diameters of 5Å and 7Å. Intensities of nanotubes appear at different 2θ positions depending on the internal diameter of the nanotube. The calculated XRD patterns predict that for 5Å and 7Å the first peaks appear at the same 2θ position but the intensity of the peaks from two different systems differ. The intensities of all the peaks of nanotube 5Å are higher than the intensity of the nanotube with 7Å. XRD patterns for 5Å nanotube have 3 highest peak indexed as {200}, {220} and {310} positioned at 20.2 2θ, 30.6 2θ and 33.4 2θ, respectively, while for 7Å nanotube have only one highest peak that is indexed as {310} positioned at 30.3 2θ. Some of the peaks in XRD pattern for nanotube of 5Å disappear when the diameter is increased to 7Å.

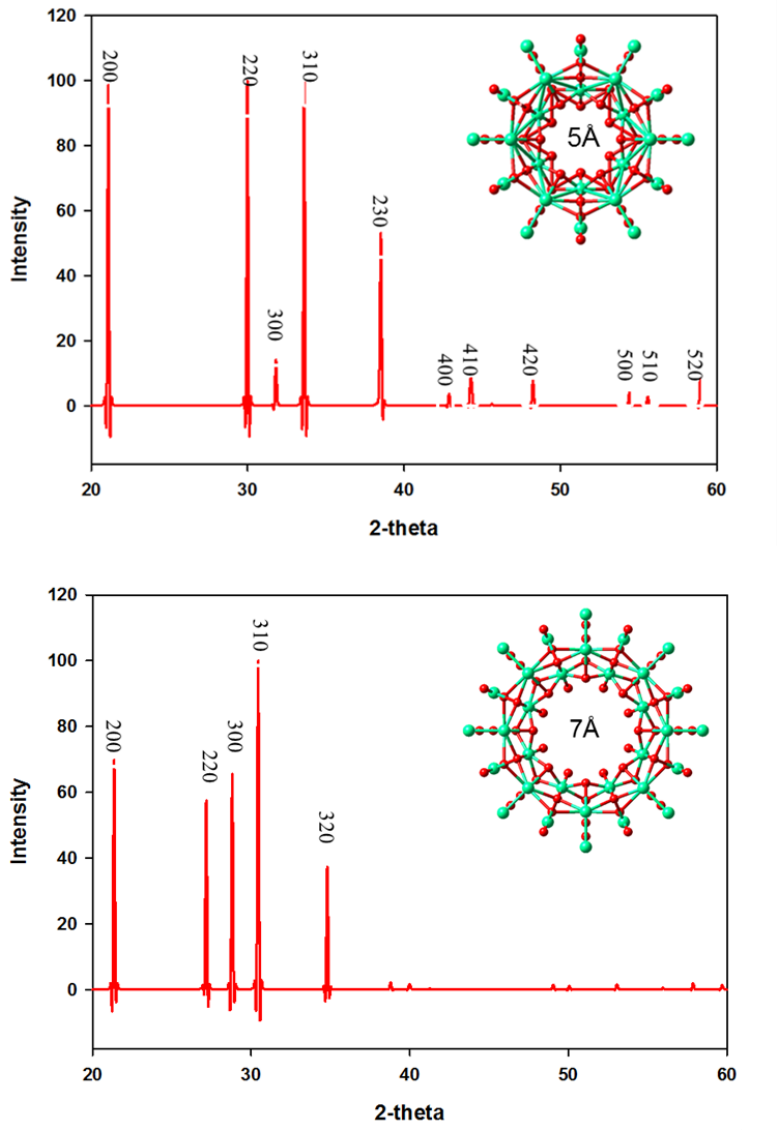

Figure 39: XRD for MnO_2 nanotube generated from {100} surface with diameter of 5Å and 7Å.

Figure 40 shows the XRD patterns for MnO_2 nanotube generated from {100} surface with the diameter of 9Å and 11Å. The calculated XRD patterns predict that for 9Å nanotube has only four peaks, with only two highest peaks indexed {320} and {310} positioned at 25.1 2θ and 28.5 2θ, respectively, while the XRD for 7Å nanotube has two highest peaks indexed {220} and {310} that are position at 24.6 2θ and 25.2 2θ, respectively. Differences in the atomic structure are reflected by differences in XRD patterns for various systems. Different XRD patterns for nanotubes with sizes of diameter, imply that the atomic arrangement of the nanotube is different. This was confirmed by calculated bond lengths of the nanotubes. The XRD patterns reveal that even though the atomic configurations look similar, there are slight difference in terms of atomic arrangements.

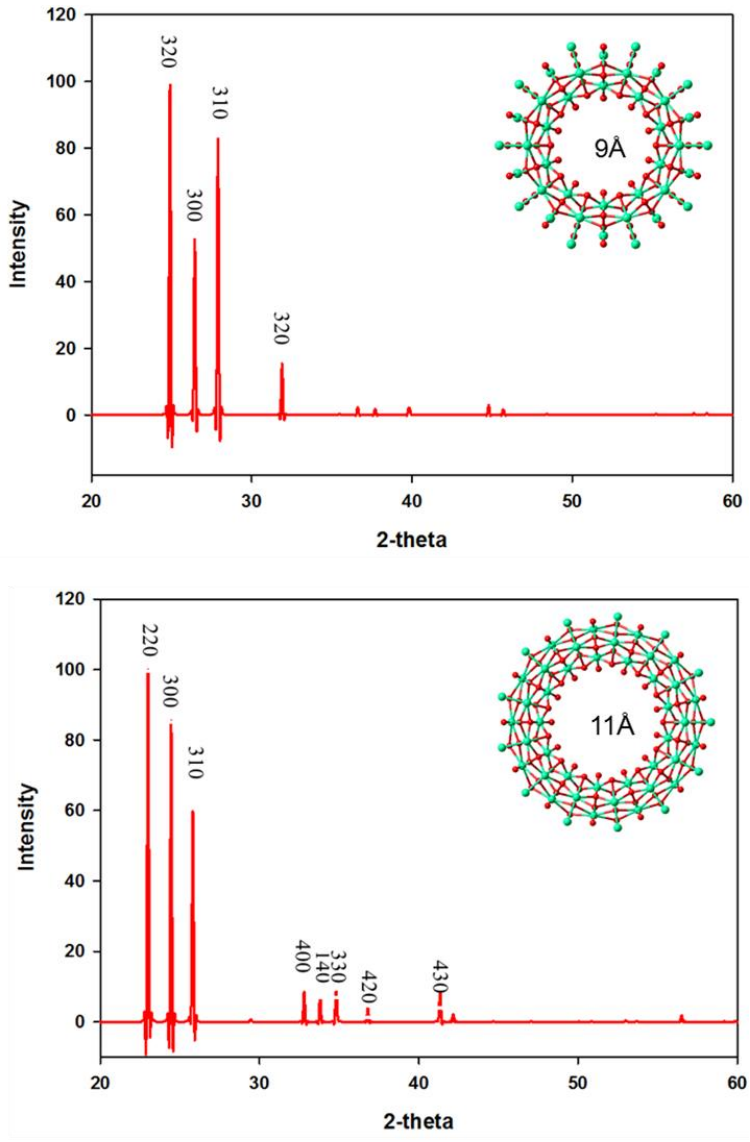

Figure 40: XRD for MnO_2 nanotube generated from {100} surface with diameter of 9Å and 11Å.

3.9.2 MnO_2 {110} Nanotube

In this section, different XRD patterns for MnO_2 {110} nanotubes with smaller diameter (5Å-11Å) are calculated and discussed. Figure 41 shows typical XRD for MnO_2 nanotube generated from {110} surface with a diameter of 5Å and 7Å. The intensity of the peak depends on the diameter of the nanotubes. The calculated XRD patterns predict that for 5Å nanotube the first peak appears at 22.3 2θ, with the index of {200} while for 7Å the first peak appears at 21.2 2θ with the same index of {200}. It is predicted that the first peaks for 5Å and 7Å diameter have the same index, with different intensities.

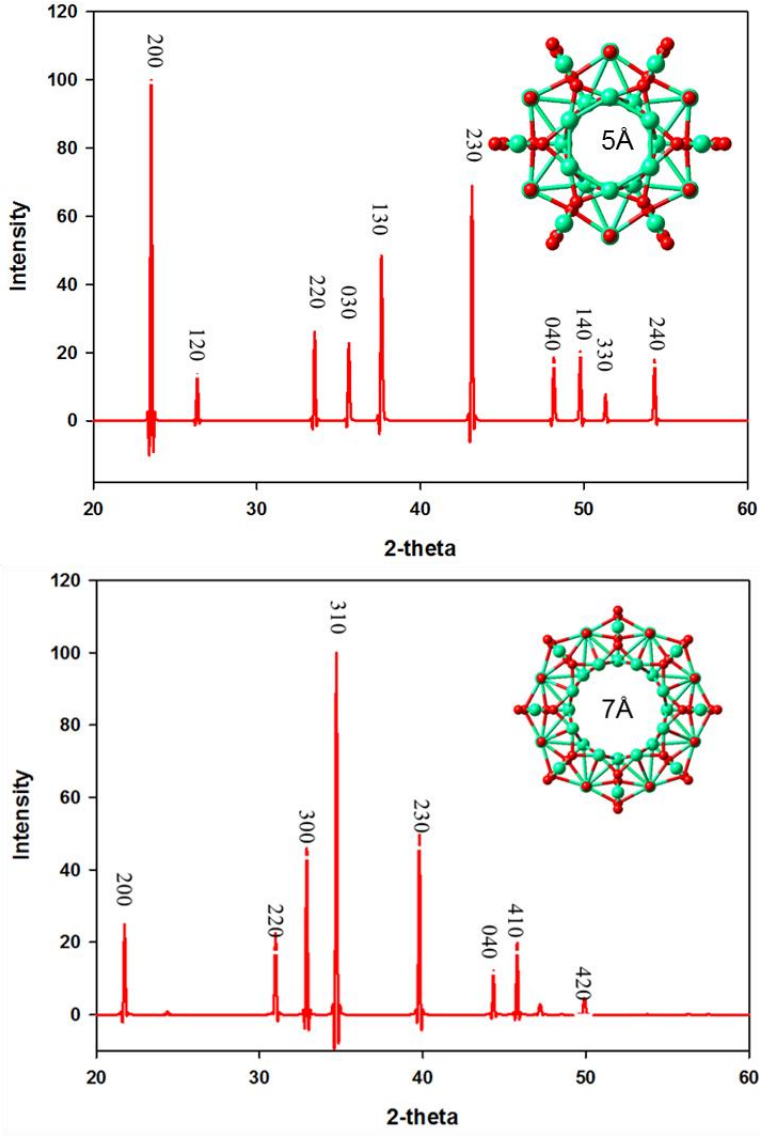

Figure 41: XRD for MnO_2 nanotube generated from {110} surface with diameter of 5Å and 7Å.

Figure 42 shows the XRD patterns for MnO_2 nanotube generated from {100} surface with the diameter of 9Å and 11Å. The calculated XRD patterns predict that for 9Å nanotubes most of the peaks have high intensity than the calculated XRD for 11Å. The diameter has an effect on the intensity of the peaks as observed previously. As the diameter is increased the atomic position changes which results in a different peak position. For 9Å nanotube, there are three highest peaks indexed {120}, {130} and {220} while 11Å nanotube has {120} plane as the only peak with highest intensity. These suggest that there is crystal re-orientation as diameter of the nanotubes is changed.

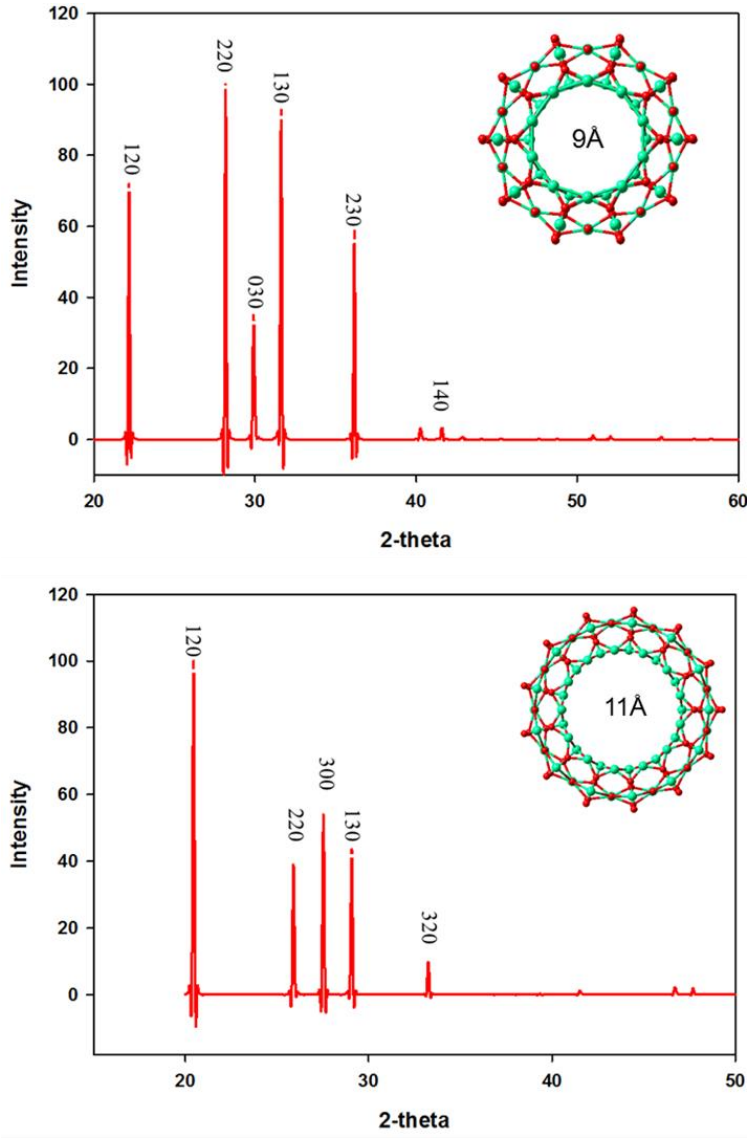

Figure 42: XRD for MnO_2 nanotube generated from {110} surface with diameter of 9Å and 11Å.

3.9.3 MnO_2 {111} Nanotube

The intensity of the peaks differ as the diameter is changed and also the position of the peaks changed as the diameter is increased. Variables such as temperature, pressure, index changes the average bond distances and d_{hkl}, hence, the diffraction peak positions change. Thus, the diffraction peak position is a product of the average atomic distances in the crystal. In this section different XRD patterns for MnO_2 {111} nanotubes with smaller diameter 5Å-11Å are calculated and discussed. Figure 43 shows the calculated XRD patterns for MnO_2 nanotube with diameter of 5Å and 7Å.

According to the calculated XRD patterns the intensity of the peaks on 5Å nanotube are stronger than the intensity of the peaks on 7Å nanotubes.

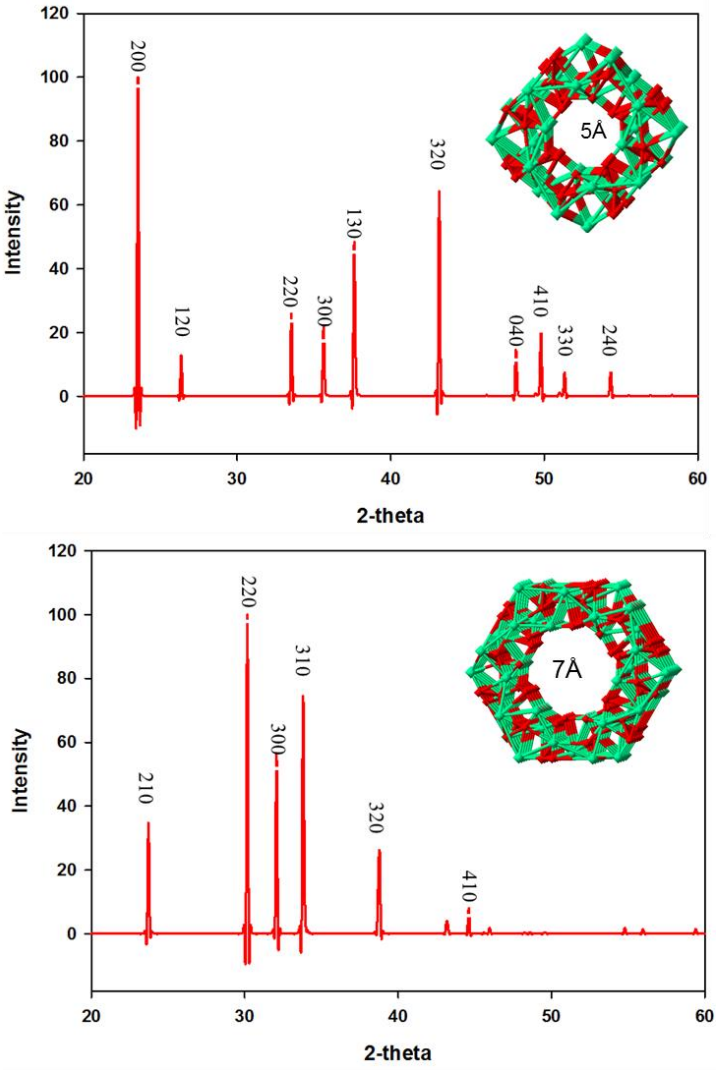

Figure 43: XRD for MnO_2 nanotube generated from {111} surface with diameter of 5Å and 7Å.

Figure 44 shows the calculated XRD patterns for MnO_2 nanotube with a diameter of 9Å and 11Å. The diffraction peak positions and diffraction peak intensity change as the diameter is changed. The nanotube 9Å has the highest peaks indexed {210} and {310}, their intensities are almost the same, while 11Å nanotube has the highest peak indexed as {220}. The peak position also changes as the diameter is changed. For 9Å the peaks {220}, {300} and {310} appears at 27.5 2θ, 29.5 2θ and 31.3 2θ, respectively

while for 11Å the peaks {220}, {300} and {310} appears at 25.3 2θ, 27 2θ and 29 2θ, respectively.

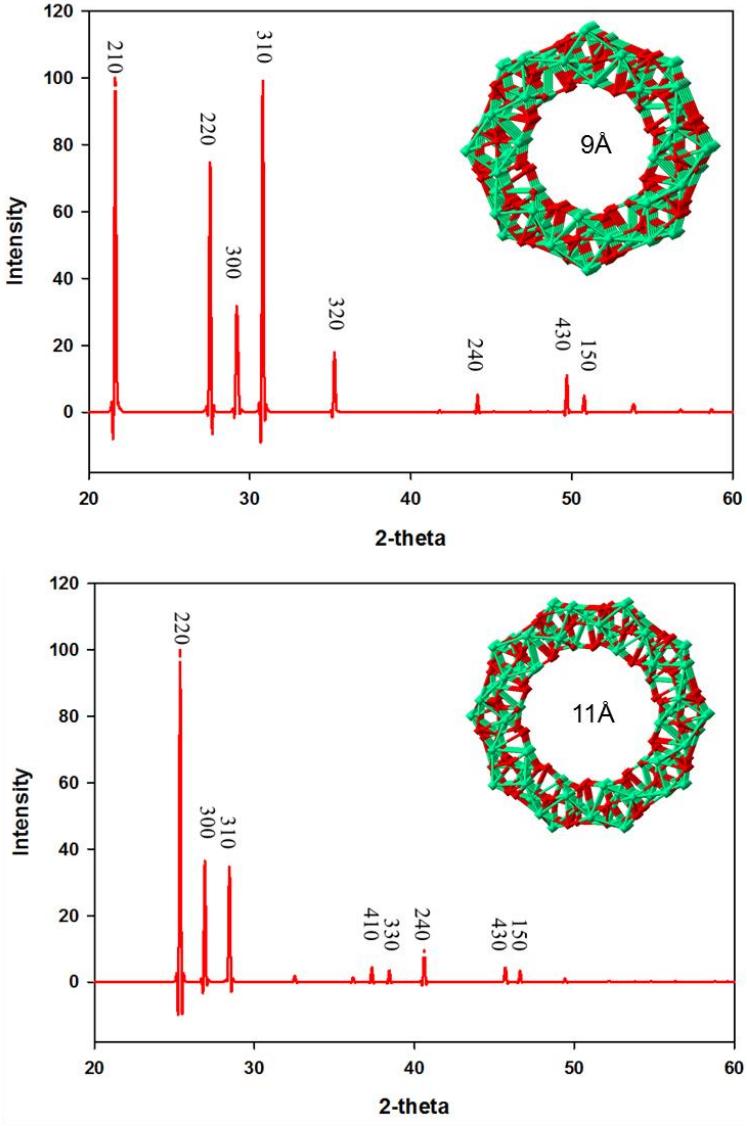

Figure 44: XRD for MnO_2 nanotube generated from {111} surface with diameter of 9Å and 11Å.

Chapter 4

$LiMn_2O_4$ Nanotubes Results and Discussion

4.1 Atomistic Simulation of Spinel $LiMn_2O_4$ Nanotube

Atomistic simulations of the lithium manganese oxide lattices were performed using two-body potentials for Mn-O, Li-O and O-O interactions. Interatomic interactions have already been successfully applied to model lithium insertion in spinel manganese oxide. However, a slight modification on ρ parameter for the Mn-O pair was implemented to further improve calculated structural parameters for spinel $LiMn_2O_4$. The shell model parameters were refined to achieve the best fit of the predicted wavenumbers of infrared and Raman-active vibrations to experimentally observed wavenumbers. Energy minimisation was performed to generate a relaxed equilibrium structure from which lattice parameters and atomic positions for $LiMn_2O_4$ are calculated. The interatomic potentials are based on Born model ionic solid, which includes a long-range Coulombic interaction and short-range term. The simulation of the lithium manganese oxide lattice were performed using two-body potentials for Mn-O, Li-O and O-O interatomic interaction which have already successfully applied to model lithium insertion in spinel manganese oxide. The potential parameters are listed in table 8.

Table 8: Interatomic potentials for spinel $LiMn_2O_4$ [89]. The cut-off 12Å was used.

Interaction	A(eV)	P(Å)	C(eVÅ^6)
Mn^{4+}- O^{2-}	1345.15	0.324	0.0
Mn^{3+}-O^{2-}	1267.5	0.324	0.0
Li^{+}-O^{2-}	426.48	0.300	0.0
O^{2-}-O^{2-}	22764.3	0.149	43.0

4.2 Geometry Optimisation of $LiMn_2O_4$ Nanotubes

Geometry optimisation is a vital component in computational studies that are concerned with the structure and the reactivity of molecules. In this section, geometry optimisation results for spinel $LiMn_2O_4$ nanotubes with {100}, {110} and {111} Miller indices with diameter of 5Å are presented. The structures were fully optimised using

DFT energy minimisation technique implemented within CASTEP code, with a cut-off of 600 eV and k-point set 2x1x1. The minimum total energy of the systems was obtained during the optimisation and are listed in Table 9. Spinel $LiMn_2O_4$ nanotube made from {110} was found to have the lowest total energy, suggesting that it is the most stable nanotube for spinel $LiMn_2O_4$ as shown in table 9.

Table 9: Total energy for $LiMn_2O_4$ nanotubes with 5Å diameter.

Miller Index	Energy (eV)
{100}	-9727.396
{110}	-19465.987
{111}	-19461.344

4.3 Spinel $LiMn_2O_4$ Nanotubes with Diameter Ranging From 5Å-11Å

4.3.1 $LiMn_2O_4$ {100} Nanotubes

In this section, different $LiMn_2O_4$ nanotubes with smaller diameter ranging from 5Å-11Å are generated and discussed. Figure 45 shows how nanotubes in figures 46 and 47 were generated at different directions as discussed in section 2.7. Figures 46 and 47 show $LiMn_2O_4$ nanotube generated from {100} surface, wrapped along different directions. Nanotubes shown in figure 46 were wrapped along a_around_b direction while the nanotubes in figure 47 were wrapped along b_around_a direction. For direction a_along_b, nanotubes are found to have their inner layer composed of Mn and O atoms, while the outer layer is composed of Li, Mn and O atoms and this is vice versa for direction b_along_a. Nanotube generated from {100} surface is composed of a varying number of atoms depending on the size of the diameter. Thus, nanotubes with diameter 5Å has 42 atoms while 7Å, 9Å and 11Å are composed of 56, 70 and 84 atoms respectively. The shape of the nanotube changes as the diameter is increased, i.e., nanotube structures become more circular as the diameter is increased.

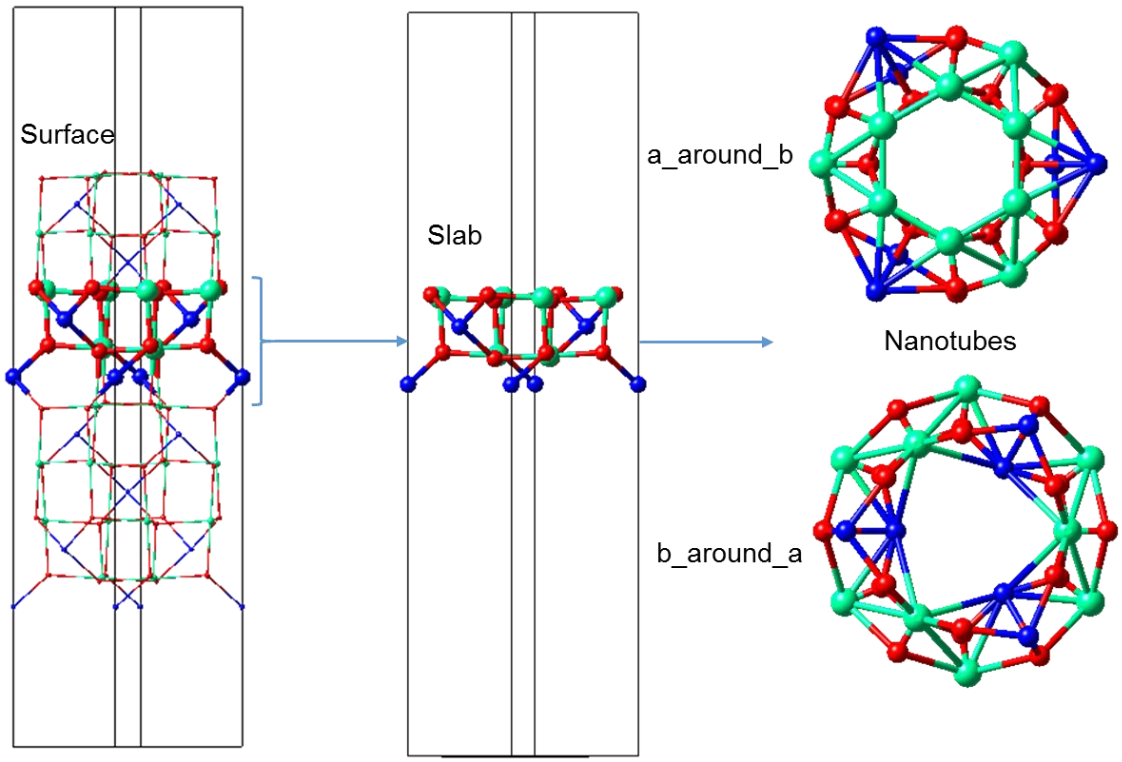

Figure 45: $LiMn_2O_4$ slab of {100} surface.

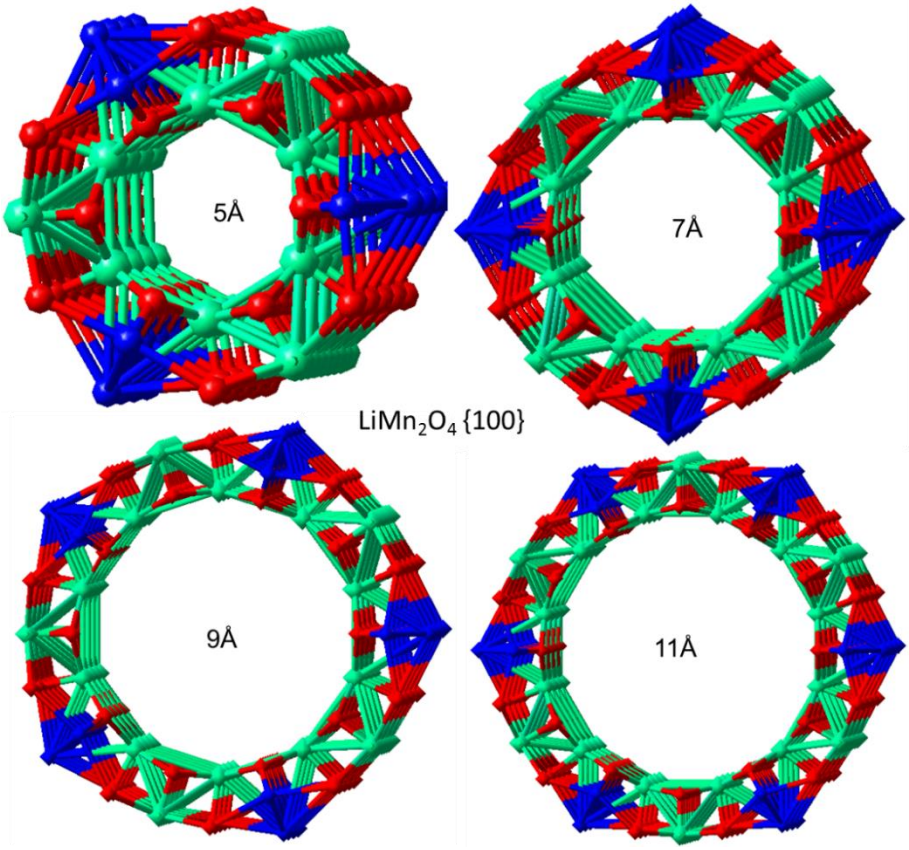

Figure 46: $LiMn_2O_4$ nanotubes created from {100} wrapped along a_around_b.

Figure 47 shows $LiMn_2O_4$ {100} nanotube wrapped along b_around_a direction, as explained previously. All the nanotubes of different diameters have their inner layer composed of Li, O and Mn atoms, while the outer layer is composed of only Mn and O atoms. As the diameter is increased the cross-section area decreases. The final nanotube structures depend on how the sheet is rolled, i.e., the direction of wrapping and they become more spherical with an increase in diameter size.

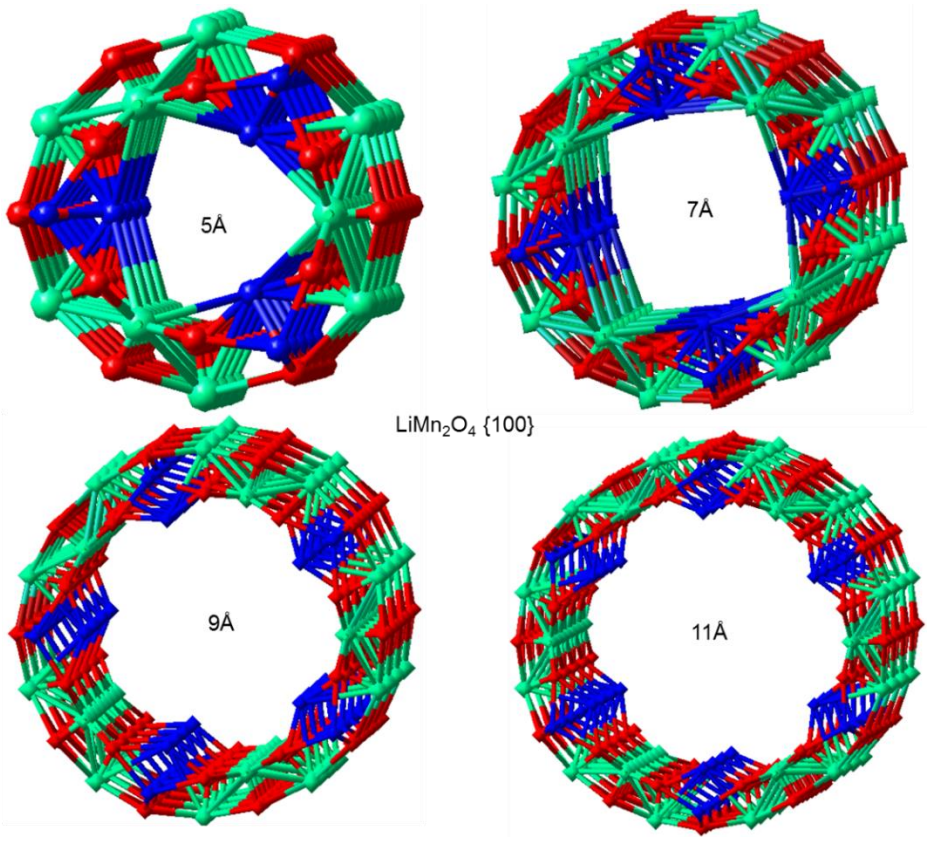

Figure 47: $LiMn_2O_4$ nanotubes created from {100} wrapped along b_around_a.

4.3.2 $LiMn_2O_4$ {110} Nanotubes

Figure 48 shows $LiMn_2O_4$ nanotubes generated from {110} surface with diameter ranging from 5Å-11Å. Nanotube generated from {110} surface is composed of a varying number of atoms relative to the size of the diameter. Thus, nanotubes with diameter 5Å has 42 atoms while 7Å, 9Å and 11Å are composed of 56, 70 and 84 atoms, respectively. The inner layer of all the nanotubes are populated by Mn and O atoms while the outer layer consists of Li, Mn and O atoms. For all the different sizes of the diameter, the inner atoms depict a zigzag configuration. The curvature of the

tubes, however, disturbs the chemistry and causes deviation from the structure based description, especially for small radii nanotubes. As the diameter is increased the shape changes and become more circular which is a favourable shape for nanotube. The nanotubes structures appear to be more closely-packed and denser as the size of the diameter is increased.

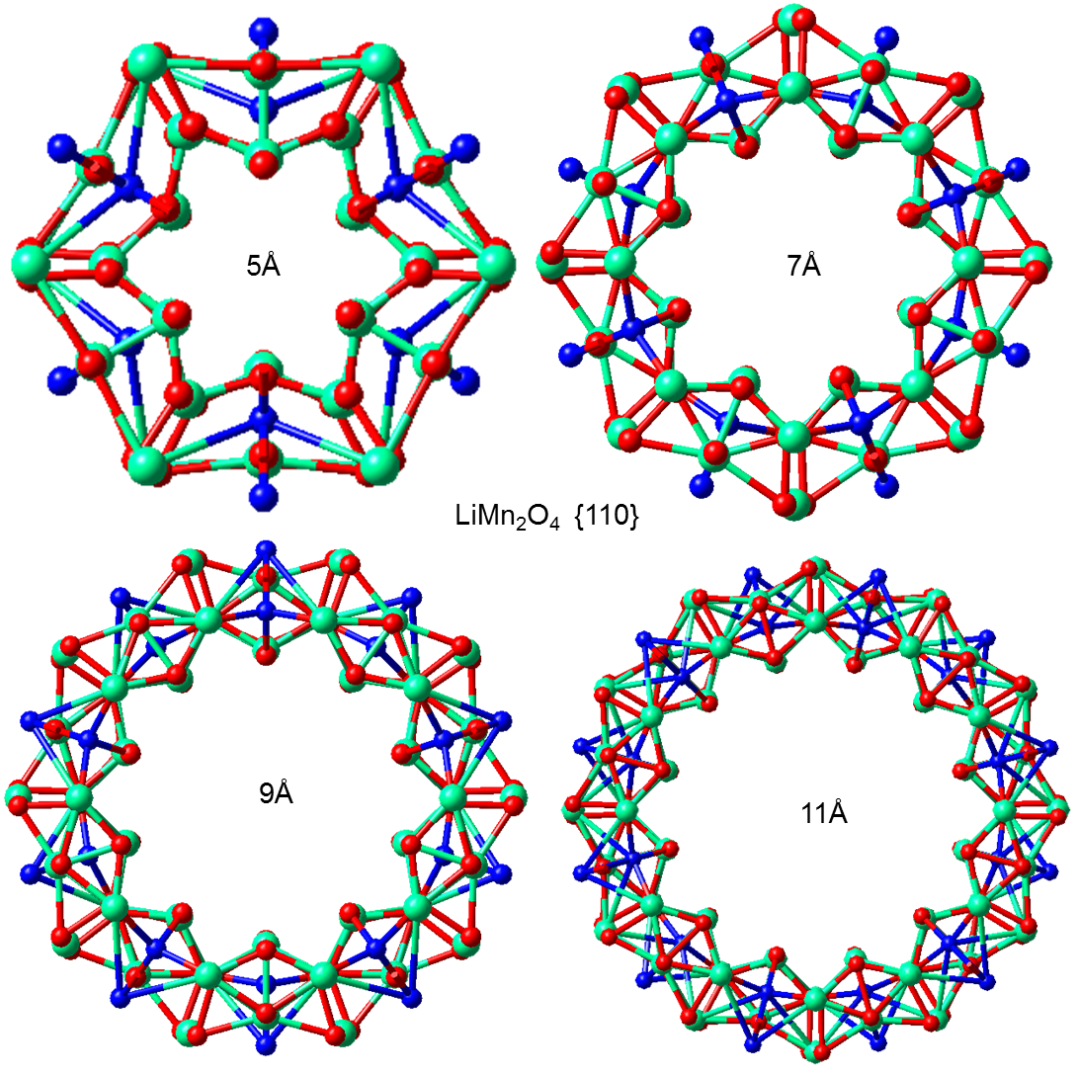

Figure 48: $LiMn_2O_4$ generated from {110} surface.

4.3.3 $LiMn_2O_4$ {111} Nanotubes

Figure 49 depicts $LiMn_2O_4$ nanotubes generated from {111} surface with diameter ranging from 5Å-11Å. Nanotube generated from {111} surface is composed of a varying number of atoms depending on the size of the diameter. Thus, nanotubes with diameter 5Å has 42 atoms while 7Å, 9Å and 11Å are composed of 56, 70 and 84

atoms, respectively. In contrast to the other nanotubes created from other Miller indices, the nanotubes for {111} surface have their inner layer composed of Mn atoms, while the outer layer is composed by Li, Mn and O atoms. The shape of the tube changes as the diameter increases, the tube become more circular. The cross-section area of the tube decreases as the diameter is increased.

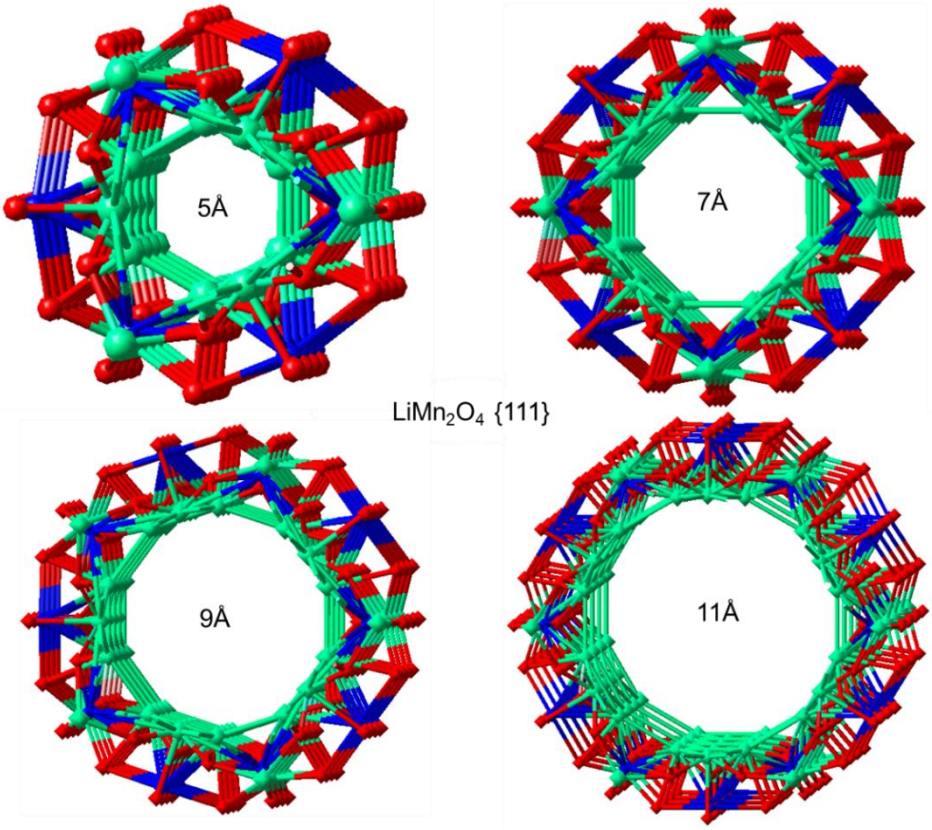

Figure 49: $LiMn_2O_4$ nanotube generated from {111} surface.

The rotational symmetry of a nanotube can be recognised by examining its chiral indices (n,m). A nanotube of indices (n,m) has N-fold rotational symmetry, with N being the greatest common divisor of n and m. When m=0, the nanotube possesses n-fold rotational symmetry and it does not have two-fold rotational symmetry. There are two special non-helical structures that deserve special attention. One is the so-called zigzag and armchair structure as shown in figures 50 and 51 respectively, which has chiral indices of the form (7,7) and (6,6), respectively. Figure 51 shows a view along the axis of symmetry as well as side view for the zigzag arrangement of atoms. As depicted in the picture, the inner most cylinder is composed of Li atoms.

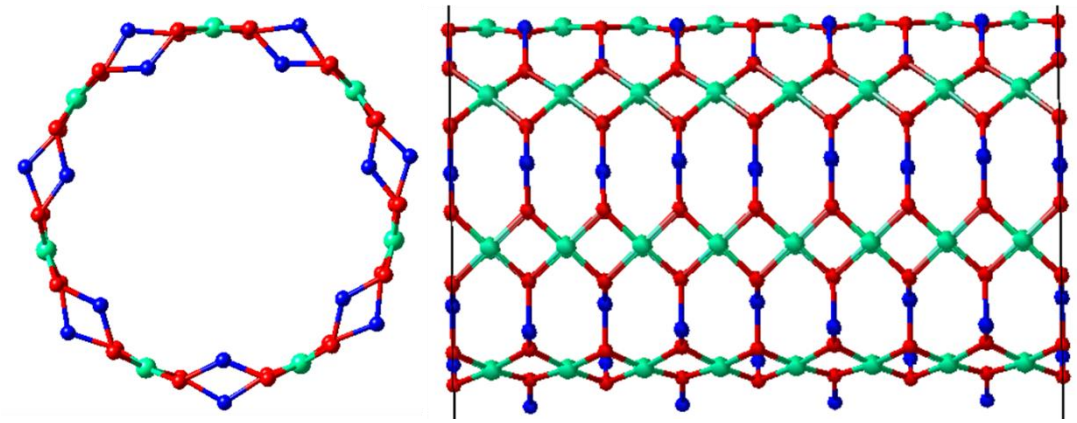

Figure 50: Single-wall $LiMn_2O_4$ nanotube of zigzag chirality obtained by rolling up the {001} surface.

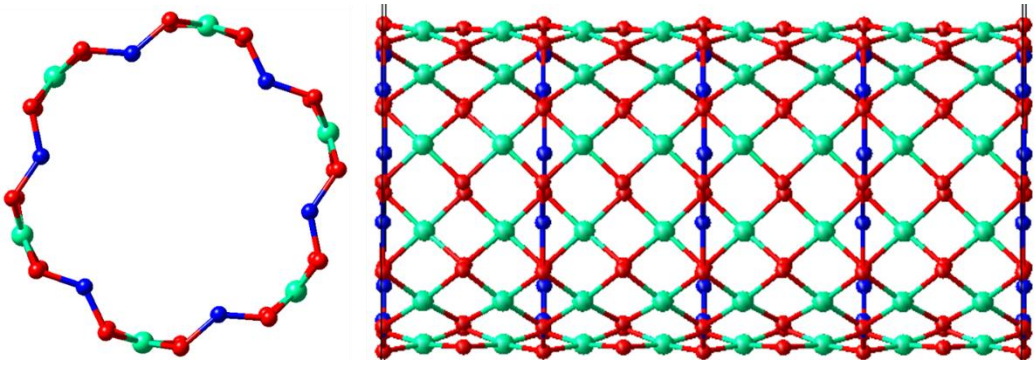

Figure 51: Single-wall $LiMn_2O_4$ nanotube of armchair chirality obtained by rolling up the {001} surface.

4.4 Spinel $LiMn_2O_4$ Nanotubes with Diameter Ranging From 10Å-30Å

4.4.1 $LiMn_2O_4$ {100} Nanotubes

In this section, different $LiMn_2O_4$ nanotubes with larger diameter 15Å-30Å are generated and discussed briefly. Figures 52 and 53 show $LiMn_2O_4$ nanotube generated from {100} surface, wrapped along different directions as shown. Nanotubes shown in figure 52 were wrapped along a_around_b direction, while the nanotubes in figure 53 were wrapped along b_around_a direction. All the nanotubes in figure 52 depict the inner layer to be consisting of Li atoms, while the outer layer is composed of Mn and O atoms. The shape of the tube changes as the size of the diameter is increased as observed with other Miller indices. From the same surface the nanotube was wrapped along a different direction as shown in figure 53, and produced a system with the inner layer composing of single atom, in this case Mn atoms while the outer layer is found to be composed of Li atoms.

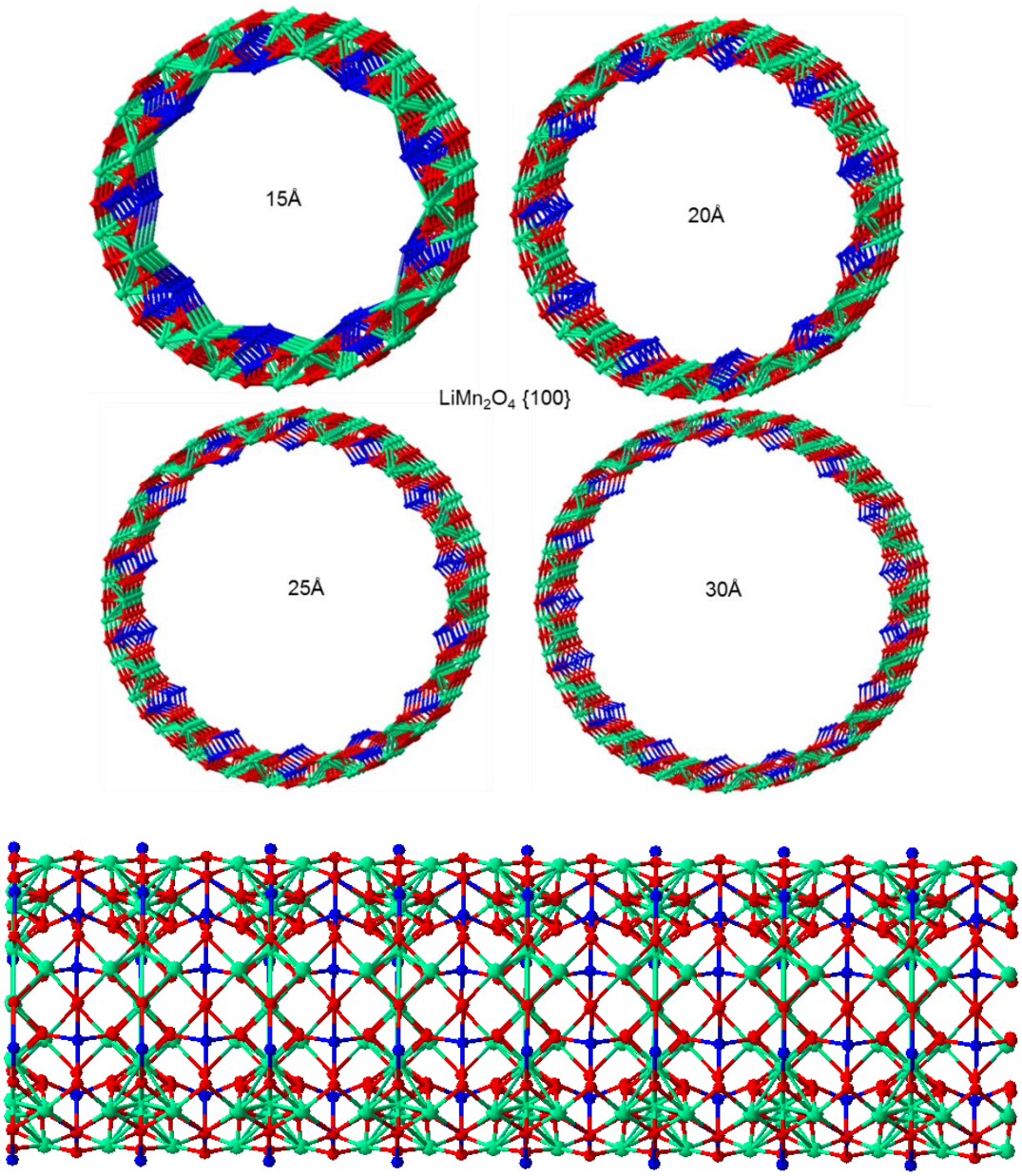

Figure 52: Cross-sectional view and long view of $LiMn_2O_4$ nanotubes generated from {100} surface wrapped along a_around_b.

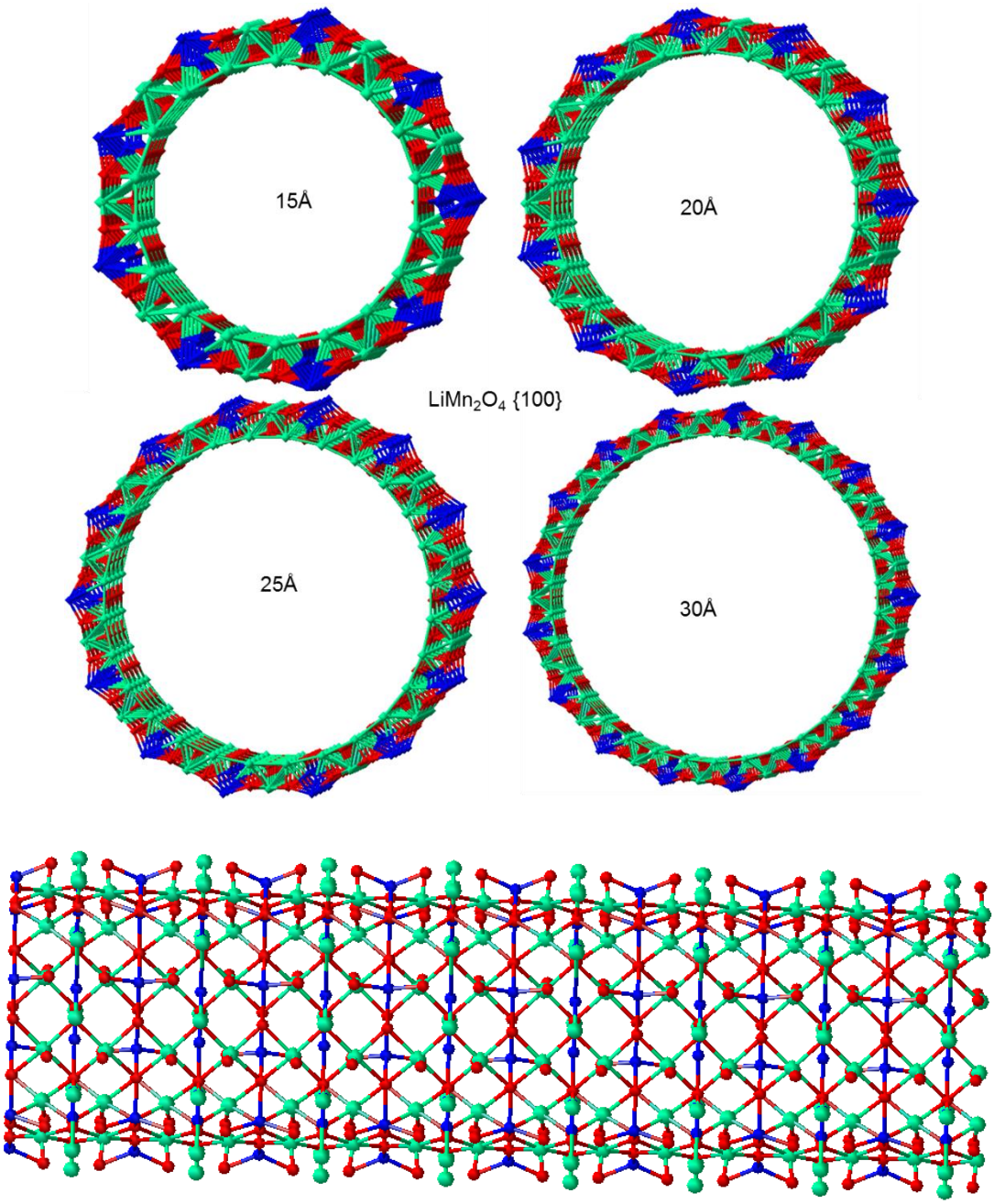

Figure 53: Cross-sectional view and long view of spinel $LiMn_2O_4$ nanotube along {100} surface wrapped along b_around_a.

4.4.2 $LiMn_2O_4$ {110} Nanotubes

Figure 54 depicts $LiMn_2O_4$ nanotubes generated from {110} surface with diameter ranging from 15Å-30Å. Nanotubes generated consist of a varying number of atoms relative to the size of the diameter. The inner most layer of the nanotubes is made up of O and Mn atoms, while the outer layer of the tube is composed of Li, Mn and O

atoms. The nanotubes appear to have formed a defined pattern, i.e., zigzag patterns. Manganese atoms are octahedrally coordinated to oxygen atoms.

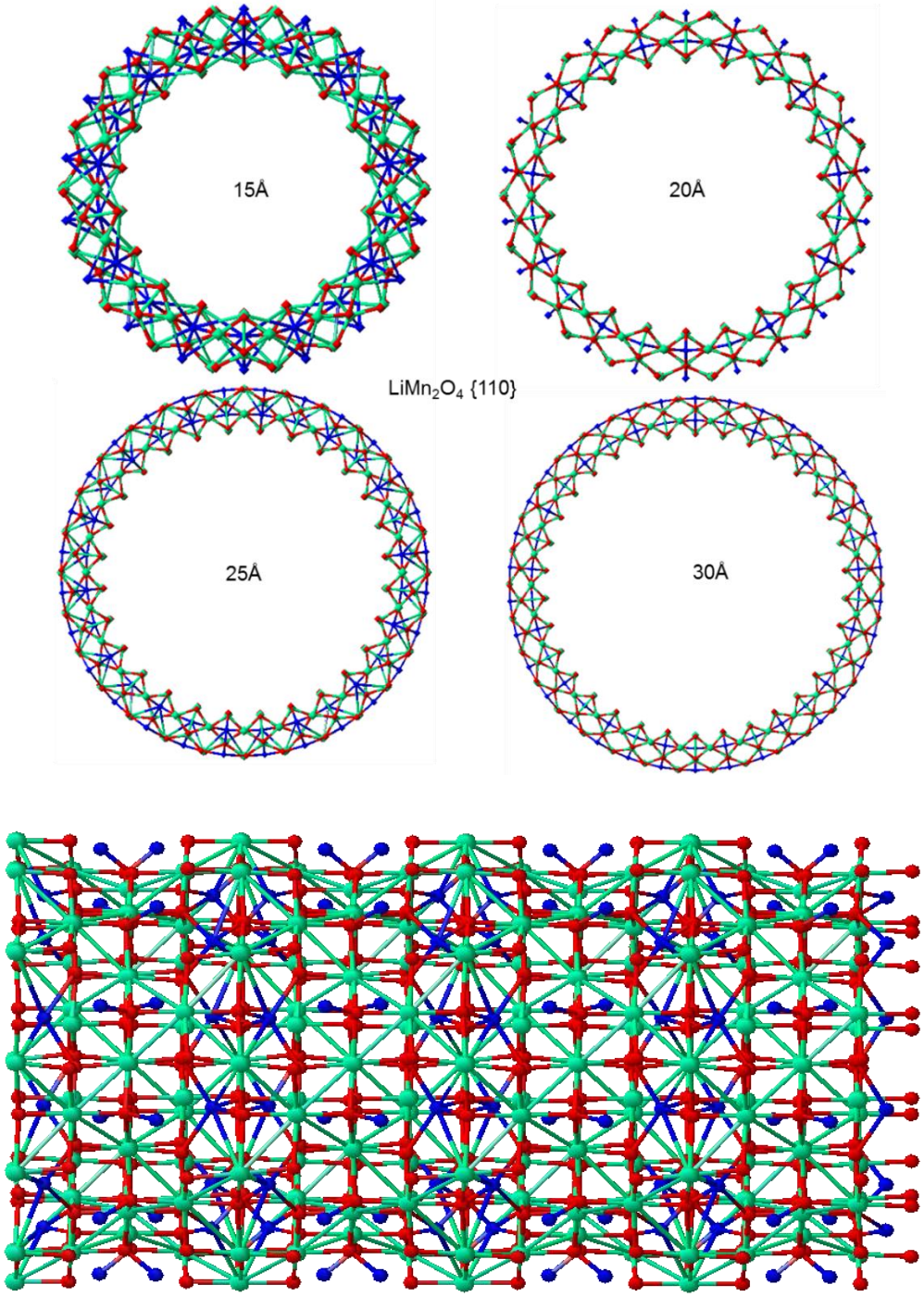

Figure 54: Cross-sectional view and long view of spinel $LiMn_2O_4$ nanotube along {110} surface.

4.4.3 $LiMn_2O_4$ {111} Nanotubes

Figure 55 depicts $LiMn_2O_4$ nanotube structures generated from {111} surface with diameter ranging from 15Å-30Å. Similar trend in terms of number of atoms for different sizes of diameter is noted. The inner layers of the nanotube structures are composed of Mn atoms, while the outer layers is composed of only oxygen atoms. The oxygen atoms on the outer layer can also be clearly identified from the long view of the nanotube structure.

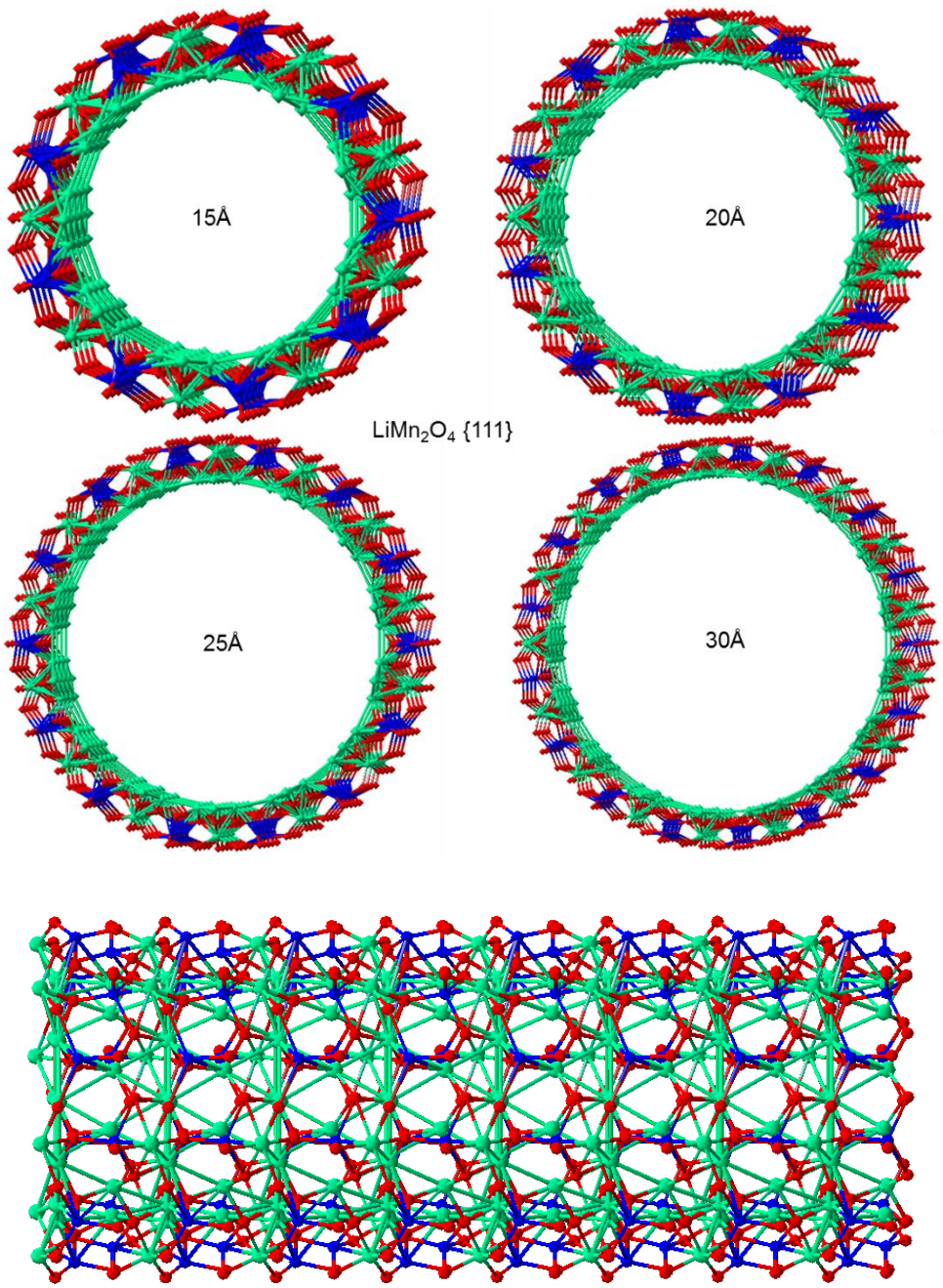

Figure 55: Cross-sectional view and long view of spinel $LiMn_2O_4$ nanotube along {111} surface.

Generally, the atoms in the nanotubes are arranged in a long and hollow cylinder. The structure of nanotube can be examined in terms of primary variables as discussed previously, i.e., length, morphology and size of the diameter. The morphology of nanotubes describes its general structures, including the number of walls as well as its shape. Some application of nanotubes, such as those attempting to use nanotubes as reinforcing element in composite materials or as continuous electrical conductor require nanotubes of well controlled and often extended length. Figures 56 and 57 shows the cross-sectional and the wall of spinel $LiMn_2O_4$ nanotube generated from {100} and {111} surfaces, respectively. The wall of nanotube generated from {111} surface is more complex than the wall of nanotube generated from {100} surface. This proves that the morphology of the nanotube depends on the Miller index from which the surface was cut. Consequently, {100} surface generated a single wall nanotube while the surface {111} generated a multi-wall $LiMn_2O_4$ nanotube. This is depicted in figures (b), where {111} nanotube appears to be more dense compared to {100} nanotube.

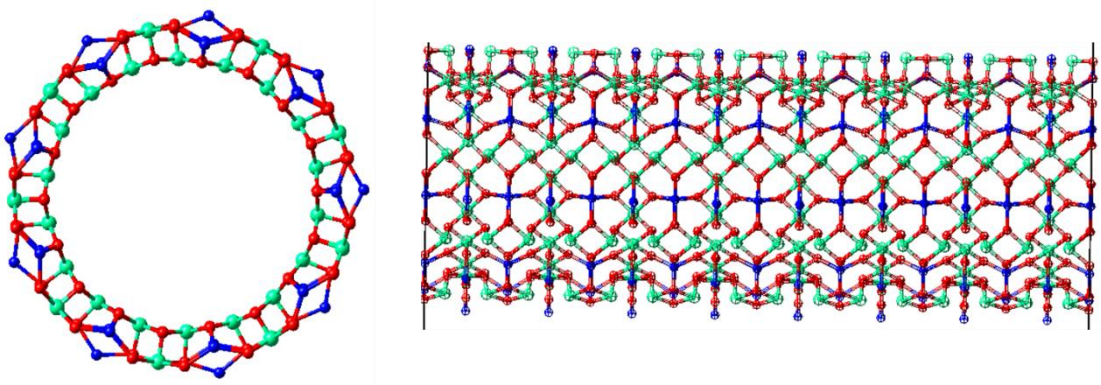

(a) (b)

Figure 56: Spinel $LiMn_2O_4$ nanotubes made from {100} surface with diameter of 11Å, (a) shows the cross section of the nanotube and (b) shows the nanotube wall.

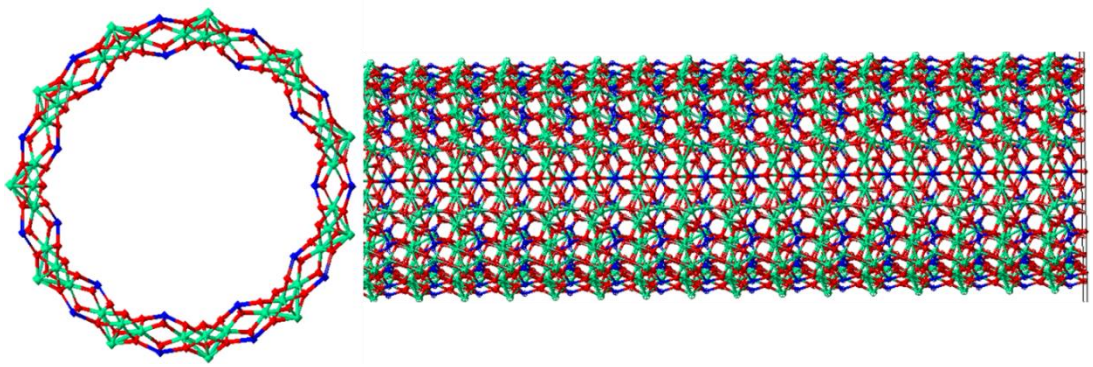

(a) (b)

Figure 57: Spinel $LiMn_2O_4$ nanotubes made from {111} surface with diameter of 20Å, (a) shows the cross-section of the nanotube and (b) shows the nanotube wall.

4.5. Bond Length of Spinel $LiMn_2O_4$ Nanotubes

4.5.1 $LiMn_2O_4$ {100} Nanotube Bond Length

In molecular geometry bond length is the average distance between two nearest bonded atoms in a system. Previous studies showed that a change in diameter of the nanotubes affects the average bond length of the nanotube. As the diameter is increased the average bond distance is stretched or compressed depending the amount of applied strain. In this section average bond length of $LiMn_2O_4$ {100} nanotube with diameter ranging from 5Å-11Å are presented. Figure 58 shows the average bond lengths of $LiMn_2O_4$ nanotubes with diameter of 5Å and 7Å. For the 5Å nanotube, the outer average bond length of Mn-O and Li-O atoms are equal to 2.14Å and 2.71Å, respectively, while the inner layer is composed of only Mn-O atoms and the average bond distance is 2.15Å. The structures have the bond length that is perpendicular to the tube axis and the average bond distance between Li-Li atoms is 3.13Å for 5Å. For 7Å the outer average bond lengths equal 2.15Å and 3.46Å Mn-O and Li-O, respectively, while the inner average bond length equal to 2.15Å. The average length that is perpendicular to the tube is equal to 3.15Å. The results show that when the diameter of the tube is increased the average bond for Li-O pair is decreased. The outer average bond length between Mn-O increases while the inner average bond length decreases.

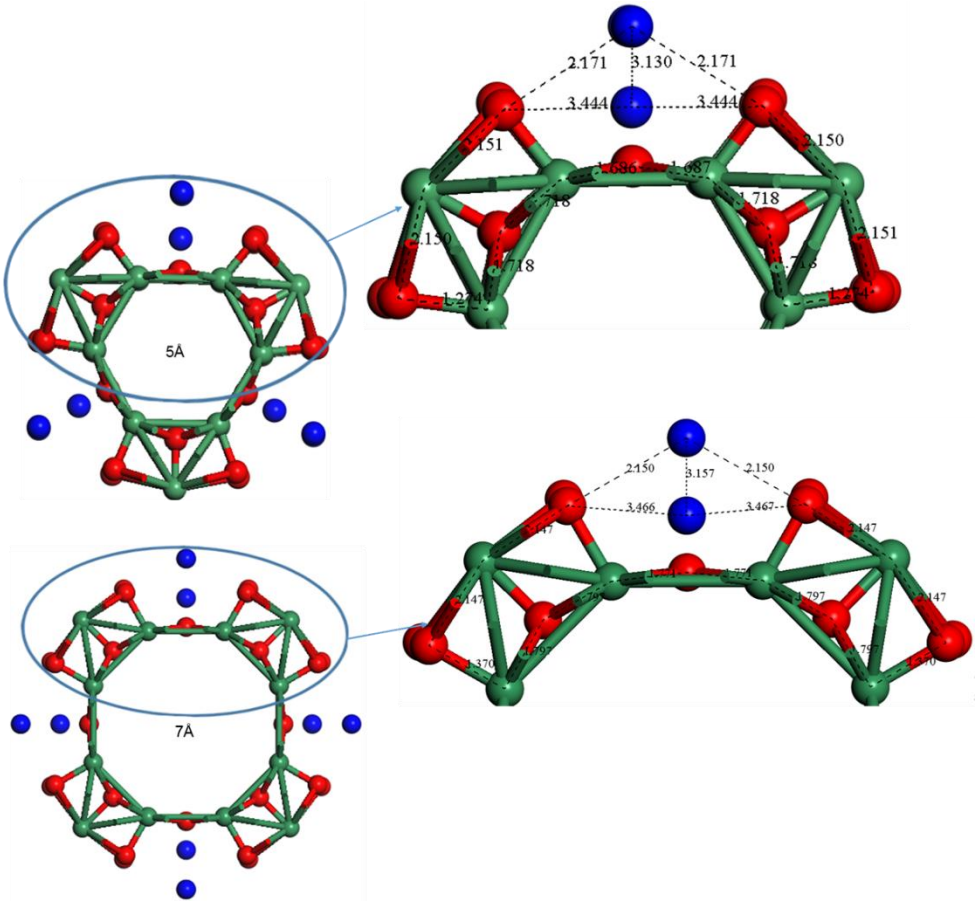

Figure 58: Bond length of {100} $LiMn_2O_4$ nanotube with diameter of 5Å and 7Å.

Figure 59 shows the average bond length of $LiMn_2O_4$ nanotubes with diameter of 9Å and 11Å. For 9Å nanotube the average bond lengths between Mn-O, Li-O and Li-Li in the outer layer equal to 2.25Å, 2.31Å and 3.19Å, respectively. The average bond length between Mn-O on the inner layer is 1.96Å, slightly higher than the Mn-O bond length for the bulk structure. As the diameter is increased to 11Å, the average bond lengths for Mn-O, Li-O outer layer and Mn-O inner layer is compressed and equal to 2.13Å, 2.12Å and 1.88Å, respectively, while the average bond length between Li-Li stretches to 3.21Å. The Mn-O average bond length for inner layer decrease as the diameter increases for {100} spinel $LiMn_2O_4$ nanotube. Also the bond length between the nearest atoms in the outer layer decrease as the diameter is increased. Only the Li-Li average bond length and is perpendicular to the tube increase as the diameter is increased.

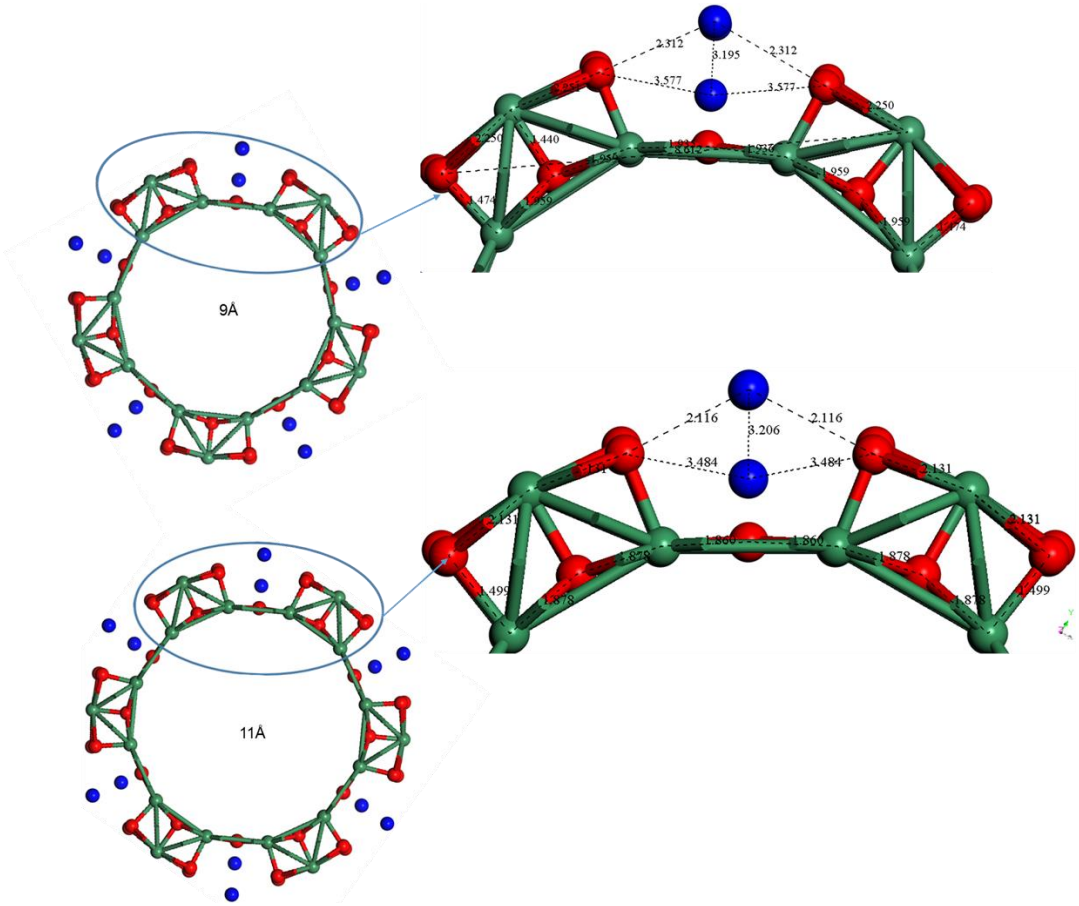

Figure 59: Bond length of {100} $LiMn_2O_4$ nanotube with diameter of 9Å and 11Å.

4.5.2 $LiMn_2O_4$ {110} Nanotube Bond Length

In this section, average bond lengths of {110} $LiMn_2O_4$ nanotube with diameter ranging from 5Å-11Å are calculated and presented in figures 60 and 61. The results are not following any trend, in some cases the bond length is increasing while in others is decreasing depending on the internal and external morphology of the nanotube. The inner layers for 5Å and 7Å nanotubes consist of Mn and O atoms while the outer layers consist of Li, Mn and O atoms. The Mn-O average bond lengths for 5Å and 7Å nanotubes equal to 1.55Å and 1.72Å, respectively. As the diameter is increased the Mn-O average bond length increases. This nanotube has the bond length that is perpendicular to the tube axis and the average bond distance between Mn-Mn atoms is 1.77Å for 5Å, while for 7Å nanotube Mn-Mn equal to 1.89Å increased as diameter increases.

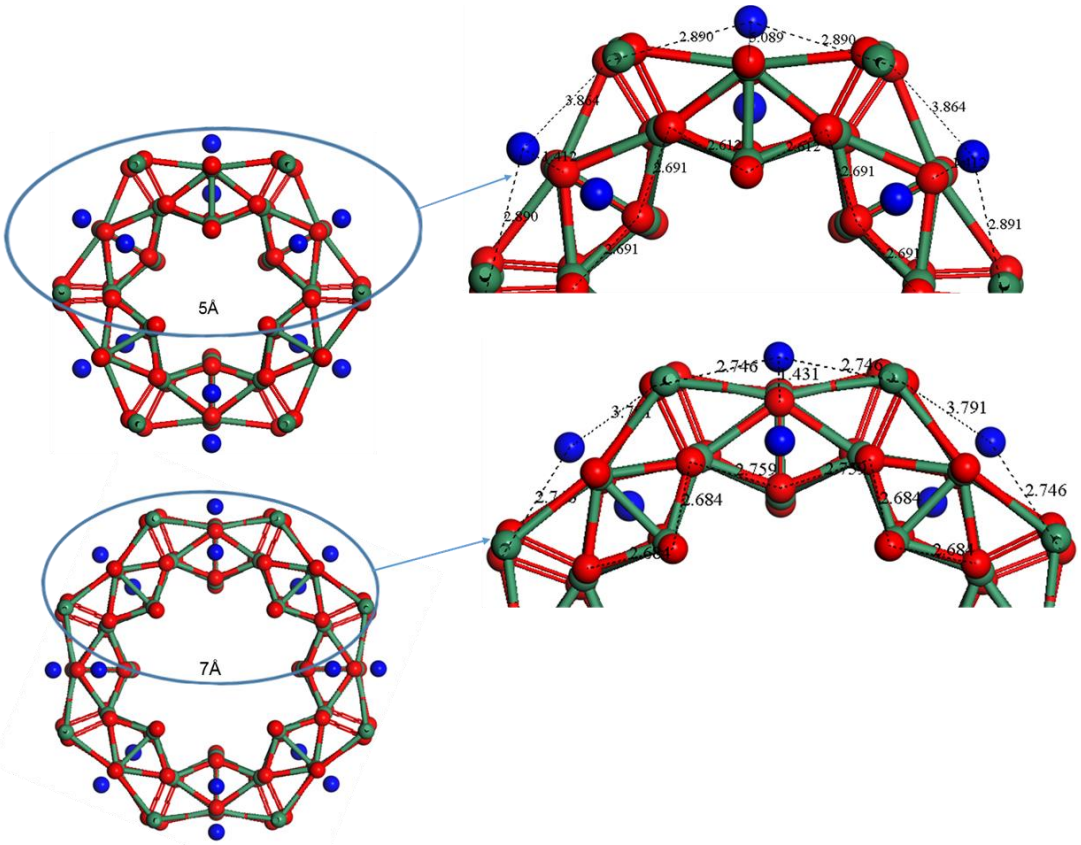

Figure 60: Bond length of {110} $LiMn_2O_4$ nanotube with diameter of 5Å and 7Å.

Figure 61 shows the average bond lengths of $LiMn_2O_4$ nanotube with diameter of 9Å and 11Å. The inner layers composed of Mn and O atoms and the Mn-O average bond length for 9Å nanotube equals to 1.89Å while for 11Å nanotube Mn-O equal to 1.9Å. For this nanotubes Mn-O average bond length increases as the diameter is increased. The outer layer of this nanotubes composed of Li, Mn and O atoms. The average bond lengths between the two nearest atoms for 9Å and 11 nanotubes increase as the diameter increases and are listed in table 10. The findings reveal that values for the average bond length depend on the strain applied to the system when size of the diameter of the nanotube is changed. This suggests that when the diameter is increased the average bond length of the nearest neighbouring atom is stretched.

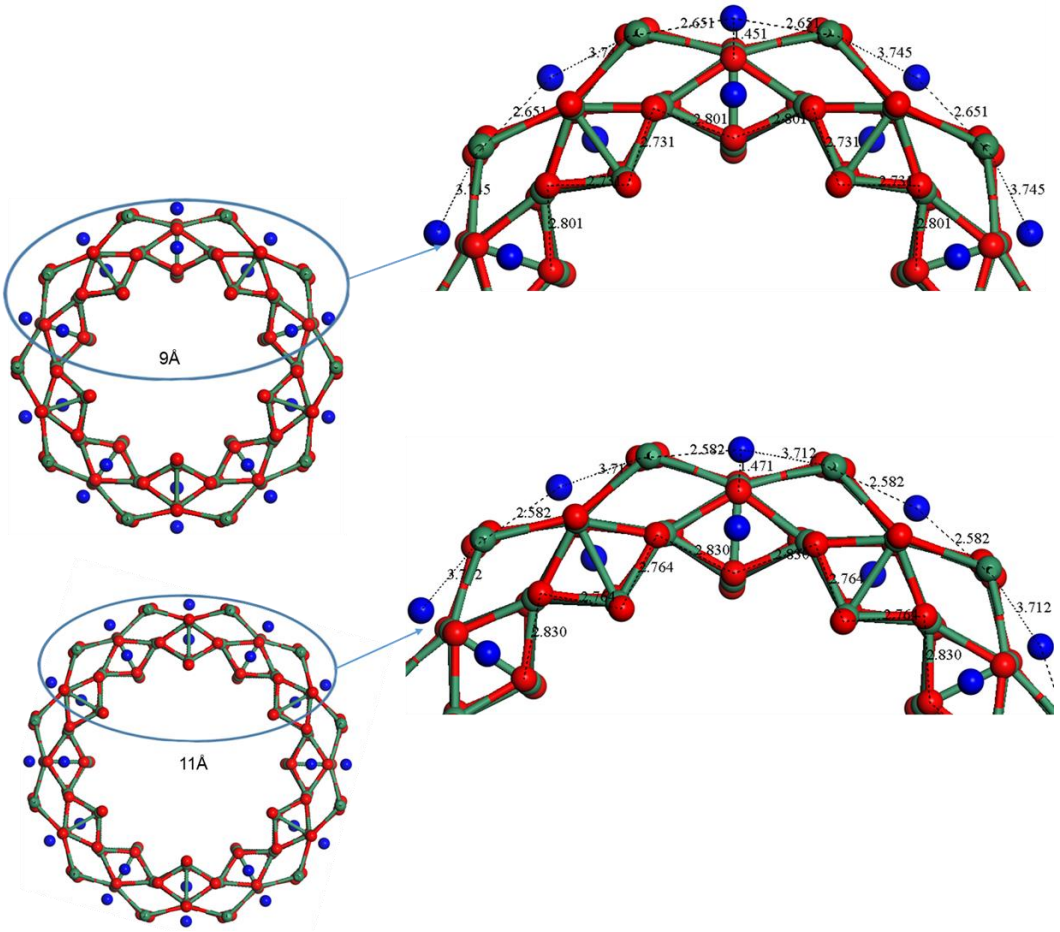

Figure 61: Bond length of {110} $LiMn_2O_4$ nanotube with diameter of 9Å and 11Å.

4.5.3 $LiMn_2O_4$ {111} Nanotube Bond Length

Another important aspect on measuring the bond lengths of the nanotubes is that due to the curvature of the nanotube sidewalls, the bond lengths are different from those of the counterpart bulk system. Moreover, nanotube structures are stronger due to the curvature of the tube, which induces changes in distributions of localised and delocalised electronic state of the nanotubes. Figure 62 shows the average bond lengths of $LiMn_2O_4$ nanotubes with diameter of 5Å and 7Å. All the inners layers of this nanotubes consist of Mn-Mn atoms, while the outer layers consist of Li and O atoms. For both 5Å and 7Å nanotubes the Mn-Mn average bond length was equal to 2.00Å and 2.29Å, respectively. The Mn-O average bond length for 5Å nanotube equals 1.67Å while for 7Å nanotube equals to 1.75Å. The Li-O average bond length for 5Å equals to 2.49Å, as the diameter was increased to 7Å the Li-O average bond length decreased to 2.43Å.

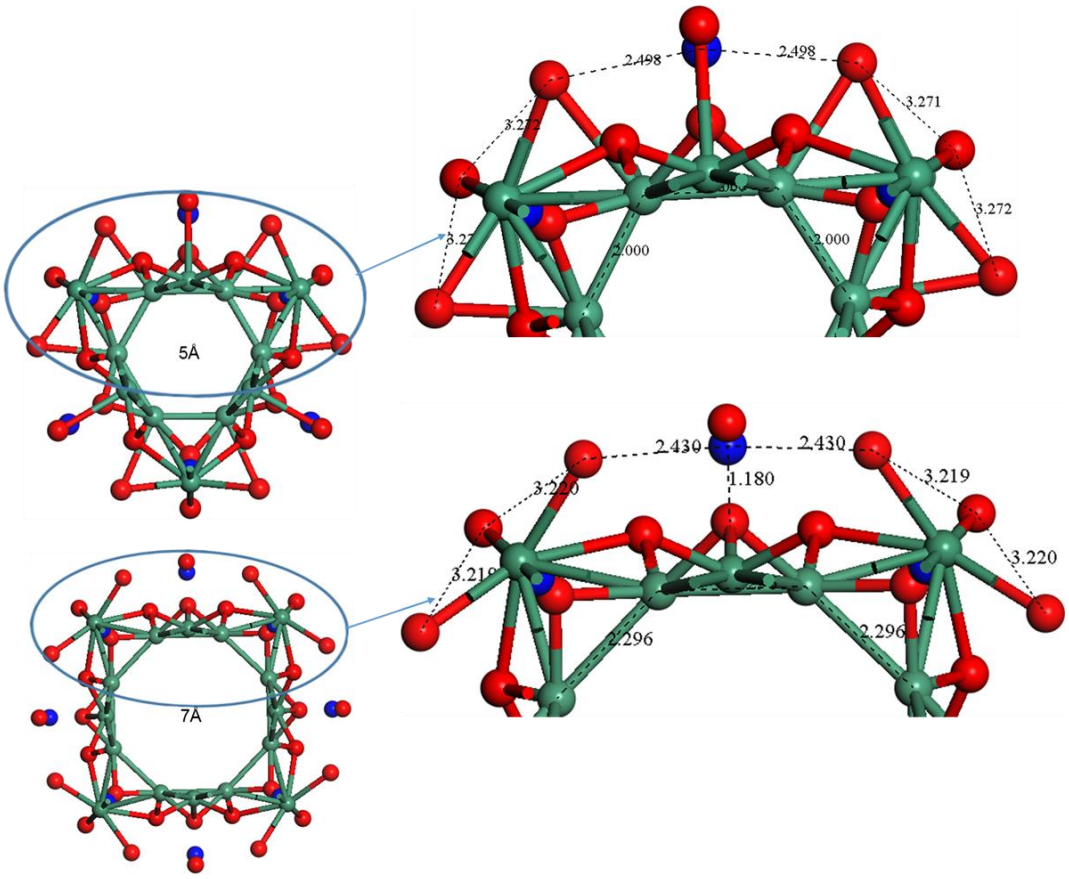

Figure 62: Bond length of {111} $LiMn_2O_4$ nanotube with diameter of 5Å and 7Å.

Figure 63 shows the average bond lengths of $LiMn_2O_4$ nanotube with diameter of 9Å and 11Å. The inner layers of this nanotubes consist of Mn-Mn atoms. The Mn-Mn average bond length for 9Å nanotube equals to 2.47Å while for 11Å nanotube equals to 2.85Å. The bond distance between the Mn-O nearest atoms for 9Å is nanotube equal to 1.81Å, while for 11Å nanotube the Mn-O average bond distance is equal to 1.94Å. The findings reveal that the values for the average bond length are increasing as the size of the diameter is increased. This suggests that when the diameter is increased both the inner and outer layers are stretched in case of this nanotube. Also the shape of the nanotube changes as the diameter is varied as shown in figure 63. Table 10 gives a comprehensive list of average bond distance for various $LiMn_2O_4$ nanotubes and bulk structure. For {100}, {110} and {111} surfaces; the average bond lengths of Mn-O and Mn-Mn increase with the increase in diameter. For {110} Li-O average bond length decreases as the diameter increase while for the other surfaces is fluctuating. There is no trend for O-O interaction as the diameter of the nanotube increase for all surfaces, as shown in table 10.

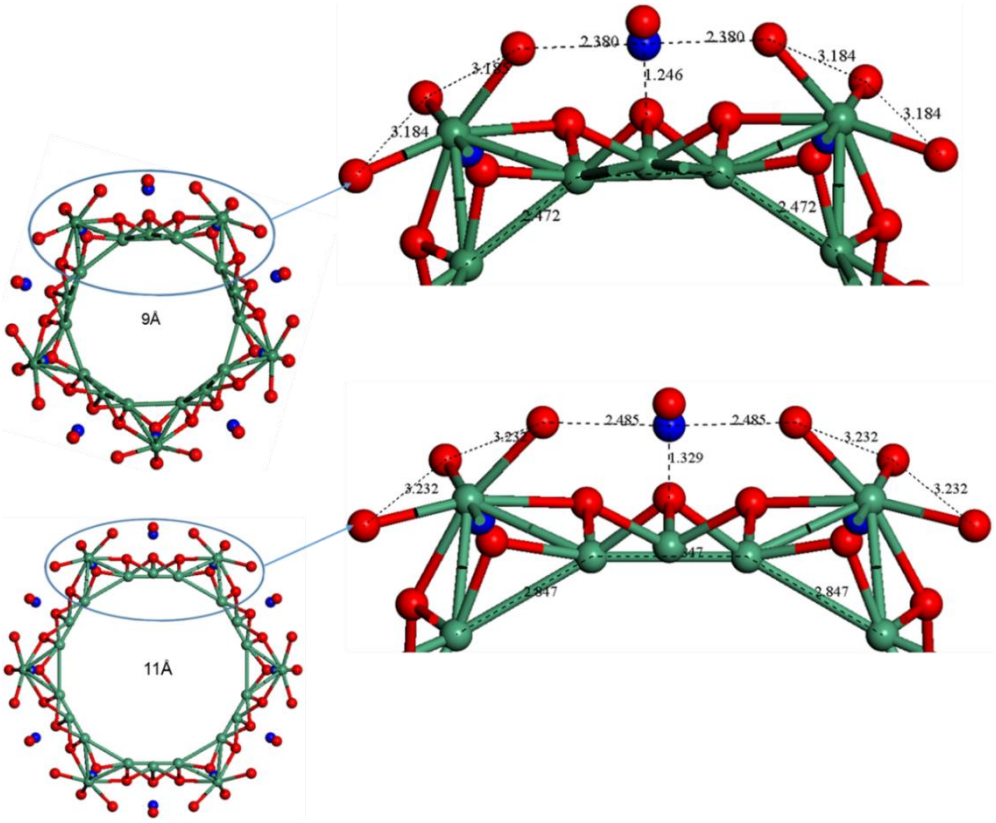

Figure 63: Bond length of {111} $LiMn_2O_4$ nanotube with diameter of 9Å and 11Å.

Table 10: Average bond lengths for various spinel $LiMn_2O_4$ nanotubes.

Bulk Structure		Mn-O(Å)	O-O(Å)	Mn-Mn(Å)	Li-O(Å)
		1.96	3.21	2.91	1.96
Miller Index	Diameter	Mn-O(Å)	O-O(Å)	Mn-Mn(Å)	Li-O(Å)
{100}	5	1.72	2.39	2.10	2.17
	7	1.79	2.51	2.37	2.15
	9	1.93	2.72	2.84	2.32
	11	1.89	2.64	2.64	2.12
{110}	5	1.55	2.61	1.77	2.89
	7	1.72	2.76	1.89	2.75
	9	1.89	2.73	1.99	2.65
	11	1.91	2.76	2.07	2.58
{111}	5	1.67	2.56	2.00	2.49
	7	1.75	2.68	2.29	2.43
	9	1.81	2.74	2.47	2.38
	11	1.94	3.01	2.85	2.49

4.6 Lattice Parameters for Spinel $LiMn_2O_4$ Nanotubes

Lattices in three dimensions generally have three lattice constants referred to as *a*, *b*, and *c*. Table 11-13 show calculated lattice parameters for $LiMn_2O_4$ nanotube structures with varying Miller indices and size of the diameter, ranging from 5Å-30Å. As expected for a nanotube structure, the morphology is elongated along the *a* lattice parameter. The lattice parameter *a* increases with an increasing size of the diameter while the lattice parameter *c* remain constant. The trend is observed for all three Miller indices investigated.

Table 11: Lattice parameters for $LiMn_2O_4$ nanotube along {100} surface.

Index	Diameter (Å)	Cell Parameters (Å)
{100}	5	a=19.597,c=5.825
{100}	7	a=21.865,c=5.825
{100}	9	a=24.063,c=5.825
{100}	11	a=26.215,c=5.825
{100}	15	a=30.435,c=5.825
{100}	20	a=35.616,c=5.825
{100}	25	a=40.739,c=5.825
{100}	30	a=45.825,c=5.825

Table 12: Lattice parameters for $LiMn_2O_4$ nanotube along {110} surface.

Index	Diameter (Å)	Cell Parameters (Å)
{110}	5	a=21.127,c=8.238
{110}	7	a=23.490,c=8.238
{110}	9	a=25.772,c=8.238
{110}	11	a=27.998,c=8.236
{110}	15	a=32.337,c=8.238
{110}	20	a=37.630,c=8.238
{110}	25	a=42.836,c=8.238
{110}	30	a=47.990,c=8.238

Table 13: Lattice parameters for $LiMn_2O_4$ nanotube along {111} surface.

Index	Diameter (Å)	Cell Parameters (Å)
{111}	5	a=20.249,c=5.045
{111}	7	a=22.560,c=5.045
{111}	9	a=24.795,c=5.045
{111}	11	a=26.979,c=5.045
{111}	15	a=31.249,c=5.045
{111}	20	a=36.477,c=5.045
{111}	25	a=41.634,c=5.045
{111}	30	a=46.749,c=5.045

4.7 Radial Distribution Functions for Spinel {111} $LiMn_2O_4$ Nanotube

In RDFs the number of peaks appearing indicate that the atoms are packed around each other in a shell of neighbours. The occurrence of peaks at long range has a high degree of ordering. Usually, at high temperature the peaks are broad, indicating thermal motion while at low temperature they are sharp. They are particularly sharp in the crystalline materials, where atoms are strongly confined in their positions. In this section, the radial distribution functions at different temperatures for $LiMn_2O_4$ nanotube structure are given in figure 64-66. The graphs show the radial distribution functions for Li-Li, Mn-Mn, Mn-O, O-Li, O(s)-Li, Mn-O(s), O(s)-O, O(s)-O(s) and O-O pairs at temperature of 300K, 1500K and 2900K for {111} nanotube. The (s) represents the interactions based on shell model. The peaks occur almost at the same distances irrespective of the temperature. At 300K, for Mn-O separation the first peak occurs at 1.86Å with g(r) = 37.79. The first highest peak for Mn-Mn separation occurs at approximately 2.81Å with g(r) = 11.45. For O-Li separation the highest peak is at approximately at 1.68A with g(r) = 12.33. Interestingly, Li-Li separation depicts the first highest peak with double peaks occurring at 2.45Å and g(r) = 3.14 and second highest broad peak occurs at 5.83Å and g(r) = 3.33. Furthermore, the Li-Li double peak collapses into a single at higher temperatures (see 1500K and 2900K). At lower temperatures, the systems appear to be ordered.

The calculated RDFs are not as sharp as those of the bulk system because the atoms are not confined to their positions and also, the large surface area of the nanotubes.

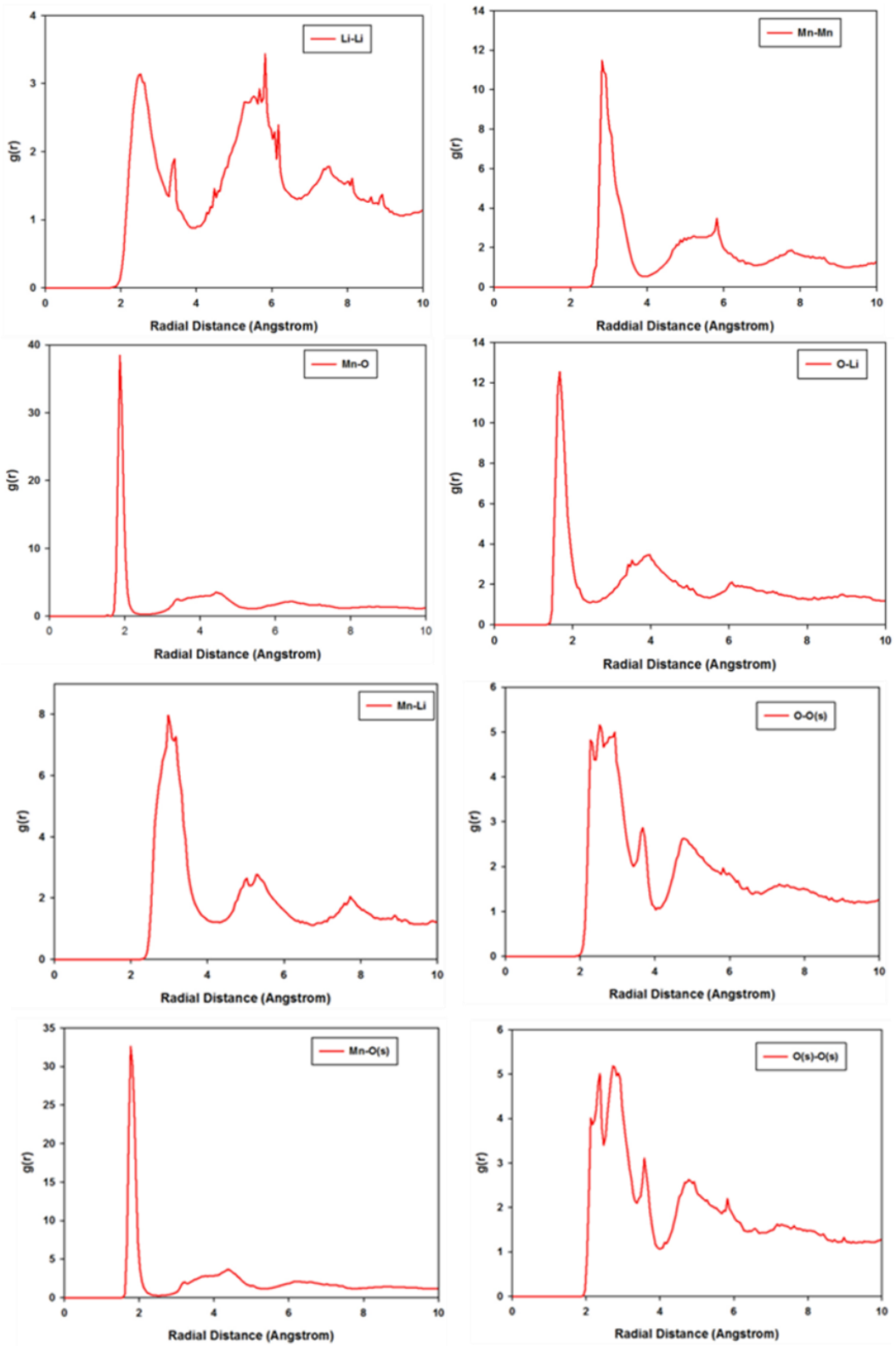

Figure 64: Radial distribution functions for spinel $LiMn_2O_4$ {111} nanotube at 300K.

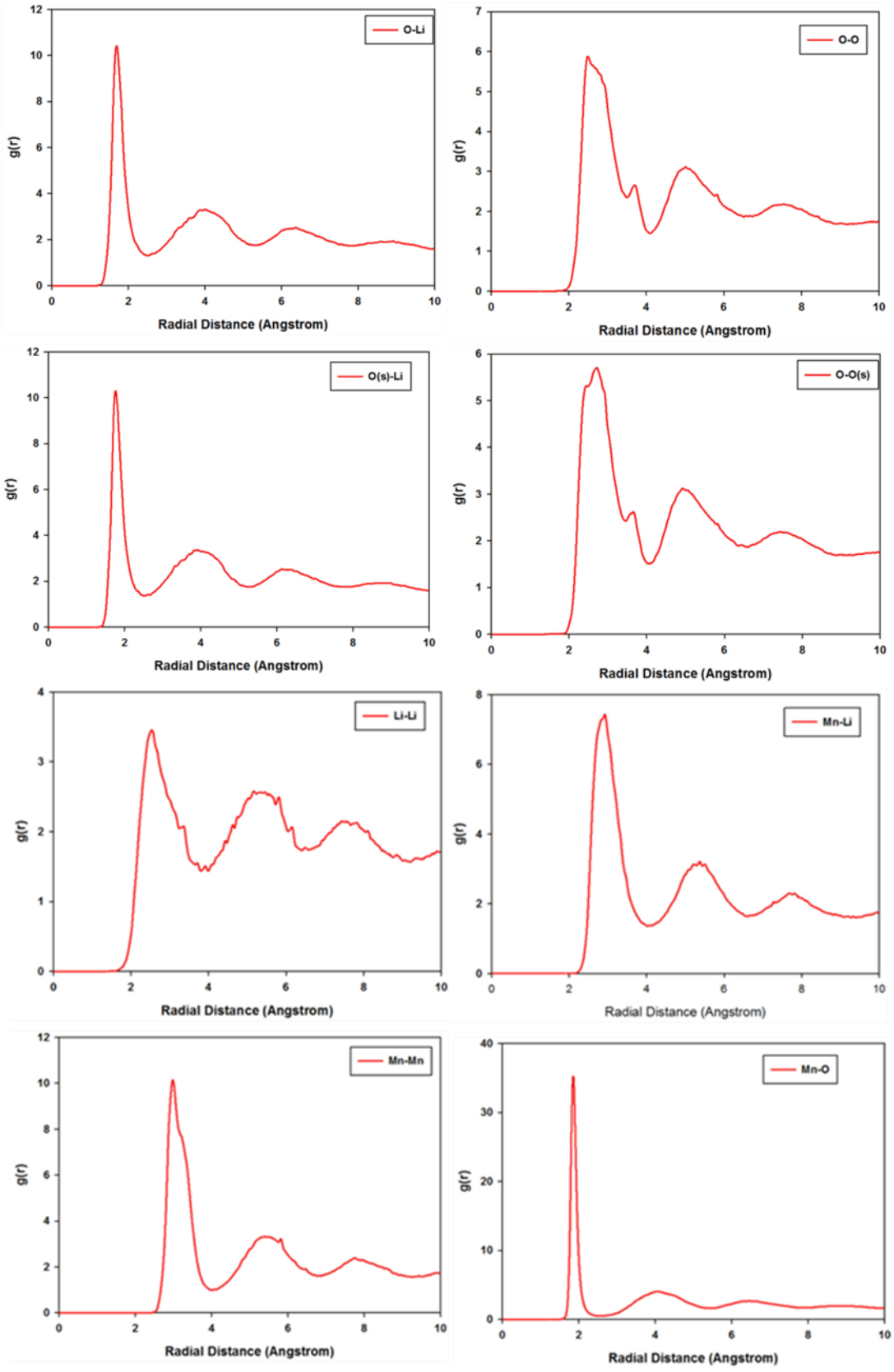

Figure 65: Radial distribution functions for spinel $LiMn_2O_4$ {111} nanotube at 1500K.

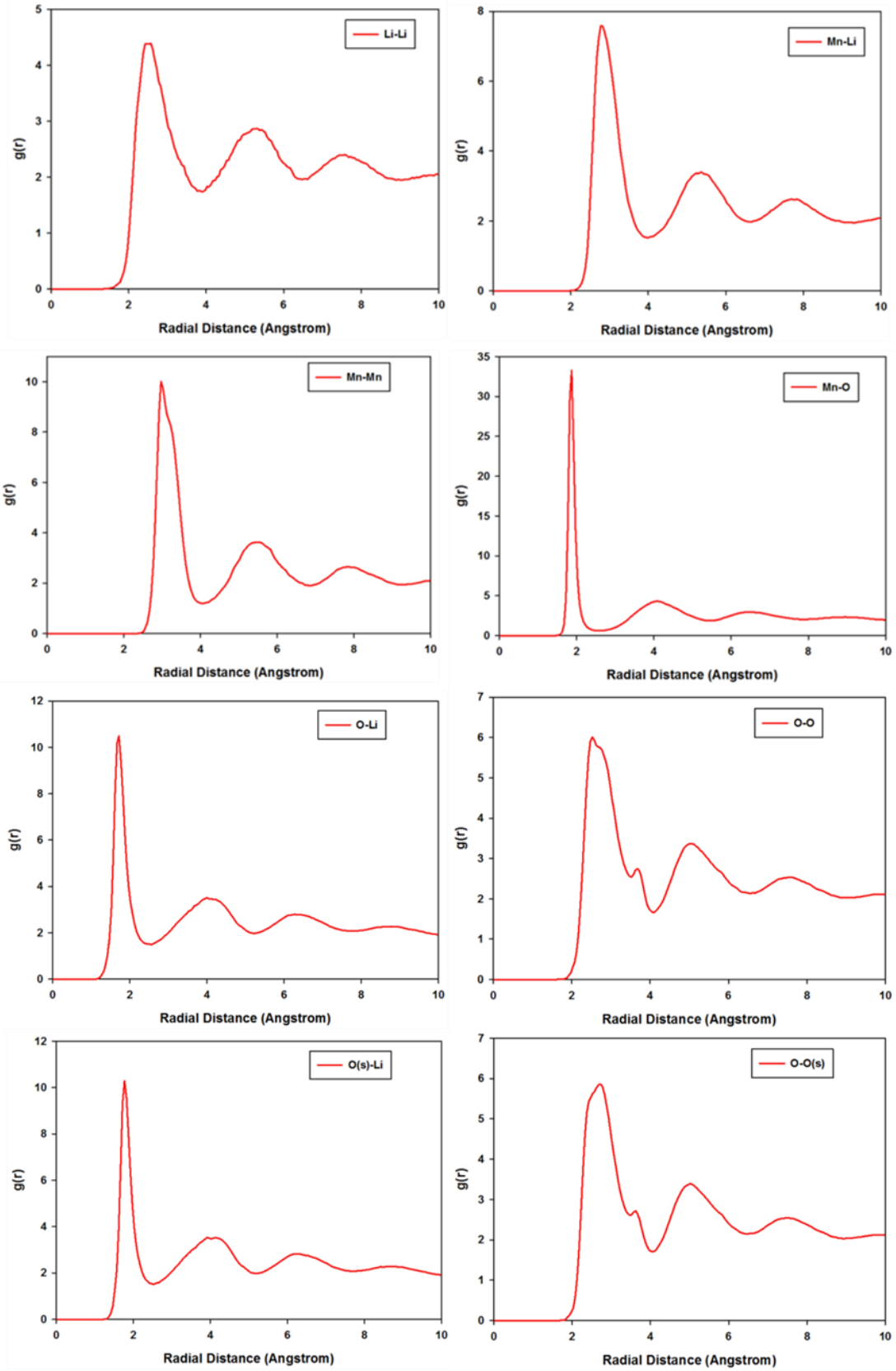

Figure 66: Radial distribution functions for spinel $LiMn_2O_4$ {111} nanotube at 2900K.

Figure 67 shows the RDFs for selected pair interaction as discussed in the section above. It is revealed that as the temperature is increased the peaks become broader and the value of g(r) decreases. The peak broadening is associated with greater degree of disorder within the systems at higher temperatures. For Li-Li interaction the double peaks collapse into single peaks as the temperature is increased.

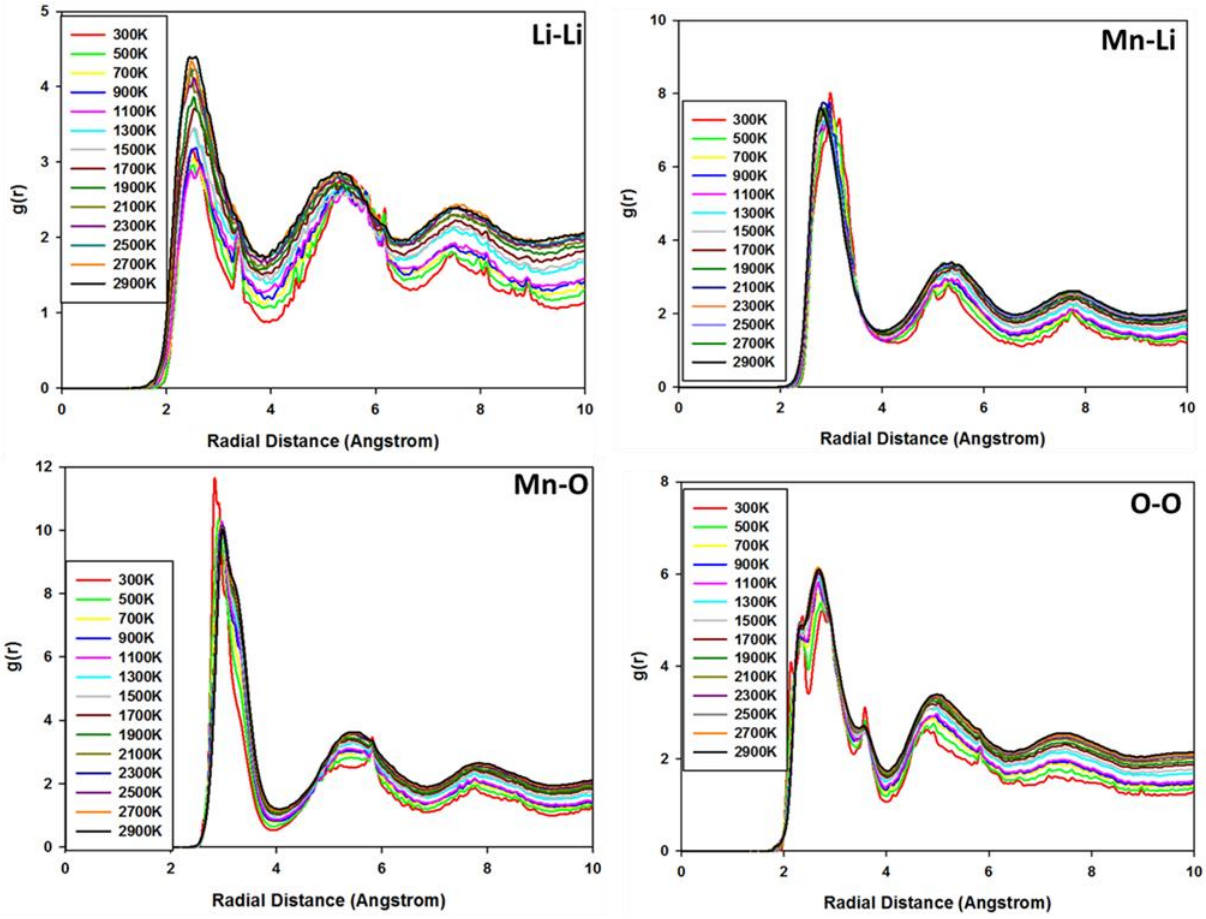

Figure 67: Graphs of g(r) and radial distance showing the partial radial distribution function of Li-Li, Mn-O, O-O and Mn-Li pairs at various temperatures.

Figure 68 shows the graph of total energy versus temperature and reveals a linear dependence curve. The total energy of spinel $LiMn_2O_4$ nanotube increases with an increase in temperature. There is a transition at an approximately 2000K, where the linear dependence discontinues.

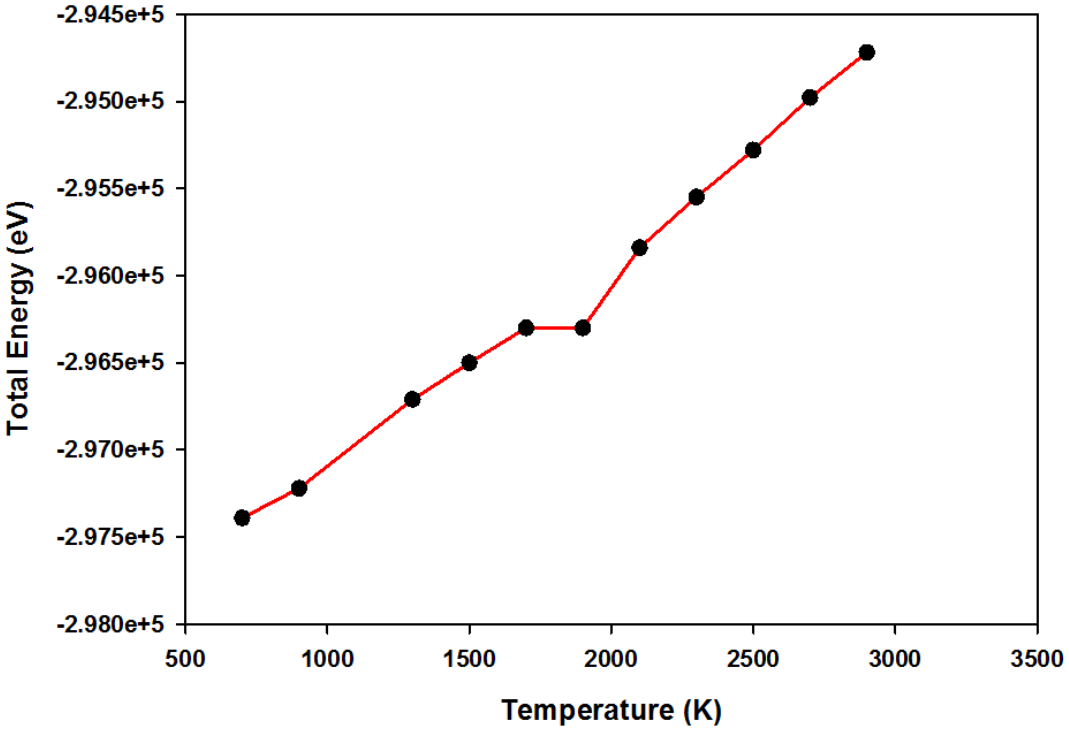

Figure 68: Graph for total energy versus temperature for {111} $LiMn_2O_4$ nanotube.

4.8 XRD Patterns for Spinel $LiMn_2O_4$ Nanotubes

The ease of XRD technique makes its application to the microstructure of nanomaterial a favourable choice. When studying nanostructures using XRD technique, the crystallite size is usually the sole factor of interest. However, the broadening of reflections in the powder diffraction pattern contains much information; such as crystallite strain, shape and stacking faults, which are often not considered. Figure 69 shows that both the calculated and experimental XRD patterns for bulk spinel $LiMn_2O_4$ are in accord. The indexed peaks from this study correspond to the experimentally measured results. This validates the starting model which is the bulk material, from which all the nanotubes generated emanated from.

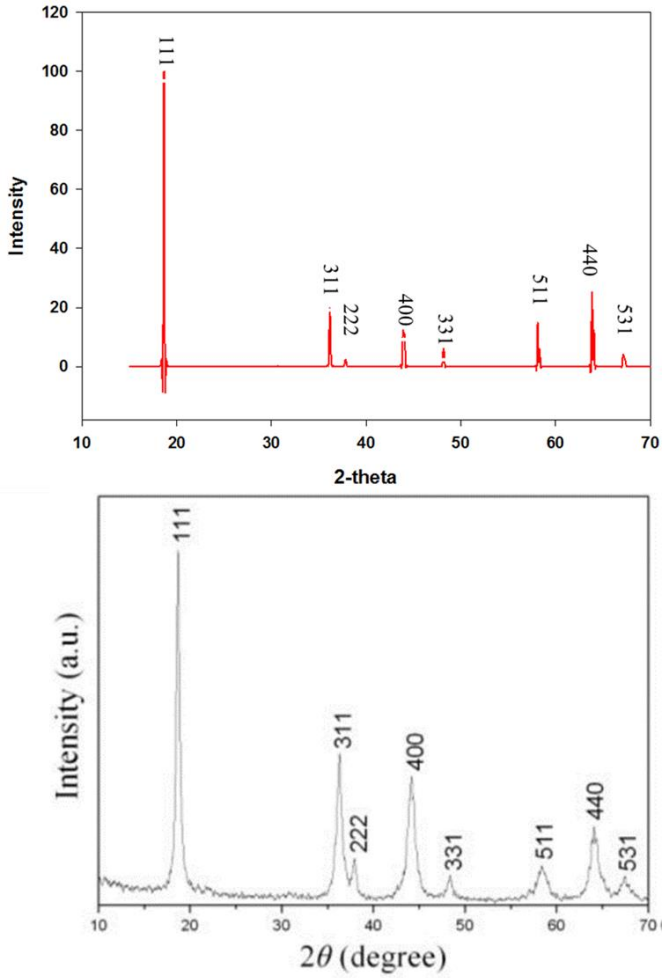

Figure 69: Calculated and experimental [90] XRD patterns for $LiMn_2O_4$.

4.8.1 $LiMn_2O_4$ {100} Nanotube

In this section, different XRD patterns for $LiMn_2O_4$ {100} nanotubes with smaller diameter 5Å-11Å are calculated and discussed. Figure 70 shows the XDR patterns for $LiMn_2O_4$ nanotube with diameter of 5Å and 7Å. The calculated XRD patterns predict that for 5Å nanotube the first highest peak appears at approximately 27 2θ, with an index of {200}, while 7Å nanotube predicts the highest peak at approximately 28 2θ indexed {030}. The diffraction peaks for the nanotubes are found not to be identical and they tend to shift as the diameter is varied. This may be attributed to the differences in bond lengths and strain applied when wrapping the nanotube. Thus, the nanotubes have different orientations for the atoms. Plane {030} and {130} are dominant in 7Å nanotube i.e., they have the highest intensity whereas in the case of 5Å nanotube these particular planes have the lowest intensity.

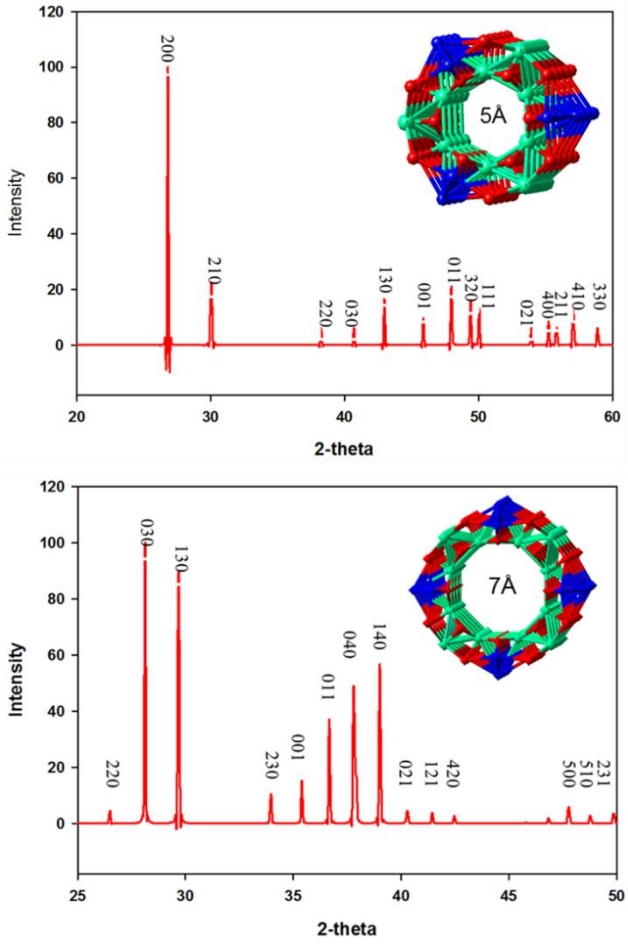

Figure 70: XRD for $LiMn_2O_4$ nanotube generated from {100} surface with diameter of 5Å and 7Å.

Figure 71 shows the XRD patterns for $LiMn_2O_4$ nanotube generated from {100} surface with the diameter of 9Å and 11Å. The calculated XRD patterns predict that for 9Å nanotube the first three peaks indexed {220}, {300} and {130} appear with low intensity while for 11Å nanotube the peaks indexed {200}, {300} and {130} are calculated to have higher intensity. It is predicted that the first three peaks for 9Å and 11Å diameter have the same index but different intensities. The intensity of the peaks is determined by the arrangement of atoms within the nanotube. Thus, the nanotubes generated from the same Miller index produce different morphologies because of the difference in size of the diameter. Hence, the size of the matter has a direct control on the final morphology of the nanotube as observed with MnO_2 nanotubes.

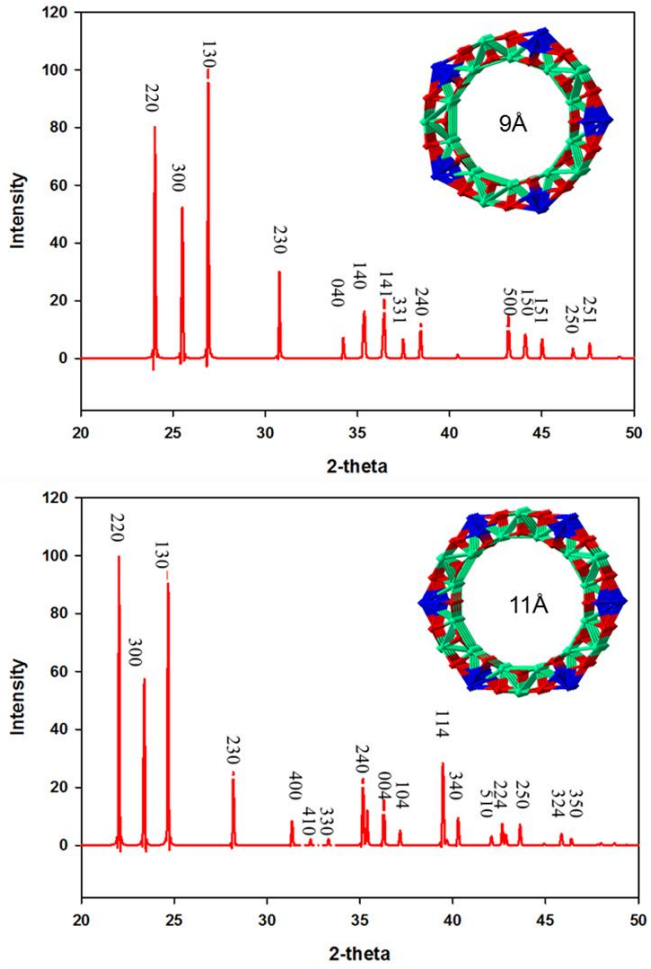

Figure 71: XRD for $LiMn_2O_4$ nanotube generated from {100} surface with diameter of 9Å and 11Å.

4.8.2 $LiMn_2O_4$ {110} Nanotube

The positions of the peaks are determined by the size and shape of the unit cell and the symmetry. In this section, different XRD patterns for $LiMn_2O_4$ {110} nanotubes with diameter of 5Å-11Å are calculated and discussed. Figure 72 shows XRD patterns for $LiMn_2O_4$ {110} nanotubes with diameters of 5Å and 7Å. XRD patterns for 5Å nanotube depict pattern made up of significant number of peaks compared to other nanotubes of different sizes of the diameter. The peak for the {310} plane appears to be the most stable peak with the highest intensity for both 5Å and 7Å nanotubes. The peaks for the other planes are significantly reduced for a 7Å nanotube.

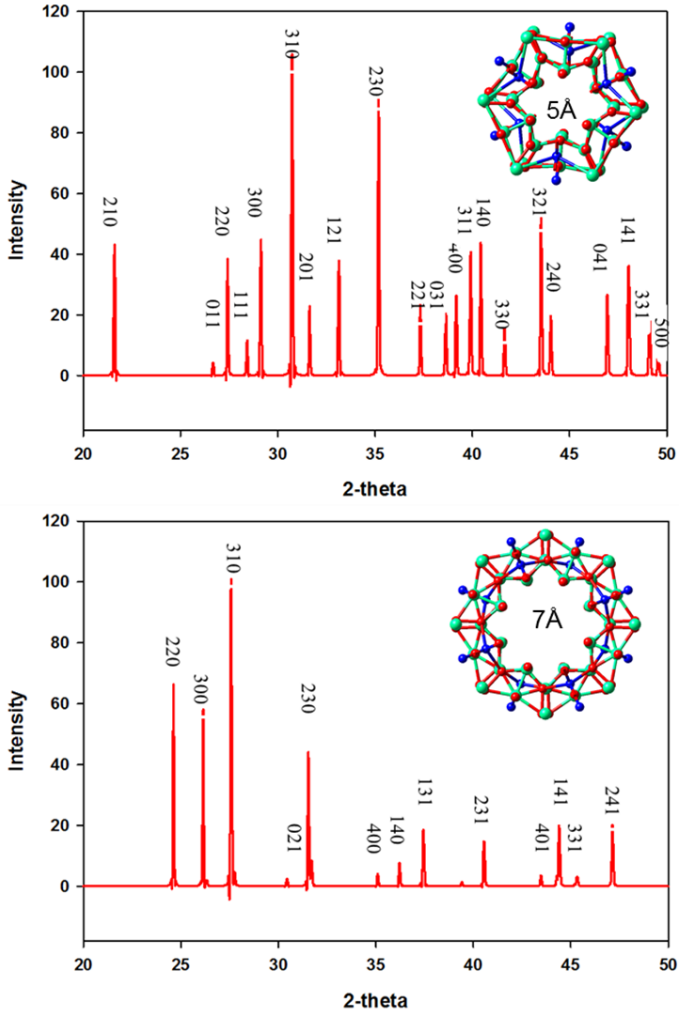

Figure 72: XRD for $LiMn_2O_4$ nanotube generated from {110} surface with diameter of 5Å and 7Å.

Figure 73 shows XRD patterns for $LiMn_2O_4$ {110} nanotube with diameter of 9Å and 11Å. For 9Å nanotube the calculated XRD patterns show the first three highest peaks indexed {220}, {300} and {310} at 23 2θ, 24 2θ and 25 2θ position, respectively. The {310} plane has the highest intensity as compared to {220} for 11Å nanotube. The first three highest peaks {220}, {300} and {130} for 11Å are positioned at approximately 21 2θ, 22 2θ and 23 2θ, respectively. As discussed previously, it is noted that the diameter has an impact on the average bond distance, hence the differences in structural morphologies of the nanotubes.

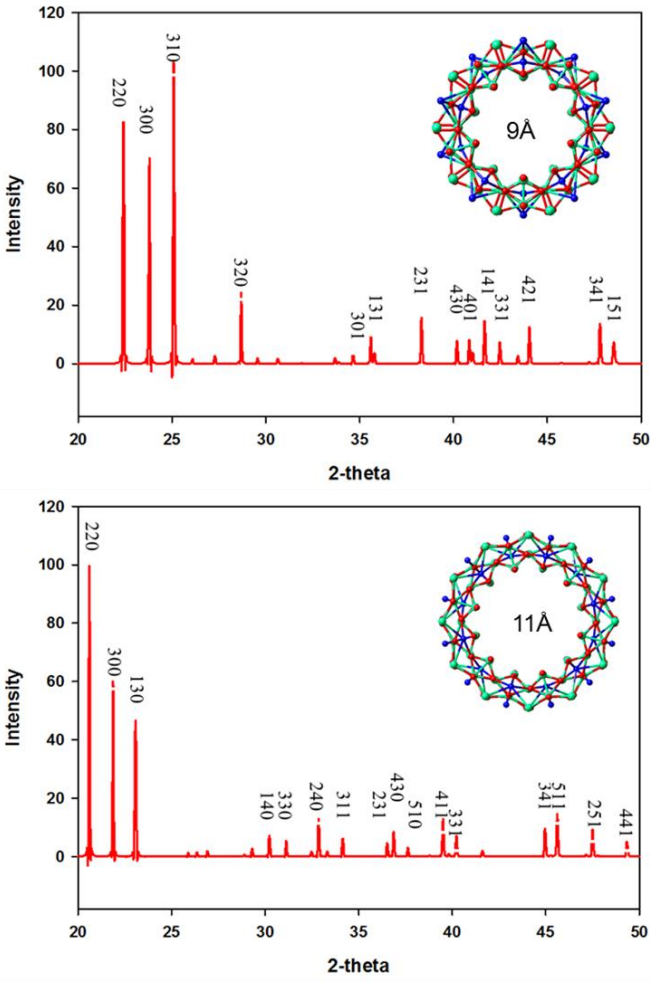

Figure 73: XRD for $LiMn_2O_4$ nanotube generated from {110} surface with diameter of 9Å and 11Å

4.8.3 $LiMn_2O_4$ {111} Nanotube

In this section, different XRD patterns for $LiMn_2O_4$ {111} nanotubes with diameter of 5Å-11Å are calculated and presented. Figure 74 shows the XRD patterns for $LiMn_2O_4$ nanotube with diameter of 5Å and 7Å. The peaks with high intensity show that on that plane the atoms a well arranged therefore it's suggest that the plane is more stable. For 5Å nanotube reveals only one peak indexed {200} as the peak with the highest intensity while for 7Å nanotube the patterns show two peaks for the plane {030} and {130} with high intensity.

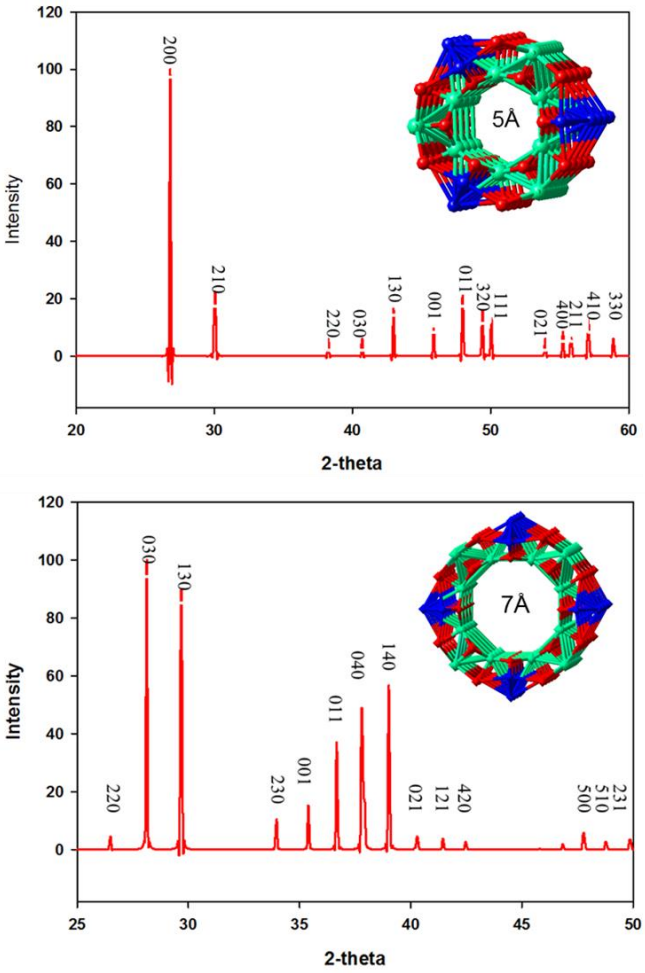

Figure 74: XRD for $LiMn_2O_4$ nanotube generated from {111} surface with diameter of 5Å and 7Å.

Figure 75 shows XRD patterns for $LiMn_2O_4$ {110} nanotube with diameter of 9Å and 11Å. For 9Å nanotube the XRD patterns are indexed with most of the peak being more intense. The first peak indexed {120} is positioned at approximately 24 2θ. For nanotube with 9Å the XRD patterns depict a graph with numerous planes with high intensity as compared to the 11Å nanotube, whereby some of the peaks diminished, particularly at the higher values of 2θ. The first two peaks for both 9Å and 11Å nanotubes have the same Miller indices i.e., {120} and {220} but occurring at different 2θ positions. Thus, the diffraction peaks are found to be shifting as the size of the diameter is changed. This is attributed to the change in positions and orientation of the atoms.

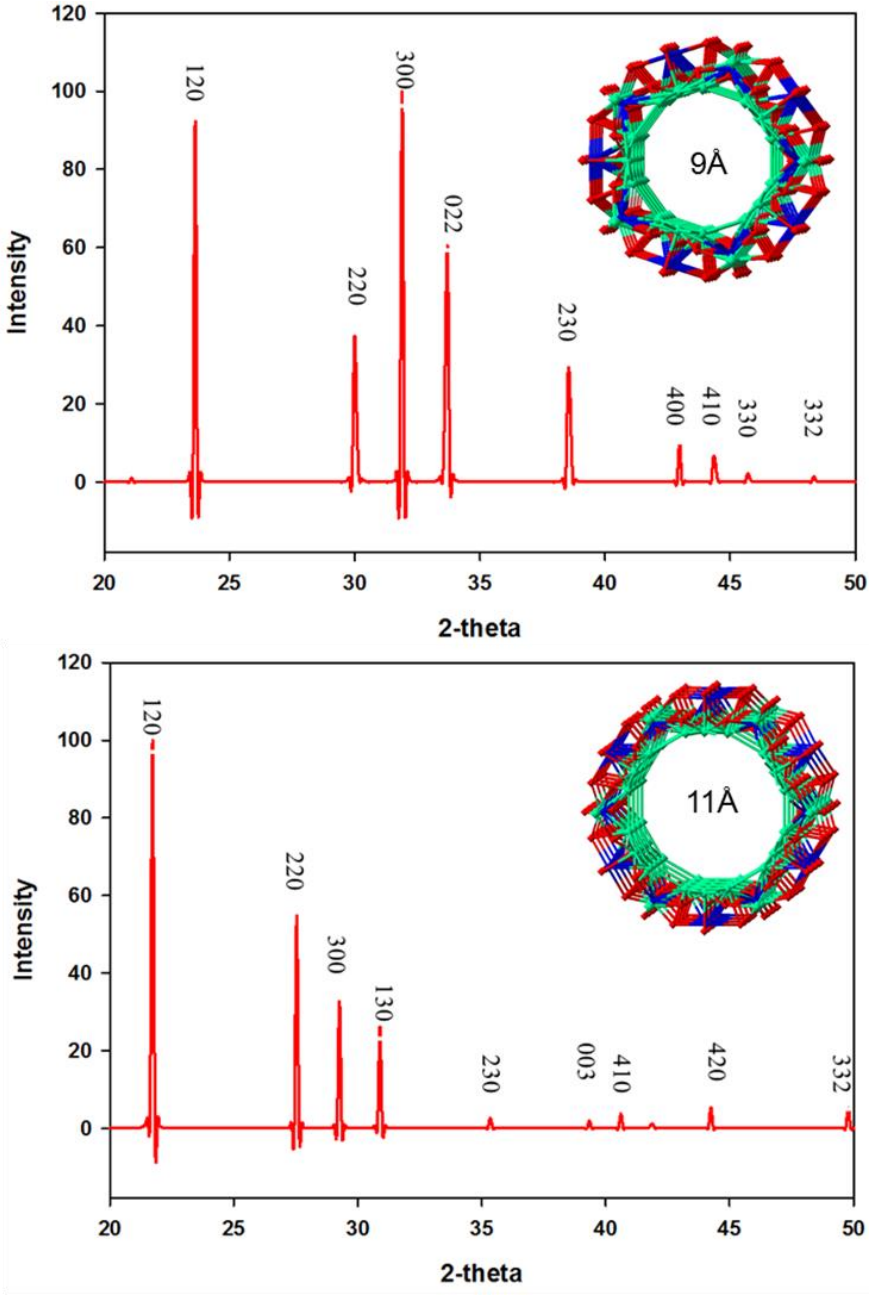

Figure 75: XRD for $LiMn_2O_4$ nanotube generated from {111} surface with diameter of 9Å and 11Å.

Chapter 5

Conclusion

5.1 Conclusion

Computer simulation methods were employed successfully to generate MnO_2 and $LiMn_2O_4$ nanotubes structures. In particular, three different computer simulation software were used to develop and investigate nanotube structures. Thus, Medea software package was used to generate nanotube structures, Materials Studio was used to visualise the models and determine their stability and DL_POLY code was employed to carry out all molecular dynamics simulations. The structures of nanotubes were examined in terms of primary variables, i.e., diameter, morphology and length. These variables play a vital role in describing the structure of the nanotube, including the number of walls that the nanotube has and the shape of the nanotube.

The formation of the nanotube structure directly impact properties such as, electronic, physical and chemical. Also, the diameter determines the radius of the curvature of the nanotube, which has an impact on the surface functionalisation. It was found that when building the nanotubes, as the value of the diameter is increased, the cross-sectional area of the nanotube is decreased. The nanotube were found to be more compact with an increase in nanotube diameter. Nanotube with different diameters resulted in system with different bond lengths between similar atom configuration. Thus, calculated bond lengths depend on the diameter of the nanotubes. Nanotubes cut from the same Miller index but with different diameters gave different bond lengths between Mn-O, Mn-Mn and O-O. Visualisation of the atomic positions revealed that the atoms are arranged in long, hollow cylinder, depending on how the slab has been rolled. Furthermore, it was found that diameter has an impact on the calculated density of the systems, as the diameter of the nanotube is increased the calculated density increased. This implies that the generated nanotube structures, could increase the rate capability of the cathode materials because reducing the particle size of the cathode material from micrometer to nanometer shortens the lithium ion diffusion paths.

Experiments established that morphological control of nanotubes has a significant impact on their performance as cathode materials in lithium-batteries, since many properties are highly shape and size dependent. The surfaces of the nanotubes are difficult to extract by experiment alone as currently there are no efficient methods of controlling morphology of the nanostructures. Computer simulations, on the other hand offer an extremely useful means and potential of exploring morphological properties. Different Miller indices for both MnO_2 and $LiMn_2O_4$ produced different nanotubes structures and the stabilities were determined. MnO_2 nanotube made from (100) surface was found to be the most stable while for $LiMn_2O_4$ (110) surface produced the most stable nanotube. These findings imply that most stable structure for both MnO_2 and spinel $LiMn_2O_4$ nanotubes depends on the surface and the terminations of the surface. Furthermore, it was found that different Miller indices generate different nanotubes with different number of walls. The surfaces (001) produced single wall nanotubes whereas (100), (110) and (111) produced multi wall nanotubes. Nanotubes generated from the same Miller index with different diameters produce nanotubes with similar structures with different number of atoms. The number of atoms increased as the diameter of the nanotube was increased. Also, it was established that different nanotube structures created from the same Miller index exist, depending on the direction that the surface was rolled-up. Thus, nanotubes can be rolled as a_around_b or b_around_a and this yield different nanotubes depending on their wrap direction. The most stable method to wrap nanotubes is a_around_b direction.

Classical molecular dynamics was used to investigate the nanotube structural behaviour at different temperatures. The radial distribution functions were used to describe the nanotube structures, depicting how the atoms are packed around each other in the system. Temperature dependences revealed that as the temperature is increased, the height of the peaks decrease. X-Ray powder diffraction technique was used to analyse the phase identification of generated nanotubes with varying parameters. All the diffraction peaks were successfully indexed using simulation techniques. General observation from XRD patterns was that as the diameter and the Miller indices change, the position and the intensity of the peak changes. The change in peak intensity shows that the diameter has an effect on the stability of nanotubes. The higher the peak intensity the more stable is the nanotube. The predicted XRD

patterns will give insights on both MnO_2 and $LiMn_2O_4$ nanotubes structures, particular to experimentalists.

In summary, the strategy established in this study is capable of controlling the size, diameter and length of the nanotube while experimentally it is extremely difficult to control all these variables. It is worth noting that the size, diameter, symmetry, orientation and Miller index have direct control on the final morphology of the nanotube. The same observation has been found experimentally. The phase and morphology of manganese oxide based cathode battery materials is still not well understood and the properties of the electrochemical devices extremely rely on the crystalline phase and morphology of nanostructures at large. It is recommended that the strategies presented in this study can be applied to many other materials, including metals, metal oxides and semiconductors.

5.2 Recommendations

Generation of MnO_2 and spinel $LiMn_2O_4$ nanotubes offer the prospect of new fundamental science, useful in nano-technological and energy storage applications. The advantages of these applications have been demonstrated, including their small size, lower weight and high performance. The exceptional design flexibility has useful implications including for fluid transportation and capillarity on the nanometer scales. Development of these nanostructures yield new forms, new applications and new materials based on the unique properties. Examining the properties of these structures one needs tubes with well-defined morphology, length, thickness, inner diameter and the number of concentric shell. The study established relevant conditions for controlling size, morphology, thickness, length, etc. of nanotubes for electrode materials.

Further investigation on these nanotubes could involve calculating properties related to battery performance, such as electronic, electrochemical, etc. Most studies on simulation of nanotubes are based on single atom systems, e.g. Carbon nanotube, Silicon nanotubes, etc. This strategy can be applied to other materials (binary and ternary system) particularly, transitional metal oxides for application on batteries.

References

[1] A.S. Arico, P.G. Bruce, B. Scrosati, J.M. Tarascon and W.V. Schalkwijk, “Nanostructured Materials for Advanced Energy Conversion and Storage Devices,” Nature Materials, vol. 4, pp. 366-377, 2005.

[2] J.M. Tarascon and M. Armand, “Issues and Challenges Facing Rechargeable Lithium Batteries,” Nature, vol. 414, pp. 359-367, 2001.

[3] R. Strobel, L. Jorissen, T. Schliermann, V. Trapp, W. Schutz, K. Bohmhammel, G. Wolf and J. Garche, “Hydrogen Adsorption on Carbon Materials,” Journal of Power Sources, vol. 84, pp. 221-224, 1999.

[4] Y.J. Lee, M.G. Kim and J.P. Cho, “Layered $Li_{0.88}[Li_{0.18}Co_{0.33}Mn_{0.49}]O_2$ Nanowires for Fast and High Capacity Li-ion Storage Material,” NanoLetter, vol. 8, pp. 957-961, 2008.

[5] S.C. Lee, S.M. Lee, J.W. Lee, J.B. Lee, S.M. Lee, S.S. Han, H.C. Lee and H.J. Kim, “Spinel $Li_4Ti_5O_{12}$ Nanotubes for Energy Storage Materials,” Journal Physical Chemistry, vol. 113, pp. 18420-18423, 2009.

[6] H. Li, W.L. Wang, F. Pan, X. Xin, Q. Chang and X. Liu., “Synthesis of Single-Crystalline MnO_2 Nanotubes and Structural Characterization by HRTEM,” Material Science and Engineering B, vol. 176, pp. 1054-1057, 2011.

[7] S. Iijima, “Helical Microtubules of Graphitic,” Nature, vol. 354, pp. 56-58, 1991.

[8] S.J. Tans, R.M. Verschueren and C. Dekker, “Room-Temperature Transistor Based on a Single Carbon Nanotube,” Nature, vol. 393, pp. 49-52, 1998.

[9] E.T. Thostenson, Z. Ren and T.W. Chou, “Advances in The Science and Technology of Carbon Nanotubes and their Composites: A Review,” Composites Science and Technology, vol. 61, pp. 1899-1912, 2001.

[10] J. Che, T. Çagin and W.A. Goddard, “Thermal Conductivity of Carbon Nanotubes,” Nanotechnology, vol. 11, pp. 65-69, 2000.

[11] R. Tenne, L. Margulis, M. Genut and G. Hodes, “Polyhedral and Cylindrical Structures of Tungsten Disulphide,” Nature, vol. 360, pp. 444-446, 1992.

[12] M. Remskar, “Inorganic Nanotubes Beyond Cylindrical Matter Comprehensive Nanoscience and Technology,” Nanomaterials, vol. 1, pp. 315-333, 2011.

[13] M. Remskar, Z. Skraba, F. Cléton, R. Sanjinés, and F. Lévy, “MoS_2 as Microtubes,” Applied Physics Letters, vol. 69, pp. 351-353, 1996.

[14] S.M. Li, Y.S. Wang, S.Y. Yang, C.H. Liu, K.H. Chang, H.W. Tien, N.T. Wen, C.C.M. Ma and C.C. Hu, “Electrochemical Deposition of Nanostructured Manganese Oxide on Hierarchically Porous Graphene Carbon Nanotube structure for ultrahigh-performance electrochemical capacitors,” Journal of Power Sources, vol. 225, pp. 347-355, 2013.

[15] A.S. Arico, P.G. Bruce, B. Scrosati, J.M. Tarascon and W.V. Schalkwijk, “Nanostructured Materials for Advanced Energy Conversion and Storage devices,” Nature Materials, vol. 4, pp. 366-377, 2005.

[16] D.T. Mitchell, S.B. Lee, L. Trofin, N. Li, T.K. Nevanen, H. Söderlund and C.R. Martin, “Smart Nanotubes for Bioseparations and Biocatalysis,” Journal of the American Chemical Society, vol. 124, pp. 11864-11865, 2002.

[17] D. Gong, G.A. Grimes, O.K. Varqhese, W. Hu, R.S. Singh. Z. Chen and E.C. Dickey, “Titanium Oxide Nanotube Array Prepared by Anodic Oxidation,” Journal of Materials Research, vol. 16, pp. 3331-3334, 2001.

[18] Q. Zhu, H. Hu, G. Li, C. Zhu, Y. Yu, “TiO_2 Nanotube Arrays Grafted with MnO_2 Nanosheets as High-Performance Anode for Lithium-ion Battery,” Electrochimica Acta, vol. 156, pp. 252-260, 2015.

[19] F.M. Hossain, A.V. Evteev, I.V. Belova , J. Nowotny and G.E. Murch, “Electronic and Optical Properties of Anatase TiO_2 Nanotubes,” Computational Materials Science, vol. 48, pp. 854-858, 2010.

[20] Y. Yu, P. Zhang, L. Guo, Z. Chen, Q. Wu, Y. Ding and W. Zheng,, “The Design of TiO_2 Nanostructures (Nanoparticle, Nanotube and Nanosheet) and Their

Photocatalytic Activity," Journal of Physical Chemistry C, vol. 118, pp. 12727-12733, 2014.

[21] K.M. Shaju, F. Jiao, A. Débarta and P.G. Bruce, "Mesoporous and Nanowire Co_3O_4 as Negative Electrodes For Rechargeable Lithium Batteries," Journal of Physical Chemistry, vol. 9, pp. 1837-1842, 2007.

[22] Y. Ding and Z.L. Wang, "Structure Analysis of Nanowires and Nanobelts by Transmission Electron Microscopy," Journal of Physical Chemistry B, vol. 108, pp. 12280-12291, 2004.

[23] M. Okubo, Y. Mizuno, H. Yamada, J.Kim, E. Hosono, H. Zhou, T. Kuda and I. Honma,, "Fast Li-ion Insertion into Nanosized $LiMn_2O_4$ without Domain boundaries," American Chemical Society, vol. 4, pp. 741-752, 2010.

[24] Z.L. Wang, "Nanobelts, Nanowires and Nanodiskettes of Semiconducting Oxides From Materials to Nanodevices," Advanced Materials, vol. 15, pp. 432-436, 2003.

[25] T. Doi, Y. Iriyama, T. Abe and Z. Ogumi, "Electrochemical Insertion and Extraction of Lithium-ion at Uniform Nanosized $Li_{4/3}Ti_{5/3}O_4$ Particles Prepared by a Spray Pyrolysis Method," Chemistry of Materials, vol. 17, pp. 1580-1582, 2005.

[26] I. Moriguch, R. Hidaka, H. Yamada, T. Murakami, H. Kodu and H. Nakashima, "A Mesoporous Nanocomposite of TiO_2 and Carbon Nanotubes as a High-Rate Li-Intercalation Electrode Material," Advanced Materials, vol. 18, pp. 69-73, 2006.

[27] T. Kudo, Y, Ikeda, T. Watanabe, M. Hibino, M. Miyayama, H. Abe and K. Kajita, "Amorphous V_2O_5/Carbon Composition as Electrochemical Supercapacitor Electrodes," Solid State Ionic, vol. 152-153, pp. 833-841, 2002.

[28] P.L. Taberna, S. Mitra, P. Poizot, P. Simon and J.M. Tarascon, "High Rate Capabilities Fe_3O_4-Based Cu Nano-Architectured Electrodes for Lithium-ion Battery Applications," Nature Materials, vol. 5, pp. 567-573, 2006.

[29] J.H. Choy, D.H. Kim, C.W. Kwon, S.J. Hwang and Y.I. Kim, "Physical and Electrochemical Characterization of Nanocrystalline $LiMn_2O_4$ Prepared by a Modified Citrate Route," Journal of Power Sources, vol. 77, pp. 1-11, 1999.

[30] A.R. Armstrong, G. Armstrong, J. Canales, R. García and P.G. Bruce, “Lithium-Ion Intercalation into TiO_2-B Nanowire,” Advanced Materials, vol. 17, pp. 862-865, 2005.

[31] Y.S. Horn, L. Croguennec, C. Delmas, E.C. Nelson and M.A. O'Keefe, “Atomic Resolution of Lithium Ions in $LiCoO_2$,” Nature Materials, vol. 2, pp. 464-467, 2003.

[32] M.M. Thackeray, W.I.F. David, P.G. Bruce and J.B. Goodenough, “Synthesis of Layered $LiMnO_2$ as an Electrode for Rechargeable Lithium Batteries,” Materials Research Bulletin, vol. 18, pp. 461-472, 1983.

[33] C. Delacourt, P. Poizot, J.M. Tarascon and C. Masquelier, “The Existence of a Temperature-Driven Solid Solution in Li_xFePO_4 for $0<x<1$,” Nature Materials, vol. 4, pp. 254-260, 2005.

[34] H.S. Zhou, D.L. Li, M. Hibino and I. Honma, “A Self-Ordered, Crystalline–Glass, Mesoporous Nanocomposite for Use as a Lithium-Based Storage Device with Both High Power and High Energy Densities,” Angewandte Chemie International Edition, vol. 44, pp. 797-802, 2005.

[35] Z. Fan, J. Chen, B. Zhang, B. Liu, X. Zhong and Y. Kuang, “High Dispersion of MnO_2 on Well-Aligned Carbon Nanotube Arrays and its Application in Supercapacitors,” Diamond and Related Materials, vol. 17, pp. 1943-1948, 2008.

[36] G. Qiu, H. Huang, S. Dharmarathna, E. Benbow, L. Stafford and S.L. Suib, “Hydrothermal Synthesis of Manganese Oxide Nanomaterials and Their Catalytic and Electrochemical Properties,” Chemistry of Materials, vol. 23, pp. 3890-3901, 2011.

[37] F. Cheng, J. Zhao, W. Song, C. Li, H. Ma, J. Chen and P. Shen, “Facile Controlled Synthesis of MnO_2 Nanostructures of Novel Shape and Their Application in Batteries,” Inorganic Chemistry, vol. 45, pp. 2038-2044, 2006.

[38] J. Wu, H. Huang, L. Yu and J. Hu, “Controllable Hydrothermal Synthesis of MnO_2 Nanostructures,” Advanced in Materials Physics and Chemistry, vol. 3, pp. 201-205, 2013.

[39] R.S. Kaluabarme, M.S. Cho, K.S. Yun, T.S. Kim and C.J. Park, “Catalytic Characteristics of MnO_2 Nanostructres for the O_2 Reduction Process,” Nanotechnology, vol. 22, pp. 1-6, 2011.

[40] H. Xia, J. Feng, H. Wang, M.O. Lai and L. Lu, “MnO_2 Nanotubes and Nanowire Array by Electrochemical Deposition for Supercapacitors,” Journal of Power Sources, vol. 195, pp. 4410-4413, 2010.

[41] J. Luo, H.T. Zhu, H.M. Fan, J.K. Liang, H.L. Shi, G.H. Rao, J.B. Li, Z.M. Du and Z.X. Shen, “Synthesis of Single-Crystal Tetragonal δ-MnO_2 Nanotubes,” Journal of Physical Chemistry C letters, vol. 112, pp. 12594-12598, 2008.

[42] M.S. Wu, J.T. Lee, Y.Y. Wang and C.C. Wan, “Field Emission from Manganese Oxide Nanotubes Synthesized by Cyclic Voltammetric Electrodeposition,” Journal of Physical Chemistry B Letters, vol. 108, pp. 16331-16333, 2004.

[43] D. Zheng, S. Sun, W. Fan, H. Yu, C. Fan, G. Cao, Z. Yin and X. Song, “One-Step Preparation of Single-Crystalline α-MnO_2 Nanotubes,” Journal of Physical Chemistry B, vol. 109, pp. 16439-16443, 2005.

[44] T.X.T Sayle, R.R. Maphanga, P.E. Ngoepe and D.C Sayle, “Predicting the Electrochemical Properties of MnO_2 Nanomaterials Used in Rechargeable Li Batteries: Simulating Nanostructure at the Atomistic Level,” Journal of Americal Chemistry Society, vol. 131, pp. 6161-6173, 2009.

[45] T.X.T. Sayle, R.A. Catlow, R.R. Maphanga, P.E. Ngoepe and D.C. Sayle, “Generating MnO_2 Nanoparticles Using Simulated Amorphization and Recrystallization,” Journal of American Society, vol. 127, pp. 12828-12837, 2005.

[46] W. Chen, R.B. Rakhi, Q. Wang, M.N. Hedhili and H.N. Alshareef, “Morphological and Electrochemical Cycling Effects in MnO_2 Nanostructures by 3D Electron Tomograph,” Advanced Functional Materials, vol. 24, pp. 3130-3143, 2014.

[47] V. Subramanian, H. Zhu, R. Vajtai, P.M. Ajayan and B. Wei, “Hydrothermal Synthesis and Pseudocapacitance Properties of MnO_2,” Journal of Physical Chemistry B, vol. 109, pp. 20207-20214, 2005.

[48] X. Zhou, M. Chen, M. Xiang, H. Bai and J. Gou, “Solid-State Combustion Synthesis of Spinel $LiMn_2O_4$ Using Glucose as a Fuel,” Ceramics International, vol. 39, pp. 4783-4789, 2013.

[49] A. Blyr, C. Sigala, G. Amatucci, D. Guymard, Y, Chabre and J. Tarascon, “Self-Discharge of $LiMn_2O_4$/C Li-Ion Cells in Their Discharged State Understanding by Means of Three-Electrode Measurements,” Journal of Electrochemical Society, pp. 194-209, 1998.

[50] Y. Gao and J.R. Dahn, “Synthesis and Characterization of $Li_{1+x}Mn_{2-x}O_4$ for Li-Ion Battery Applications,” Journal of the Electrochemical Society, vol. 143, pp. 100-114, 1996.

[51] J.Y. Luo, H.M. Xiong and Y.Y. Xia, “$LiMn_2O_4$ Nanorods, Nanothorn Microspheres and Hollow Nanospheres as Enhanced Cathode Materials of Lithium-ion Battery,” Journal of Physical Chemistry C, vol. 112, pp. 12051-12057, 2008.

[52] Y. Sun, C. Xu, B. Li, J Xu, Y. He, H. Du and F. Kang, “Synthesis of Single-Crystalline $LiMn_2O_4$ with Different Dimensional Nanostructures for Li-ion Battries.,” International Journal of Electrochemical Science, vol. 9, pp. 6387-6401, 2014.

[53] Z. Kai, W. Yang, Z. Shuang, Y. Yan, P. Hao, L. Guiwei and J. Jianli, “Synthesis of Single Crystalline Spinel $LiMn_2O_4$ Nanorods for Lithium-ion Battrey,” International Journal of Electrochemical Science, vol. 9, pp. 5280-5288, 2014.

[54] D.K. Kim, P. Muralidharan, H.W. Lee, R. Ruffo, Y. Yang, C.K. Chan, H. Peng, R.A. Huggins and Y. Cui, “Spinel $LiMn_2O_4$ Nanorods as Lithium-ion Battery Cathodes,” NanoLetters, vol. 8, pp. 3948-3952, 2008.

[55] E. Hosono, T. Kudo, I. Honma, H. Matsuda and H. Zhou, “Synthesis of Single Crystalline Spinel $LiMn_2O_4$ Nanowires for a Lithium-ion Battery with High Power Density,” NanoLetters, vol. 9, pp. 1045-1051, 2009.

[56] S. Lee, Y. Oshima, E. Hoson, H. Zhou, K. Kim, H.M. Chang, R. Kanno and K. Takayanagi, “Phase Trasitions in a $LiMn_2O_4$ Nanowire Battery observed by

Operando Electron Microscopy," American Chemical Society Nano, vol. 9, pp. 626-632, 2015.

[57] H. Zhao, D.F. Chen, M. Yan, J. Peng, M.M. Wua, X.L. Xiao and Z.B. Hu, "A Novel Two-Step Preparation of Spinel $LiMn_2O_4$ Nanowires and its Electrochemical Performance Charaterization," Journal of Materials Research, vol. 27, pp. 1750-1754, 2012.

[58] K.M. Shaju and P.G. Bruce, "A Stoichiometric Nano-$LiMn_2O_4$ Spinel Electrode Exhibiting High Power and Stable cycling," Chemistry of Materials, vol. 20, pp. 5557-5562, 2008.

[59] C.H. Jiang, S.X. Dou, H.K. Liu, M. Ichihara and H.S. Zhou, "Synthesis of Spinel $LiMn_2O_4$ Nanoparticle Through One Step Hydrothermal Reaction," Jounal of Power Sources, vol. 9, pp. 410-415, 2007.

[60] Y.L. Ding, J. Xie, G.S. Cao, T.J. Zhu, H.M. Yu and X.B. Zhao, "Single-Crystalline $LiMn_2O_4$ Nanotubes Synthesized via Template-Engaged Reaction as Cathodes for High-Power Lithium-ion Batteries," Advanced Functional Materials, vol. 21, pp. 348-355, 2011.

[61] W. Tang, Y. Hou, F. Wang, L. Liu, Y. Wu and K. Zhu, "$LiMn_2O_4$ Nanotube as Cathode Material of Second-Level Charge Capability for Aqueous Rechargeable Batteries," NanoLetter, vol. 13, pp. 2036-2040, 2013.

[62] W. Bragg, "The Structure of the Spinel Group of Crystals," Philosophical Magazine, vol. 199, pp. 10-15, 1915.

[63] S. Nishikawa, "Structure of Some Crystal of The Spinel Group," Process of Mathematical Physics Society, vol. 199, pp. 8-12, 1915.

[64] P. Hohenberg and W. Kohn, "Inhomogeneous Electron Gas," Physical Review B, vol. 136, pp. 867-871, 1964.

[65] W. Kohn and L.J. Sham, "Self-Consistent Equations Including Exchange and Correlation Effects," Physical Review A, vol. 140, pp. A1133-A1138, 1965.

[66] J.P. Perdew and Y. Wang, “Accurate and simple density functional for the electronic exchange energy: General Gradient Approximation,” Journal of Physical Review B, vol. 33, pp. 8800-8802, 1986.

[67] M.C. Payne, M.P. Teter and T.A. Allan, “Iterative Minimization Techniques for ab-Initio Total-Energy Calculations: Molecular Dynamics and Conjugate Gradients,” Reviews of Modern Physics, vol. 64, pp. 1050-1051, 1992.

[68] W. Koch and M.C. Holthausen, A chemist’s guide to Density Functional Theory, Weinheim: WILEY-VCH, 2001, pp. 75-77.

[69] K. Burke, P. Perdew and M. Ernzerhof,, “Why the Generalized Gradient Approximation Works and How to go Beyond it,” International Journal Quantum of Chemistry, vol. 293, pp. 61-64, 1997.

[70] J.P. Perdew, K. Burke and M. Ernzerhof, “Generalized Gradient Approximation Made Simple,” Physical Review Letters, vol. 77, pp. 3865-3868, 1996.

[71] J.P. Perdew, J.A. Chevary, S.H. Vosko, K.A. Jackson, M.R. Pederson, D.J. Singh and C. Fiolhais, “Atoms, Molecules, Solids and Surface: Application of the Generalized Gradient Approximation for Exchange and Correction,” Physical Review B, vol. 46, pp. 6671-6687, 1992.

[72] A.E. Mattsson, P.A. Schultz, M.P. Desjarlais, T.R. Mattsson and K. Leung, “Desiging Meaningful Density Functional Theory Calculations in Materials Science–a Primer,” Modelling and Simulation of Material and Engineering, pp. 1-6, 2005.

[73] M.C. Payne, M.P. Teter, D.C. Allan, T.A. Arias and J.D. Joannopoulos, “Iterative Minimization Techniques for ab initio Total-Energy Calculations: Molecular Dynamics and Conjugate Gradients,” Reviews of Modern Physics, vol. 64, pp. 1050-1051, 1992.

[74] H.J. Monkhorst and J.D. Pack, “Special Points for Brillouin-Zone Integrations,” Physical Review B, vol. 13, pp. 5188-5192, 1976.

[75] A. License, “CASTEP Users Guide,” in Accelrys License, San Diego, 2001.

[76] G. Watson, E.T. Kelsey, N.H. De Leeuw, D.J. Harris and S.C. Parker, “Atomistic Simulation of Dislocations, Surface and Interface in MgO,” Journal of the Chemical Society Faraday Transactions, vol. 101, pp. 275-295, 1996.

[77] J.D. Gale and A.L. Rohl , “The General Utility Lattice Program (GULP),” Molecular Simulation, vol. 5, pp. 291-341, 2003.

[78] W. Smith and T.R. Forester, J. MOL. Graphics, “DL_POLY 2.0: A General-Purpose Parallel Molecular Dynamics Simulations Package,” vol. 14, pp. 136-141, 1996.

[79] T. Teranishi and M. Miyake, “Size Control of Palladium Nanoparticles and Their Crystal Structures,” Chemistry of Materials, vol. 10, pp. 594-600, 1988.

[80] G. Somorjai, Introduction to Surface Chemistry and Catalysis, New York: Wiley, 1994.

[81] M. Pakkhesal and R. Ghayour, Electronic Band Structure of Carbon Nanotubes in Equilibrium and None-Equilibrium Regimes, Iran: InTech Europe, 2011.

[82] D.V. Bavykin, A.A. Lapkin, P.K. Plucinski, J.M. Friedrich and F.C. Walsh , “Reversible Storage of Molecular Hydrogen by Sorption into Multilayered TiO_2 Nanotubes,” Journal of Physical Chemistry B, vol. 109, pp. 19422-19427, 2005.

[83] R.Z. Ma, Y. Bando and T. Sasaki, “Nanotubes of Lepidocrocite Titanates,” Chemical Physics Letters, vol. 380, pp. 577-582, 2003.

[84] Q. Chen, W.Z. Zhou, G.H. Du and L.M. Peng, “Trititanate Nanotubes Made via a Single Alkali Treatment,” Advanced Materials, vol. 14, pp. 1208-1211, 2002.

[85] H.H. Ou and S.L. Lo, “Review of Titania Nanotubes Synthesized via the Hydrothermal Treatment: Fabrication, Modification and Application,” Separation and Purification Technology, vol. 58, pp. 179-191, 2007.

[86] M. Matsui and M. Akaogib, “Molecular Dynamics Simulation of the Structural and Physical Properties of the Four Polymorphs of TiO_2,” Molecular Simulation, vol. 6, pp. 239-244, 1991.

[87] R.R. Maphanga, S.C. Parker and P.E. Ngoepe, “Atomistic Simulation of the Surface Structure of Electrolytic Manganese Dioxide,” Surface Science, vol. 603, pp. 3184-3190, 2009.

[88] J.N. Hart, S.C. Parker and A.A. Lapkin, “Energy Minimisation of Single-Walled Titanium Oxide Nanotubes,” American Chemical Society, vol. 3, pp. 3401-3412, 2009.

[89] B. Ammundsen, G.R. Burns, M.S. Islam, H. Kanoh and J. Roziere, “Lattice Dynamics and Vabrational Spectra of Lithium Manganese Oxides: Computer Simulation and Spectroscopic Study,” Journal of Physical Chemistry B, vol. 103, pp. 5175-5180, 1999.

[90] S. Chen, C. Mi, L. Su and X. Zhang., “Improved Performance of Mechanical-activated $LiMn_2O_4$\MWNTs Cathode for Aqueous Rechageable Lithium Batteries,” Journal of Applied Electrochemical, vol. 39, pp. 1943-1948, 2009.

Appendix

Papers Presented at Conferences

1. D.M. Tshwane, P.E. Ngoepe and R.R. Maphanga, Computer Simulation Study of MnO_2 Nanotubes, 58th Annual Conference of the SA Institute of Physics, University of Zululand, July 2013

2. D.M. Tshwane, P.E. Ngoepe and R.R. Maphanga, Computer Simulation Study of Spinel $LiMn_2O_4$ Nanotubes as a Cathode Material for Lithium-Ion Batteries, 59th Annual Conference of the SA Institute of Physics, University of Johannesburg, July 2014

3. D.M. Tshwane, P.E. Ngoepe and R.R. Maphanga, Computer Simulation Study of Spinel $LiMn_2O_4$ nanotubes. 7th International Symposium on Macro-and Supramolecular Architectures and Materials, Johannesburg, South Africa, November 2014

4. D.M. Tshwane, P.E. Ngoepe and R.R. Maphanga, Generation of spinel $LiMn_2O_4$ nanotubes Using Computer Simulation Strategy, CHPC National Meeting, Kruger National Park, Skukuza, Mpumalanga, December 2014

5. D.M. Tshwane, P.E. Ngoepe and R.R. Maphanga, Computer Simulation as a Strategy for Generating MnO_2 Nanotubes, South African Institute of Physics Annual Conference, Boardwalk Convention Centre, Port Elizabeth, July 2015

6. D.M Tshwane, P.E. Ngoepe and R.R. Maphanga, Generation of MnO_2 Nanotubes using Computer Simulation Method, CHPC National Meeting, CSIR International Convention Centre, Pretoria, December 2015. Best Poster Presentation Award.